Collective Dynamics of Cold Atoms in Optical Cavities

By

Michał Hemmerling

Dissertation

Submitted in Partial Fulfillment of the Requirements
for the Degree of Doctor of Philosophy
in Physics at
University of Strathclyde, 2010

Glasgow, Scotland

This thesis is the result of the author's original research. It has been composed by the author and has not been previously submitted for examination which has led to the award of a degree.

Signed: Date:

"...Rozum i wiedzę miej w pogardzie,
To, czym się szczyci człek najbardziej.
Gdy mamidłami cię oszuka
Kuglarsko–cudotwórcza sztuka,
Wtedyś się dostał w moją moc—
Takiego ducha dał ci los,
Że gdy przed siebie przesz na wprost,
Co tylko spotykasz jest przeszkodą;
Więc z rzeczy mijasz się urodą.
W przygód cię wciągnę korowody,
W arcybanalne epizody.
Będziesz się miotał, wił, trzepotał.
Nienasyconych powab żądz
Wciąż będzie oczom twym migotał.
O napój będziesz błagał, drżąc.
I cóż, żeś mi zaprzedał duszę?
W ręce i tak cię dostać muszę."

("Faust", Johann Wolfgang Goethe)

"...Reason and Knowledge only thou despise,
The highest strength in man that lies!
Let but the Lying Spirit bind thee
With magic works and shows that blind thee,
And I shall have thee fast and sure!—
Fate such a bold, untrammelled spirit gave him,
As forwards, onwards, ever must endure;
Whose over-hasty impulse drave him
Past earthly joys he might secure.
Dragged through the wildest life, will I enslave him,
Through flat and stale indifference;
With struggling, chilling, checking, so deprave him
That, to his hot, insatiate sense,
The dream of drink shall mock, but never lave him:
Refreshment shall his lips in vain implore—
Had he not made himself the Devil's, naught could save him,
Still were he lost forevermore!

("Faust", Johann Wolfgang Goethe)

Acknowledgements

To my dad.

I want to thank my supervisor Doctor Gordon Robb for his help and patience, and my family and friends for their support.

ABSTRACT

Cooling and manipulation of atoms and molecules has been recently of great interest. Cold atoms provide a useful tool to understand many physical phenomena, including quantum information processing, Bose-Einstein Condensation, atom interferometry, ultra-high precision spectroscopy, atomic clocks and many others. Most methods of cooling and slowing, however, apply to a relatively small range of temperatures, and cooling rather hot samples of atoms requires using more than one method only. Moreover, the majority of existing schemes including the most important – Doppler cooling and magneto-optical trapping are limited to the alkali and alkaline earth metals. For that reason it is very attractive to develop new effective cooling schemes.

In this thesis a novel cavity cooling method based on combined cavity-atom dynamics has been investigated. In contrast to Doppler cooling, cavity cooling does not rely on the internal structure of the particle. Consequently, cavity cooling should be applicable to a wider range of particle species e.g. molecules, which do not have a closed atomic transition. Furthermore, in some regimes of cavity cooling the temperature is limited not by the spontaneous emission rate but by the cavity decay rate so the temperature can be at or below the Doppler limit. There have been several recent cavity cooling experiments. Some of these involved a single atom while others have used many atoms interacting with the cavity field inside different cavity geometries.

This thesis presents several analytical and numerical results from cavity cooling simulations. These involve cooling of atoms in a Fabry-Perot cavity using two different configurations – one, in which the optical cavity is assumed to be pumped directly via one of the cavity mirrors or alternatively when the atoms are illuminated by laser beams directed perpendicularly to the cavity axis.

Both configurations are modelled using particle based simulations and a new, distribution-

function (Vlasov) model of cavity cooling. This Vlasov model should be more practical for modelling cavity cooling experiments involving large numbers of atoms and photons.

In addition to the classical models of cavity cooling developed previously, a semi-classical model is also presented. An analytical and numerical comparison of the classical and the semi-classical cavity cooling models is presented. The semi-classical model within a low excitation regime agrees very well with its classical counterpart, however for cases which involve the internal degrees of freedom of the atoms the semi-classical model reveals new interesting features.

Finally, in addition to Fabry-Perot cavities a ring cavity with a phase modulated pump field is also studied. This scheme has the distinguishing feature that the optical potential is able to move inside the cavity which in certain regimes provides an opportunity to control the dynamics of the atomic ensemble and can eventually lead to effective slowing of an atomic beam.

Contents

List of Figures

Chapter 1

Introduction

1.1 Light Forces

The idea that light may affect the motion of matter originates from the 17th century with Kepler who noticed that a comet tail always points away from the Sun regardless of what direction it was moving in relation to the Sun. Kepler suggested that those tails were driven by the pressure of the sunlight, which in fact was not completely correct, but it identified a significant astrophysical effect and stimulated further work to explain its origin. The first proper theoretical basis of light pressure was given in 1873 by Maxwell who formulated the electromagnetic theory of light [1] and showed that an electromagnetic field exerts a pressure proportional to the energy of the field per unit volume. Another important step towards understanding light forces was made by Einstein, in 1917, who showed that a quantum of light, i.e a *photon*, carries not only energy $h\nu$ but also momentum $hv/c = h/\lambda$. Soon after his theory the particle-like nature of radiation was reinforced by subsequent experiments that led to further discovery of light pressure phenomena. The first took place in the early 1920's with the experimental demonstration of the Compton effect where electrons were scattered by high frequency photons and a decade after, in 1933, by Frisch in Hamburg who illuminated a thermal beam of sodium atoms with resonant light [2]. Although instructive, all experiments until then were limited by the inten-

sity of the source and could not fully reveal the potential of the pressure force. The discovery of the laser in 1960 finally resolved that limitation and resulted in many subsequent discoveries: in 1962 Askar'yan showed that an intensity gradient could exert a substantial force on atoms due to an induced dipole moment [3], in 1968 Letokhov suggested that this so called dipole force can be used to trap atoms at the nodes (or antinodes) of a standing wave [4], and shortly afterwards, in the 1970's Ashkin at Bell Laboratories trapped a small glass sphere between opposing focussed laser beams [5]. He also first divided light forces into two classes: a spontaneous force arising from the absorption and spontaneous emission of photons and a dipole force, resulting from absorption followed by stimulated emission of photons. Finally in 1975 Hänsch and Schawlow [6] proposed that laser light could potentially be used to cool atoms and ions.

1.2 Force on Two-Level Atoms

The force F acting on an atom can be defined as an expectation value of the quantum mechanical operator $\mathcal{F}$. This relation is a specific example of the Ehrenfest theorem, which links the quantum mechanical expectation value of an observable and the corresponding classical equation of motion. It simply states that the expectation value of the quantum mechanical operator must correspond to the behaviour of its classical counterpart [7]

$$F = \langle \mathcal{F} \rangle = \frac{d}{dt} \langle p \rangle \tag{1.1}$$

The above relation is a general case of the time evolution of the expectation value of a time-independent quantum mechanical operator, which is given by [8, 9]

$$\begin{aligned} \frac{d}{dt}\langle A \rangle &= \frac{d}{dt} \int (\Psi^* A \Psi)\, dr \\ &= \int \left(\frac{\partial \Psi^*}{\partial t} A \Psi + \Psi^* \frac{\partial A}{\partial t} \Psi + \Psi^* A \frac{\partial \Psi}{\partial t} \right) dr \\ &= \left\langle \frac{\partial A}{\partial t} \right\rangle + \frac{1}{i\hbar} \int \Psi^* \left(A\mathcal{H} - \mathcal{H}A \right) \Psi dr \end{aligned} \tag{1.2}$$

The commutator of the two operators is defined as

$$[A, B] = AB - BA \tag{1.3}$$

and since they commute if their commutator vanishes (1.2) can be written as

$$\frac{d}{dt}\langle A\rangle = \left\langle \frac{\partial A}{\partial t} \right\rangle + \frac{1}{i\hbar}\langle [A, \mathcal{H}]\rangle \tag{1.4}$$

If the operator A does not depend explicitly on time we can write

$$\frac{d}{dt}\langle A\rangle = \frac{i}{\hbar}\langle [\mathcal{H}, A]\rangle \tag{1.5}$$

and hence the commutator of $\mathcal{H}$ and p is given by

$$[\mathcal{H}, p] = i\hbar\frac{\partial \mathcal{H}}{\partial z} \tag{1.6}$$

where the operator p has been replaced with $-i\hbar(\partial/\partial z)$. Consequently from (1.1), (1.5) and (1.6) the force acting on an atom is

$$F = -\left\langle \frac{\partial \mathcal{H}}{\partial z} \right\rangle \tag{1.7}$$

Equation (1.7) forms a quantum mechanical analogue of the classical expression that the force is a negative gradient of a potential.

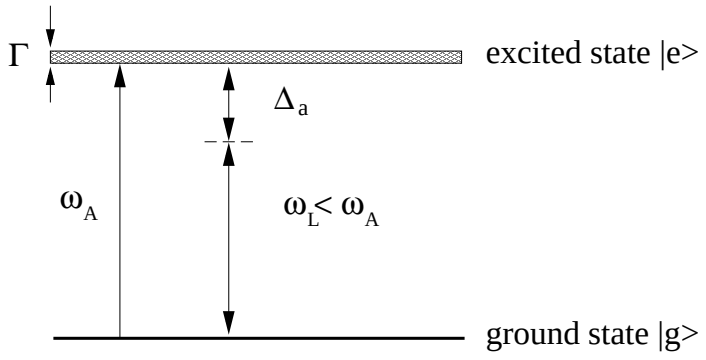

Figure 1.1: Two-level system with the ground state $|g\rangle$ and excited state $|e\rangle$ which has a linewidth Γ. The laser frequency ω_L is red detuned ($\Delta_a < 0$) from the transition frequency ω_a

The Hamiltonian responsible for the interaction with the radiation field is given by

$$\mathcal{H}' = -e\vec{\mathcal{E}}(\vec{r},t)\cdot\vec{r} \tag{1.8}$$

where

$$\vec{\mathcal{E}}(\vec{r},t) = E_0\ \hat{\epsilon}\ cos(kz - \omega_L t) \tag{1.9}$$

which can be used in equation (1.7) in order to find the force on atoms by light fields

$$\langle\mathcal{F}\rangle = F = e\left\langle\frac{\partial}{\partial z}\left(\vec{\mathcal{E}}(\vec{r},t)\cdot\vec{r}\right)\right\rangle \tag{1.10}$$

At this point it is possible to use the electric dipole approximation, i.e assume that

since the electric field changes on a length scale determined by the wavelength of the field then for λ much smaller than the size of the atom the spatial variation of the electric field can be neglected over the size of the atom. In (1.10), this approximation allows the interchange of the gradient with the expectation value

$$F = e\frac{\partial}{\partial z}\left\langle\left(\vec{\mathcal{E}}(\vec{r},t)\cdot\vec{r}\right)\right\rangle. \tag{1.11}$$

The expectation value of (1.11) can be found using the general definition of the expectation value of an operator

$$\langle A\rangle = \langle\Psi|A|\Psi\rangle \tag{1.12}$$

where Ψ is the wavefunction expanded in a basis set of $\{\phi_n\}$

$$\Psi = \sum_{i=1}^{n} c_i\phi_i \tag{1.13}$$

so

$$\langle A\rangle = \left\langle\sum_{ij} c_i\phi_i|A|c_j\phi_j\right\rangle = \sum_{ij} c_i^* c_j\langle\phi_i|A|\phi_j\rangle = \sum_{i,j}\rho_{ji}a_{ij} \tag{1.14}$$

where the elements of the density matrix are

$$\rho_{ij} = \langle \phi_i | \rho | \phi_j \rangle = \langle \phi_i | \Psi \rangle \langle \Psi | \phi_j \rangle = c_i c_j^* \tag{1.15}$$

Hence using (1.14) and (1.15) it is possible to obtain

$$\begin{aligned} F &= \frac{\partial}{\partial z} \left\langle c_1\phi_1 + c_2\phi_2 | - e\vec{\mathcal{E}}(\vec{r},t)\cdot\vec{r} | c_1\phi_1 + c_2\phi_2 \right\rangle \\ &= -e\frac{\partial}{\partial z}\left(c_1 c_2^* \left\langle \phi_1 | \vec{\mathcal{E}}(\vec{r},t)\cdot\vec{r} | \phi_2 \right\rangle + c_1^* c_2 \left\langle \phi_2 | \vec{\mathcal{E}}(\vec{r},t)\cdot\vec{r} | \phi_1 \right\rangle \right) \end{aligned} \tag{1.16}$$

Assigning the basis $\phi_{1,2}$ to the ground and excited state of a two-level atom and then eq. (1.16) can be rewritten as

$$F = -e\frac{\partial}{\partial z}\left(\rho_{eg}^* E_0 \langle e|r|g\rangle + \rho_{eg} E_0 \langle g|r|e\rangle \right) \tag{1.17}$$

Obtaining eq. (1.17) requires implementation of the RWA (i.e Rotating Wave Approximation) that neglects the terms oscillating with the laser frequency.

Equation (1.17) can be then written as

$$F = \hbar\left(\frac{\partial\Omega}{\partial z}\rho_{eg}^* + \frac{\partial\Omega^*}{\partial z}\rho_{eg} \right) \tag{1.18}$$

where Ω is the Rabi frequency defined as

$$\Omega \equiv \frac{-eE_0}{\hbar}\langle e|r|g\rangle \tag{1.19}$$

It is useful to to split $\partial\Omega/\partial z$ in (1.18) into two parts, real and imaginary so that

$$\frac{\partial\Omega}{\partial z} = (q_r + iq_i)\,\Omega \tag{1.20}$$

where $q_r + iq_i$ is the logarithmic derivative of Ω (i.e. if $\Omega = ue^{i\psi}$ with u and ψ real, then $q_r = d/dz\ (lnu)$ and $q_i = d/dz\ (\psi)$).

Consequently the expression for the force expands to

$$\begin{aligned} F =& \hbar\left[(q_r + iq_i)\,\Omega\rho_{eg}^* + (q_r - iq_i)\,\Omega^*\rho_{eg}\right] \\ F =& \hbar q_r\left(\Omega\rho_{eg}^* + \Omega^*\rho_{eg}\right) + i\hbar q_i\left(\Omega\rho_{eg}^* - \Omega^*\rho_{eg}\right) \end{aligned} \tag{1.21}$$

Equation (1.21) describes the total force that can be found for any particular situation as long as ρ_{eg} can be solved (ρ_{eg} is the optical coherence between ground and excited state and can be found from the optical Bloch equations as a stationary state).

Substituting the steady state of the optical coherence between the ground and the excited state ρ_{eg} [10]

$$\rho_{eg} = \frac{i\Omega}{2\left(\Gamma/2 - i\Delta_a\right)\left(1+s\right)} \tag{1.22}$$

into (1.21) reduces it to

$$F = \frac{\hbar s}{1+s}\left(-\Delta_a q_r + \frac{1}{2}\Gamma q_i\right) \tag{1.23}$$

where s is the saturation parameter defined as

$$s \equiv \frac{|\Omega|^2}{2|\Gamma/2 - i\Delta_a|^2} = \frac{|\Omega|^2/2}{\Delta_a^2 + \Gamma^2/4} \equiv \frac{s_0}{1+(2\Delta_a/\Gamma)^2} \tag{1.24}$$

where

$$s_0 \equiv \frac{2|\Omega|^2}{\Gamma^2} = \frac{I}{I_{sat}} \tag{1.25}$$

and

$$I_{sat} \equiv \frac{\pi hc}{3\lambda^3\tau} \tag{1.26}$$

where I_{sat} is the saturation intensity corresponding to the intensity required for a resonant atom to spend $1/4$ of its time in the excited state

Using equation (1.23) one can identify the two general components of the total force. The first term of (1.23) is proportional to the detuning between the laser and the atomic transition frequency Δ_a and the second term is proportional to the decay rate Γ of the atom. However their contribution to the total force is determined by the real and imaginary part of the logarithmic derivative of Ω, as defined in (1.20). Since q_r and q_i depend on the electric field, strictly speaking on whether it is a travelling or standing wave, the force can be predominantly due to the field detuning or the scattering rate and hence give the contribution to two different forces which will be described in detail in the following sections.

1.3 Scattering or Radiation Pressure Force

Consider a travelling wave of the electric field given by

$$E(z) = \frac{E_0}{2}\left(e^{i(kz-\omega t)} + c.c.\right) \tag{1.27}$$

The Rabi Frequency for such a wave can be found using the definition given earlier in (1.19) where the wavefunction $\Psi(\vec{r},t)$ has been expanded in the terms of ϕ_n such as

$$\Psi(\vec{r},t) = \sum_k c_k(t)\psi_k(\vec{r})e^{-i\omega_k t} \tag{1.28}$$

Since the amplitude of the wave does not depend on z its gradient is zero so its logarithmic derivative is zero too and hence $q_r = 0$.

The phase of the wave contributing to Ω is not zero however if after applying RWA the only surviving part is a negative frequency component whose derivative equals simply the wave number k hence $q_i = k$.

When $q_r = 0$ and $q_i = k$ the force equation (1.23) reduces to

$$F = \frac{1}{2}\hbar k\Gamma\frac{s}{1+s} \tag{1.29}$$

and substituting the saturation parameter defined earlier in (1.24) gives

$$F_{scat} = \hbar k \, \frac{\Gamma}{2} \, \frac{s_0}{1 + s_0 + (2\Delta_a/\Gamma)^2}. \tag{1.30}$$

Equation (1.30) can be also written in terms of the population of the excited state

$$\rho_{ee} = \frac{1}{2}(1 - w) = \frac{s}{2(1 + s)} = \frac{1}{2} \frac{s_0}{1 + s_0 + \left(\frac{2\Delta_a}{\Gamma}\right)^2} \tag{1.31}$$

where w is the population difference

$$w = \frac{1}{(1 + s)} \tag{1.32}$$

so that

$$F_{scat} = \hbar k \Gamma \rho_{ee} \tag{1.33}$$

It can be seen now that the force saturates to a maximum value $\hbar k\Gamma/2$ since the maximum value of ρ_{ee} is $1/2$.

The mechanism of the radiation pressure force acting on an atom originates from the fundamental laws of conservation of energy and momentum during the absorption and emission of light. An atom can emit a photon in two ways: by spontaneous emission or stimulated emission. The scattering force can be understood as a result of cycles of absorption followed by spontaneous emission (absorption and stimulated

emission play more important roles in dipole cooling which will be explained in the following chapters)

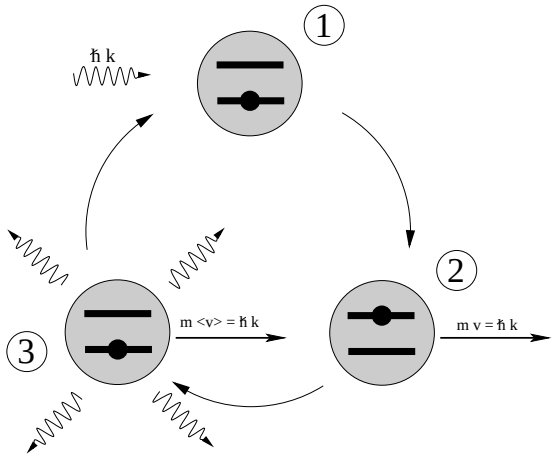

Figure 1.2: Photon picture of the scattering force: a two level atom, initially in the ground state, absorbs a photon with momentum $\hbar k$ (1) , excited atom increases its velocity by $\hbar k/m$, in the direction of the incoming beam (2) , the internal energy is released by spontaneous emission of a photon, in a direction described by a symmetric probability distribution so the average velocity change is zero (3)

Consider an atom with mass m absorbing a photon with energy $\hbar\omega$ (fig. 1.2). The energy of the photon that has been absorbed by an atom is converted into its internal energy i.e. the atom ends up in an excited state. However a photon carries also a momentum $\hbar k$ that after absorption causes the atom to recoil in the direction of the incoming light and changes its velocity v by an amount $\hbar k/m$. The excited atom does not stay in this state forever and soon returns to the ground state by spontaneously emitting a photon. The conservation of momentum during the emission causes another recoil in the opposite direction to the emitted photon. The recoil caused by an absorption is always in the direction of the laser beam, however the second recoil due to spontaneous emission is completely random in direction. For that reason the spontaneous emission does not contribute to the net force and

after each cycle an atom changes its velocity by $\hbar k/m$. Note that the scattering force is dissipative because the reverse of spontaneous emission is not possible and therefore the action of the force cannot be reversed. The scattering force can then be used to slow and cool atoms [11, 12, 13, 14, 15, 16].

In contrast to the scattering force the dipole force is conservative and without a dissipative mechanism can be used to trap atoms; this will be discussed in more detail in the following chapters.

1.3.1 Doppler Cooling and Optical Molasses

The concept of using laser radiation for the purpose of cooling atoms was first proposed by Hänsch and Schawlow in 1975 [6]. The idea was to illuminate an atom with laser beams of the same frequency, intensity and polarisation but directed against each other. The lasers are also slightly detuned to the red of the atomic frequency ($\omega_L < \omega_a$) [17]. For the atom at rest the two radiation pressure forces exactly balance each other and the net force is equal to zero. However, an atom moving slowly along the light beams sees oncoming light Doppler shifted closer to the resonance whereas co-propagating light is shifted further away from the resonance. As shown in fig. 1.3 the atom scatters more light from the counter-propagating beam than from the co-propagating beam. The atom therefore experiences a net friction force and is slowed. Such a method of using radiation pressure to slow atoms is called optical molasses; one of the most common cooling methods used [18, 19].

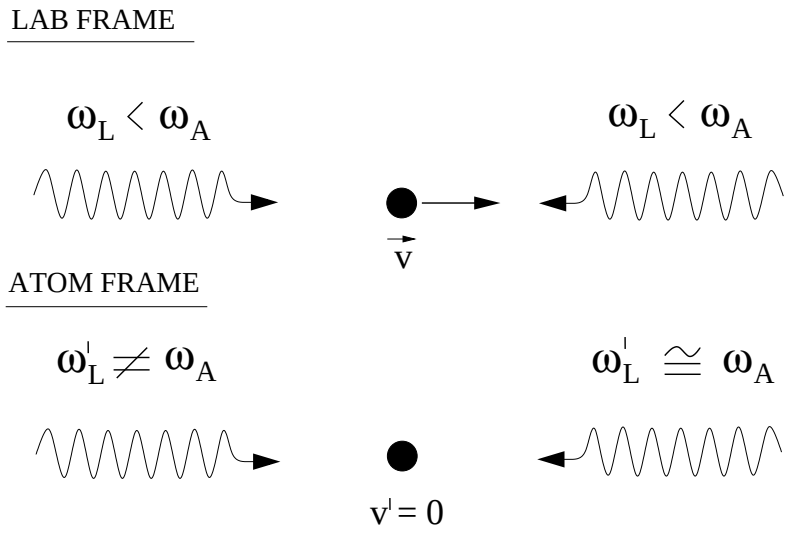

Figure 1.3: Doppler cooling in 1D, resulting from the imbalance between the radiation pressure forces of two counterpropagating laser waves

It is possible to demonstrate the existence of a friction force using the expression derived for the scattering force (1.30). The scattering force can be written in terms of the saturation intensity for the case of opposing directions (+) and (-) using

$$F_{\pm} = \pm\,\hbar k\,\frac{\Gamma}{2}\,\frac{s_0}{1+s_0+(2\Delta_a \mp kv/\Gamma)^2} = \pm\hbar k\,\frac{\Gamma}{2}\,\frac{I/I_{sat}}{1+I/I_{sat}+(2\Delta_a \mp kv/\Gamma)^2} \tag{1.34}$$

It is now straightforward using the above equation to estimate the total force on an atom in optical molasses. For the low intensity case the forces from each of the light beams can be simply added to give

$$F_{total} = \hbar k \, \frac{\Gamma}{2} \left[\frac{I/I_{sat}}{1 + I/I_{sat} + \left(\frac{2(\Delta_a - kv)}{\Gamma}\right)^2} - \frac{I/I_{sat}}{1 + I/I_{sat} + \left(\frac{2(\Delta_a + kv)}{\Gamma}\right)^2} \right] \tag{1.35}$$

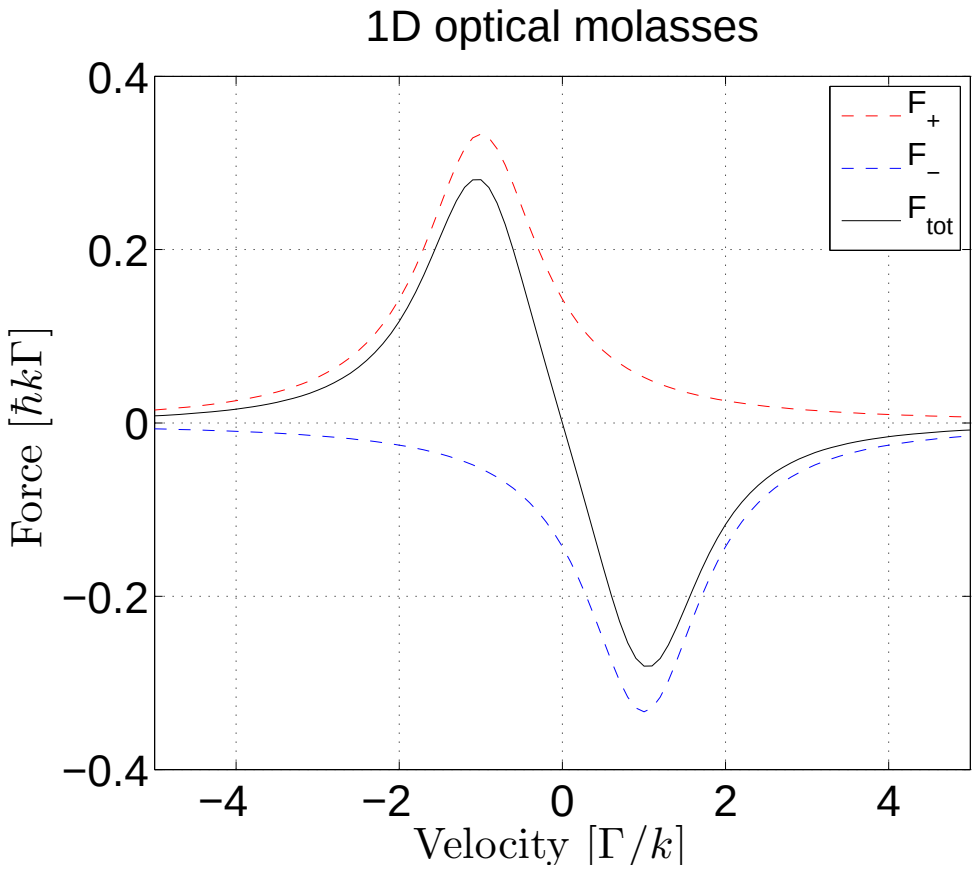

Figure 1.4: Velocity dependence of the light pressure force in a one-dimensional optical molasses. The dashed lines show the two components of the force (eq. 1.34) in the $\pm k$ direction. The solid line shows the sum of the two forces, which is linear for small velocities. The parameters used are: $s_0 = 2, \Delta_a = -\Gamma$

$$F_{total} \cong \frac{8\hbar k^2 \Delta_a s_0 v}{\Gamma \left(1 + s_0 + \left(\frac{2\Delta_a}{\Gamma}\right)^2\right)^2} \equiv -\beta v \tag{1.36}$$

where β is the velocity damping rate, defined as

$$\beta = -\frac{8\hbar k^2 \Delta_a s_0}{\Gamma\left(1 + s_0 + \left(\frac{2\Delta_a}{\Gamma}\right)^2\right)^2} \tag{1.37}$$

Figure 1.4 shows the velocity dependence of the optical damping forces for one-dimensional optical molasses as calculated from eq. (1.34). Each of the counter-propagating beams exerts a force with a Lorentzian velocity dependence. The dashed lines show the two components of the force in $\pm k$ direction. The solid line shows the sum of the two forces, which has a linear dependence for small velocities.

1.4 Dipole Force

An atom in the presence of an oscillating electric laser field acquires an electric dipole moment that interacts with the laser field. If the field is spatially inhomogeneous (as in a standing wave or a focussed Gaussian laser beam) the interaction varies in space and therefore can be described in terms of a spatially varying potential. The force associated with such a potential is proportional to the gradient of the field's intensity and is called the gradient or dipole force.

In order to find the mathematical expression of the dipole force, we can follow a similar derivation as for the scattering force that has been shown in section 1.3. Here, in contrast, we consider a standing wave for which the electric field equation can be written as

$$E(z) = E_0 cos(kz) \left(e^{-i\omega t} + c.c.\right) \tag{1.38}$$

In calculating the Rabi frequency we again find that only the negative component of (1.38) survives the RWA, but the gradient does not depend on it and equals zero. However for a standing wave the gradient of the amplitude is non-zero and hence the logarithmic components of Ω become $q_r = -ktan(kz)$ and $q_i = 0$. If submitting this to the general force equation (1.23) gives:

$$F_{dip} = \frac{\hbar s}{(1+s)}\ \delta\ k\ tan(kz) \tag{1.39}$$

which for the value of the local saturation parameter s becomes:

$$F_{dip} = \frac{2\hbar k \delta s_0 sin2kz}{1 + 4s_0 cos^2 kz + (2\delta/\gamma)^2} \tag{1.40}$$

where s_0 is the saturation parameter corresponding to each of the two oppositely directed travelling waves that constitute the standing wave.

It needs to be emphasised that unlike the scattering force, the dipole force does not saturate and can be made very large for large intensities [10, 13, 20].

1.4.1 AC-Stark Shift

The dipole force originates from the dynamical shift of the atom's energy levels in the presence of the external field [21, 22, 23]. This energy shift, called the light shift or AC Stark shift, is the energy displacement of the ground level ΔE_g, which is directly proportional to the light intensity and inversely proportional to the detuning, so that $\Delta E_g = \frac{\hbar\Omega^2}{4\Delta_a}$, as shown in fig. 1.5.

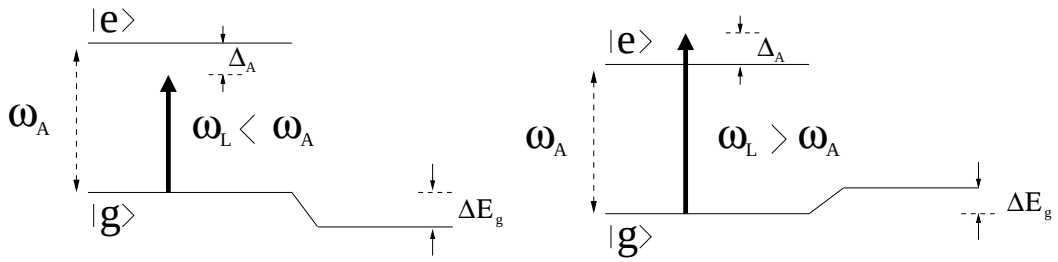

(a) $\Delta_a < 0$ (b) $\Delta_a > 0$

Figure 1.5: Light shift of the ground state $|g\rangle$ of an atom produced by a non-resonant light excitation detuned to the red side of the atomic transition (a) or to the blue side (b). This is known as a AC-Stark shift.

It is the gradient of this shift that produces a dipole force on an atom. When, for

instance, the frequency of the external field is tuned below the atomic resonance (Δ_a is negative), the energy shift becomes negative and the potential energy is minimum there (fig. 1.5a). Since the shift increases while the intensity increases the atom is attracted to the regions of the high field intensity (an atom is called a high-field seeker). On the other hand if the frequency of the laser is tuned above the atomic resonance ($\Delta_a > 0$) the shift becomes positive and the potential creates a hill that is repulsive to the atom (in this case the atom is called a low field seeker, fig. 1.5b).

The dipole force can be used to trap atoms in high intensity or low intensity regions depending on the detuning [16, 24, 25]. The simplest form of such a trap is a single focussed TEM_{00} Gaussian laser beam red detuned to the atomic resonance. Here atoms will be attracted to the focal point of the beam and its centre where the intensity is greatest. Such traps are also called optical tweezers since they can be used to "grab" and move dielectric objects, including e.g biological samples. Similarly, low field seekers can be trapped using the "hollow" modes e.g LG_{0n}, $(n = 1, 2, \ldots, n)$ laser beam mode, which have an intensity minimum on the beam axis (hollow beam).

For the case of standing waves that are also characterised with an inhomogeneous intensity distribution atoms will be attracted towards the field antinode where the intensity is maximum (for red detuned light) or pushed away from antinodes toward nodes (for blue detuned light), where the intensity is minimum. This property lies behind the principle of the cavity trapping (cooling) methods which with an additional dissipative mechanism can be used to slow and cool atoms [21, 23, 26, 27, 28, 29].

1.4.2 Sisyphus Cooling

Sisyphus cooling is a method of cooling which involves the dipole force. A proper treatment of Sisyphus cooling requires a quantum-mechanical description of the atom-light interaction. In the so called dressed-atom picture the atom and the field are not treated separately but are considered as a single system [30, 31, 32, 33].

In the dressed-atom picture the energy of the atom and the field are added together. If we initially ignore the interaction of the field the two states $|g\rangle$ and $|e\rangle$, additionally characterised by the number of photons in the field n, form a ladder of energy manifolds, separated by the photon energy $\hbar\omega_L$. The states in each manifold are of the form: $|g,n\rangle$ and $|e,n-1\rangle$, $|e,n\rangle$ and $|g,n+1\rangle$ as shown in fig. 1.6a. If the atom-field coupling is included the energy levels split (due to the AC-Stark shift) and are separated by the energy proportional to Rabi frequency $\hbar\Omega$ (fig. 1.6b). The dressed states associated with the energy shift $|1,n\rangle$ and $|2,n\rangle$, $|1,n-1\rangle$ and $|2,n-1\rangle$ are mixtures of the basic states such that:

$$|1,n\rangle = \quad cos\theta|e,n\rangle + sin\theta|g,n+1\rangle \tag{1.41}$$

$$|2,n\rangle = -sin\theta|e,n\rangle + cos\theta|g,n+1\rangle \tag{1.42}$$

where the angle θ is given by

$$tan2\theta \equiv -\Omega/\Delta_a \tag{1.43}$$

The mechanism of Sisyphus cooling is based on the fact that the energies of the dressed states, and so the energy shift, vary in space, i.e in the direction of the atomic motion. This takes place when the laser intensity is not homogeneous as is

the case in a standing wave optical field.

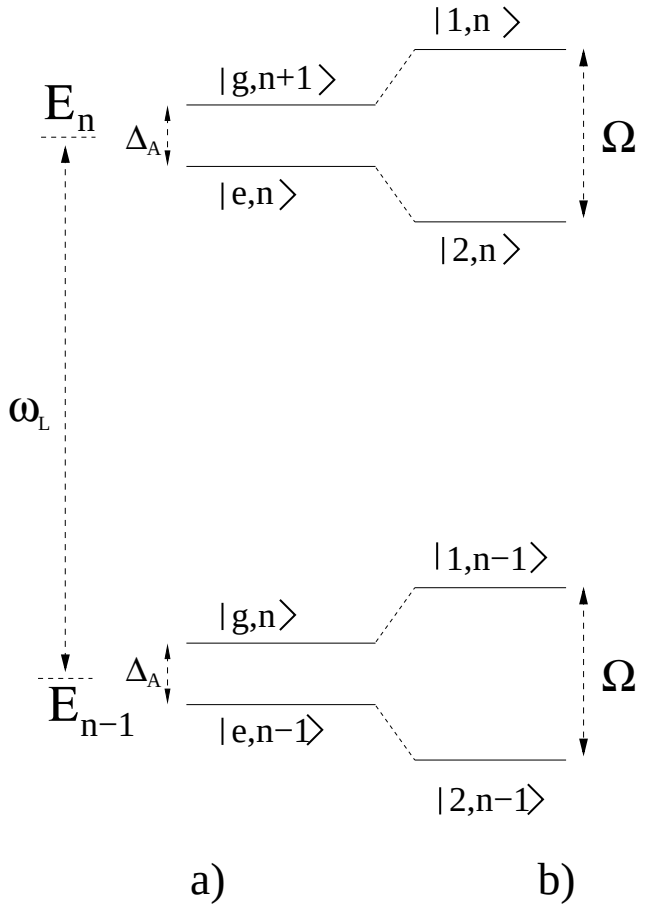

Figure 1.6: Dressed-atom energy diagram for $\Delta_a > 0$. a) when the coupling is not taken into account, b) including laser-atom coupling.

Consider an atom moving through the dressed atom potentials created by the blue detuned laser light, as shown in fig. 1.7. Lets assume the atom starts in the ground state at a field node with $n+1$ photons in the field. The atom cannot undergo a spontaneous emission at such a place since it is in a pure ground state and hence will continue its trajectory. While climbing the potential hill created by the field intensity the atom increases its potential energy but at the same time decreases its kinetic energy. As the intensity increases the Rabi frequency increases so at the antinode of the standing wave the dressed atoms have a large contribution from the excited state and transition $1 \rightarrow 2$ can occur. If the decay is to another $|1\rangle$ state in a different pair its motion is unaffected. But if the decay is to level $|2\rangle$ the atom finds itself again at the bottom of the potential well and will continue climbing until reaching the next hill. In contrast to the upper sideband, here the transition $2 \rightarrow 1$ will occur preferentially at the node of the wave where the atom is in a pure excited state with n photons. Consequently the most probable transitions $1 \rightarrow 2$ and $2 \rightarrow 1$ will force the atom to "see" more uphills than downhills and it will be slowed down.

This type of cooling mechanism is generally referred to as Sisyphus cooling since on average atoms spend most time climbing hills losing kinetic energy, in analogy to the Greek myth about Sisyphus. This mechanism is particularly interesting since it provides cooling for a laser field tuned above the atomic resonance, contrary to Doppler cooling. However it works for "slow" particles only, i.e. particles that move a distance of $\lambda/4$ (from the node to the antinode of the standing wave) within, or less, its natural life time.

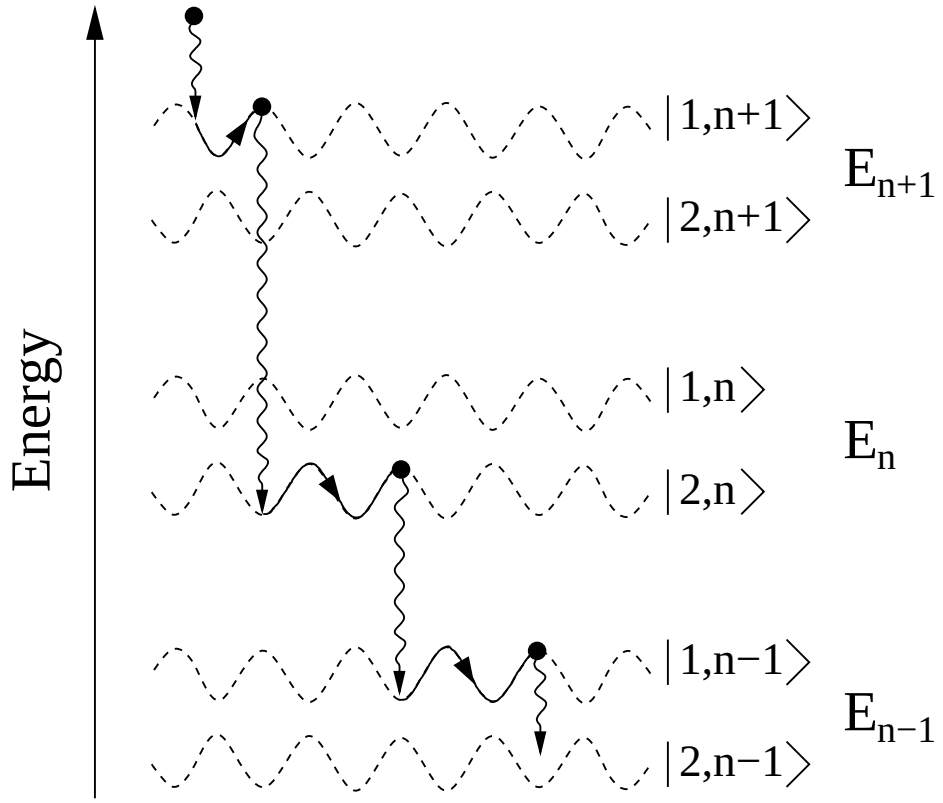

Figure 1.7: Sisyphus cooling of an atom in a standing wave for $\Delta_a > 0$. The dashed lines represent the spatial variation of the dressed atom energy levels and the full lines represent the "trajectory" of a slowly moving atom. The moving atom sees more "uphills" than "downhills" (figure adapted from Ref. [30])

1.5 Cavity Cooling

Doppler cooling is based on the scattering force which relies on a complicated mechanism of closed cycles of absorption and spontaneous emission of atomic population and is limited to species with simple spectroscopic structures. It has been proven to be very successful for cooling alkali and alkaline earth metals but is rather inaccessible to cool more complex systems, like molecules which do not have closed atomic transitions. Cavity cooling is based on the dipole force which does not rely on the internal structure of an atom but uses the off-resonant interaction between an optical coherent field and a polarisable particle. However, the dipole force is a conservative force and requires an additional dissipative mechanism. In cavity cooling the dissipation channel is via decay of the optical field that is coupled to an atom or a molecule [34, 35].

1.5.1 Historical Background

The first complete cavity cooling scheme was proposed by Vuletić and Chu in 2000 [36]. The model was addressed to the translational motion of polarisable particles at low saturation and large detuning from the particles' resonances. The authors pointed out that this scheme should be applicable to molecules or multilevel atoms as the method is independent of the particles' internal level structure [27, 35, 37, 38]. Another potential advantage of the scheme was the final achievable temperature which, in this case, is limited by the dipole force heating in a two-level system [13, 30] and can be at or below the recoil limit.

In 2002, Domokos and Ritsch [39] proposed a different set-up and suggested illuminating atoms in the cavity from the side instead of sending the pump light directly into the cavity. In such a configuration the cavity-mediated atom-atom coupling

can lead to strong cooperative effects and enhance cooling and trapping. Such an effect strongly depends on the number of atoms inside the cavity and the strength of the pump field (the origin of the cooperative effect in this configuration will be explained in chapter 3).

Results from the first cavity cooling experiment were reported in 2003 by Chan, Black and Vuletić [40, 41, 42, 43]. The experimental setup consisted of a cavity in which 3×10^6 Cesium atoms (freely falling under the gravity force) were illuminated by two laser beams sent perpendicularly to the cavity axis. Observed results showed that one-third of the falling sample was stopped by the standing wave cavity field. In addition, strong deceleration of up to $1500 m/s^2$ and cooling to temperatures as low as $7\mu K$ was observed.

1.5.2 Cavity Geometries

There are two main cavity geometries taken into account in a cavity cooling setups: Fabry-Perot cavity and a ring cavity. In the first case atoms can be illuminated either injecting the pump through a cavity mirror or directly illuminating the atoms, which then scatter light into the cavity mode. While in the first case some field always builds up even in the absence of atoms, the second case needs the presence of particles to populate the cavity mode via scattering. Hence the latter case exhibits more intriguing physical effects such as self-ordering of the atoms in the optical potentials. In a Fabry-Perot cavity in spite of the direction of a pump field, potentials built by an oscillating field are fixed in space and cannot travel inside the cavity. In the second case of a ring cavity this restriction can be removed. The different boundary conditions for the field in the ring cavity case allow the positions of the field nodes/antinodes and hence the optical potentials to move in the cavity.

1.5.3 Results from the Cavity Cooling Simulations Presented in this Work

The following chapters present analytical and numerical results from cavity cooling simulations. It is important to mention that this work has been greatly influenced by the cavity cooling experiment that has been carried out at the University College of London (UCL) by Prof Ferruccio Renzoni's group. The experiment involved a MOT chamber with a pre-cooled cloud of $\sim 10^6$ Cs^{55} atoms and a vertical cavity, optically pumped along the cavity axis with an $852nm$ laser. Initially the Cesium atoms are fed to the MOT and pre-cooled to a temperature of $160\mu K$. After the MOT is switched off, the atoms are trapped and cooled in the standing wave cavity field.

The parameters used in the experiment are listed below [44]:

Number of atoms:	N	$\sim 1 \times 10^6$
Cavity linewidth:	κ	$= 10.0 \times 10^6\ Hz$
Laser wavelength:	λ	$= 852.4 \times 10^{-9}\ m$
Cs decay rate:	Γ_{lw}	$= 32.89 \times 10^6\ Hz$
Coupling constant:	g_0	$= 222.38 \times 10^3\ Hz$
Cs mass:	m	$= 2.21 \times 10^{-25}\ kg$
Initial temperature:	T_{ini}	$= 160.0 \times 10^{-6}\ K$
Pump-atom detuning:	Δ_A	$= (-250 : 250) \times 10^6\ Hz$
Laser power:	P	$\leq 0.3\ W$

where N is the number of atoms, κ is the cavity decay rate, Γ_{lw} is the spontaneous emission linewidth, g_0 is the measure for the atom-cavity coupling strength, m is the Cesium mass, T_{ini} is the initial temperature of the atomic cloud that interacts

with the cavity field, $\Delta_a = \omega_p - \omega_a$ is the laser-atom detuning and P is the laser power. Corresponding scaled parameters have been used in the series of numerical simulations for various cavity configurations and are presented in this work. This work is organised as follows:

Chapter 2 contains the derivation of the cavity cooling model (particle model) for the single atom and many atoms confined inside a Fabry-Perot cavity pumped along the cavity axis (here called the cavity-pump case). Obtained equations are solved numerically and the figures characterising the most important features, including the cooling rates of this scheme are presented. Afterwards, with the respect to the particle model of the cavity pump configuration, equivalent model based on a distribution-function (Vlasov model) is developed. Both models are then compared and the numerical results are analysed.

Chapter 3 introduces cooling of atoms illuminated from light sent perpendicularly to the cavity axis (here called atom-pump case). This chapter has a similar structure to that of chapter 2 for the cavity-pump case and hence contains a derivation of the particle model, main features of this model and numerical solutions obtained from the solution of its equations. Accordingly the distribution function, Vlasov model is derived for the same atom-pump configuration and the results from numerical simulations are compared with the particle model.

Chapters 4 and 5 present the semi-classical models of the cavity-pump and the atom-pump configuration, respectively. In both cases the semi-classical models are derived and compared with equivalent classical models. The models are first compared analytically and then verified using numerical results. Additionally, chapters 4 and 5 contain numerical simulations of the semi-classical models for both the cavity pump and the atom-pump configurations for the case of blue detuned light. The results from the simulations are presented and analysed.

In chapter 6 the possibility of slowing and cooling atomic gas using a phase-modulated pump field is being investigated. This model assumes atoms being confined in a high-quality ring cavity illuminated by light sent through one of the cavity mirrors. Unlike in the Fabry-Perot cavity in this configuration the optical potentials built up by the field can freely travel inside the cavity. Hence, three different regimes, in which both the field and the atoms reveal qualitatively different behaviour, are identified. The atom-field interaction characteristics for each regime are presented and analysed using results obtained from numerical simulations of the model equations.

In chapter 7 all results from this work are reviewed and summarised.

Chapter 2

Cavity-Pump Configuration

The following chapter introduces the cavity cooling model for cases where a single atom and many atoms are confined inside a Fabry-Perot cavity pumped through one of the cavity mirrors, along the cavity axis. Equations for the particle model and the alternative Vlasov model will be derived and the results from the numerical simulation of both models will be compared and analysed.

2.1 Classical Derivation of Single Atom Cooling

Let us consider a system consisting of a single atom inside an optical cavity, pumped by an external field injected through one of the mirrors, with a standing wave light field far detuned from any atomic transition (fig. 2.1).

The cavity field induces a dipole moment in the atom which in turn contributes to the plane wave electric field as a driving term in Maxwell's wave equation [35]

$$\begin{aligned} &-\frac{\partial^2}{\partial x^2}E(x,t)+\frac{1}{c^2}\frac{\partial^2}{\partial t^2}E(x,t)+\mu_o\sigma\frac{\partial}{\partial t}E(x,t) \\ &=-\mu_o\frac{\partial^2}{\partial t^2}P(x,t)+\mu_o\sigma\frac{\partial}{\partial t}E^{ext}(x,t)\ . \end{aligned} \tag{2.1}$$

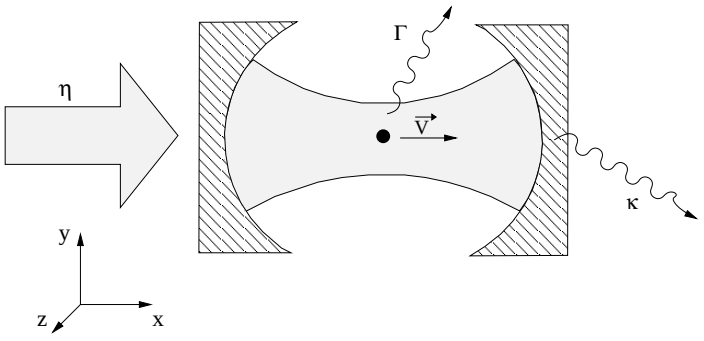

Figure 2.1: Particle moving inside a driven optical cavity, pumped along the cavity axis. The cavity pumping rate, spontaneous loss rate and cavity decay rate are determined by the parameters η, Γ and κ respectively

where σ is the conductivity of the cavity mirrors, μ_o is the magnetic permeability, c is the speed of light, $P(x,t)$ is the polarisation of the atom and E^{ext} is the electric field of the external pump field. The third term on the LHS and second term on the RHS of (2.1) describe damping and external pumping of the cavity, respectively. The electric field and polarisation can be written as

$$E(x,t) = \mathcal{E}(t)e^{-i\omega_p t}\ u(x) + c.c. \tag{2.2}$$

$$P(x,t) = \mathcal{P}(t)e^{-i\omega_p t}\ u(x) + c.c. \tag{2.3}$$

where u(x) is the intracavity mode function - $cos(kx)$ with wave number k. Substituting eq. (2.2) and (2.3) into (2.1), finding the derivatives and assuming that $\mathcal{E}$ and $\mathcal{P}$ are slowly varying amplitudes ($|\dot{\mathcal{E}}| \ll \omega_p|\mathcal{E}|$ and analogously for $\mathcal{P}$ and $\mathcal{E}^{ext}$) one can rewrite eq. (2.1) as

$$\dot{\mathcal{E}} + (\kappa - i\Delta_c)\mathcal{E} \approx \frac{i\omega_p \mathcal{P}}{2\epsilon_o} + \kappa\mathcal{E}^{ext}\ . \tag{2.4}$$

Here Δ_c is the detuning between the pumping field and cavity frequency ($\Delta_c = \omega_p - \omega_c$) and $\kappa = \sigma/2\epsilon_o$ is the cavity decay rate.

The dynamics of the atomic dipole can be modelled as an elongation of an elastically bound electron under the influence of an electric field:

$$\ddot{y}(t) + 2\Gamma\dot{y}(t) + \omega_o^2 y(t) = \frac{e}{m} E(x_a, t) \ , \tag{2.5}$$

where x_a is the atomic position, m is the electron mass, e is the charge, Γ is the scattering rate and where we have introduced the slowly varying complex amplitude $Y(t)$ via

$$y(t) = Y(t)e^{-i\omega_p t} + c.c. \tag{2.6}$$

Inserting eq. (2.6) into eq. (2.5) and solving for steady state one obtains:

$$Y(t) = \frac{e\ \mathcal{E}(t)/m}{2\omega_p(-i\Gamma + (\omega_o^2 - \omega_p^2)/2\omega_p)}\ cos(kx_a) \ . \tag{2.7}$$

The polarisation density can be defined as $P(x,t) = ey(t)\ \delta(x - x_a)/A$ where δ is a Dirac delta function and A is the cavity cross-section. Using definition (2.3) and defining a "macroscopic" polarisation $\mathcal{P}(t) = (2/d)\int_{-d/2}^{d/2} dx P(x,t) cos(k,x)$, where d denotes cavity length, it is possible to obtain the following expression for the slowly varying amplitude:

$$\mathcal{P}(t) = i\ \frac{e^2}{(m\omega_p V)} \frac{cos^2(kx_a)}{(\Gamma - i\Delta_a)} \mathcal{E}(t) \ . \tag{2.8}$$

where Δ_a is the frequency detuning $\omega_p - \omega_o$.

Substituting (2.8) into (2.4) one obtains

$$\dot{\mathcal{E}}(t) = [-\kappa - \gamma(x_a) + i\Delta_c - iU(x_a)\ ]\mathcal{E}(t) + \kappa\mathcal{E}^{ext}\ , \tag{2.9}$$

where

$$\gamma(x) = \frac{\Gamma}{\Gamma^2 + \Delta_a^2} g_o^2 cos^2(kx)\ , \tag{2.10}$$

$$U(x) = \frac{\Delta_a}{\Gamma^2 + \Delta_a^2} g_o^2 cos^2(kx)\ . \tag{2.11}$$

The parameter $\gamma(x)$ can be understood as the total rate at which the atom scatters light and $U(x)$ as the frequency shift of the cavity due to the interaction with the atom. Here $g_o = |e|/\sqrt{(2V\epsilon_o m)}$ is a measure of the atom-cavity coupling strength.

The dipole force acting on the atom is given by

$$F(x_a) = \nabla[e\ y(x_a, t)E(x_a, t)], \tag{2.12}$$

so substituting (2.2), (2.6) and (2.7) into (2.12) produces

$$F(x_a) = -\nabla\left[\frac{e^2}{2\omega_p m}\frac{\Delta_a}{\Gamma_a^2 + \Delta_a^2}\mathcal{E}(t)cos^2(kx_a)\right]. \tag{2.13}$$

Introducing the effective pumping term η and rewriting (2.9) and (2.13) in terms of a dimensionless parameter α, associated with the average cavity photon number:

$$|\alpha^2| = \frac{\epsilon_o|\mathcal{E}^2|V}{\hbar\omega_p} \tag{2.14}$$

it is finally possible to write the following set of equations for the atom-cavity dynamics:

$$\frac{d\alpha}{dt} = [-\kappa - \gamma(x) + i\Delta_c - iU(x)\ ]\alpha + \eta \tag{2.15}$$

$$\frac{dp}{dt} = -\hbar|\alpha|^2 \frac{d}{dx}U(x) \tag{2.16}$$

$$\frac{dx}{dt} = \frac{p}{m} \tag{2.17}$$

Equation (2.15) describes the time evolution of the field amplitude; here α is the complex, dimensionless parameter whose absolute squared value $|\alpha|^2$ is associated with the average photon number, η characterises the driving laser strength given by the free-space Rabi frequency and κ is the total cavity decay rate. The parameter $\gamma(x) = \gamma_0\ cos^2(kx)$ can be understood as the total rate at which the atom scatters light where

$$\gamma_o = \frac{\Gamma}{\Gamma^2 + \Delta_a^2} g^2, \tag{2.18}$$

describes the absorptive effect of the atom as it broadens the resonance line of the cavity.

Equation (2.16) and (2.17) are the equations of motion of the atomic centre-of-mass, where x refers to the position of the atom and p to its momentum. $U(x) = U_0\ cos^2(kx)$ is the frequency shift of the cavity due to the interaction with the particle, where

$$U_o = \frac{\Delta_a}{\Gamma^2 + \Delta_a^2} g^2 \tag{2.19}$$

describes the dispersive effect of the atom as it shifts the resonance line of the cavity.

In order to understand the basic idea of the cavity cooling mechanism let us consider a massive point-like polarisable particle strongly coupled to a high finesse optical cavity pumped directly along the cavity axis (fig. 2.1). Depending on the configuration a laser field, which can be pumped along the cavity axis or perpendicularly, forms a standing wave cavity mode to which an atom is coupled. Because of the electric dipole moment the field detuned from any atomic transition exerts a force on the particle and consequently modifies its momentum and position inside the cavity.

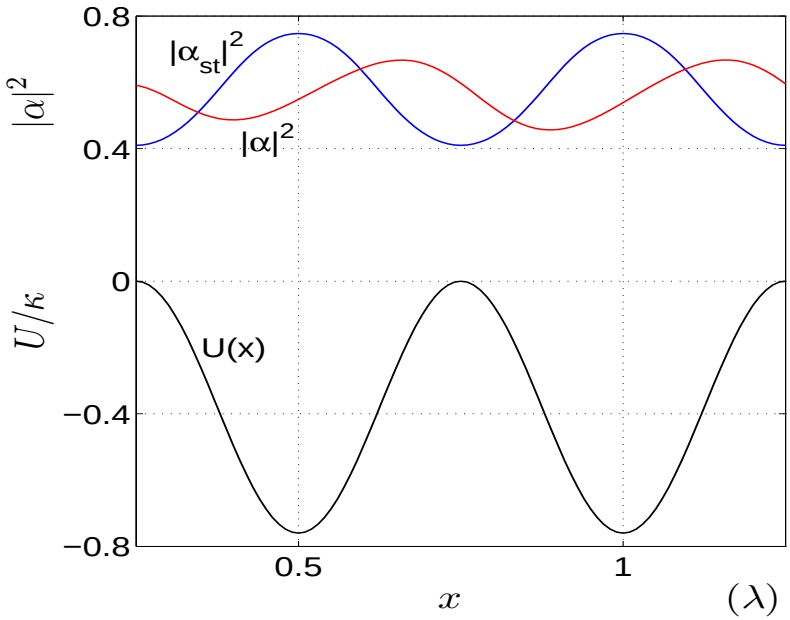

Figure 2.2: Potential $U(x)$ and intracavity intensity $|\alpha|^2$ versus particle position x – red curve when particle moving, blue when steady (figure adapted from Ref. [34])

The detuning between the field and an atom (Δ_a) plays a significant role in the whole system dynamics. If $\Delta_a < 0$, we say the field is red detuned and the force is directed along the gradient of intensity so an atom is attracted to an antinode. For blue detuning, $\Delta_a > 0$, the force is directed against the gradient of intensity and a particle will be pushed towards a node. In turn, due to atom-field coupling the particle's position strongly influences the field amplitude.

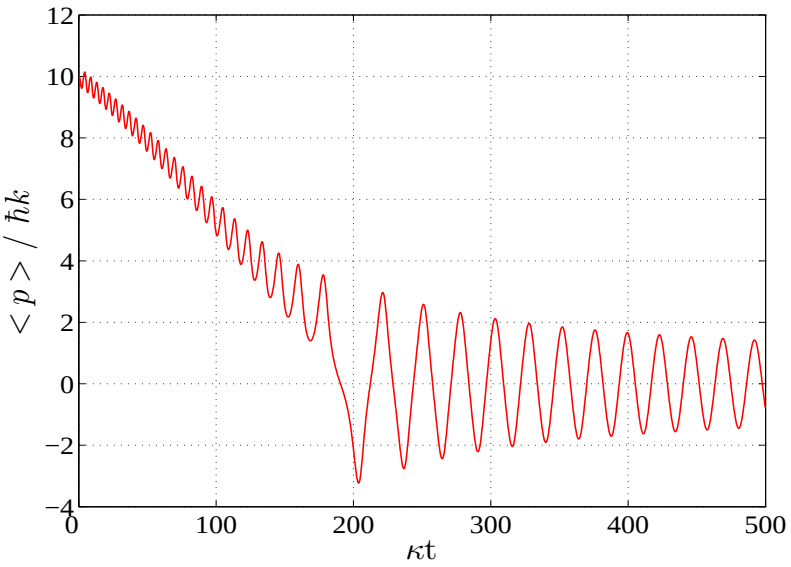

Figure 2.3: Time evolution of particle momentum. The parameters used are: $U_0 = 0.76\kappa$, $\gamma_0 = 0.07\kappa$, $\Delta_c = 1.2\kappa$ (figure adapted from Ref. [34])

For a typical cooling regime, and assuming $\Delta_a < 0$, the maximum field amplitude will be obtained when the particle sits at an antinode of a standing wave and will be minimum when the particle sits at a node (fig. 2.2). For a particle with non-zero momentum, because of the finite cavity response time, the maximum field intensity will be attained after the particle passed the minimum potential. Thus, for properly scaled values this atom-field cross-talk can be controlled in a way that the particle will climb potential hills at times of higher intracavity intensity and run down at

times of lower intracavity intensity. Over an entire cycle the particle will lose its kinetic energy and after being slowed it can be trapped in a single potential well (fig. 2.3),[34]. More results from the numerical simulations of the particle model, including cooling rates for the case of many particles inside the cavity will be shown in the next sections.

2.2 Cavity Cooling Including Many Particles - Particle Model

In this section, the model derived in section 2.1 is extended to describe the case where many particles are coupled to the same cavity mode, as shown in fig. 2.4. Because of the presence of many atoms, the cavity resonance shift is now due to the total phase shift induced by the position of all the atoms inside the cavity [45].

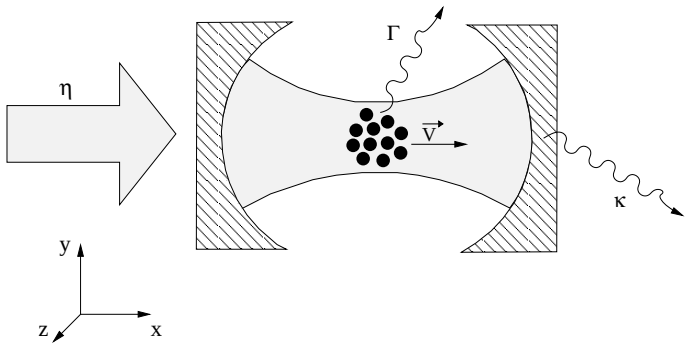

Figure 2.4: Cavity resonator with many particles coupled to the light field. The cavity pumping rate, spontaneous loss rate and cavity decay rate are determined by the parameters η, Γ and κ respectively

Similarly, the absorptive effect is a function of the total scattering from each of the particles separately. Hence equations (2.15) , (2.16) & (2.17) become:

$$\frac{d\alpha}{dt} = [-\kappa - \gamma_o \sum_j cos^2(kx_j) + i\Delta_c - iU_o \sum_j cos^2(kx_j)\ ]\alpha + \eta \tag{2.20}$$

$$\frac{dp_j}{dt} = -\hbar U_o |\alpha^2| \frac{d}{dx} cos^2(kx_j) \tag{2.21}$$

$$\frac{dx_j}{dt} = \frac{p_j}{m} \tag{2.22}$$

where the parameters $\alpha, \kappa, \gamma(x), U(x), \Delta_c$ and η represent the same physical quantities as in a single atom configuration (section 2.1) and $j = 1...N$ is the particle

index.

In the particle model the knowledge of the system at a given time requires information about the instantaneous position and momentum of each of the particles. This information in turn contributes to the evolution of the total field intensity and phase as described by eq. (2.20). The whole idea is to use that interplay and find parameters for which cooling can be obtained. The cooling mechanism for the case of many particles in the cavity is similar to the single atom case. For red particle-field detuning $U_0 < 0$ the particles are drawn towards the field intensity maxima at the mode antinodes, as explained earlier in section 1.5. This increases their average coupling to the field and thus enlarges the effective refractive index of the cloud shifting the cavity resonance towards a lower frequency. Under suitable operating conditions, when the pump frequency is also below the cavity resonance, such a shift decreases the pump-cavity frequency mismatch and leads to an increase in the cavity photon number. In turn this deepens the optical potential and further confines the cloud near the antinodes.

In reality the position and momentum distribution in an atomic cloud is fully random. In the cavity pump configuration the external field does not provide any correlation between the motion of the atoms so in principle the cross-talk between particles should increase the trapping time. Numerical solutions of eqs. (2.20) - (2.22) provide information about certain parameters e.q. number of particles or pump strength that can influence the cooling of the sample.

2.2.1 Scalability of the Cavity Pump Configuration

Numerical simulations using the classical model (eqs. (2.20 - 2.22)) predict faster cooling for small number of particles and slower cooling for larger ensembles. It is important to mention that this model does not include spontaneous emission and any spread of the atomic momentum is due to interaction with the classical cavity field only. The cavity pump configuration is characterised by strong scalability [45, 46]. Since U_0 is the cavity frequency shift due to the interaction with the atom, hence increasing the number of particles by a factor r, dividing the interaction potential U_0 by r and increasing the pump strength by $\sqrt{r}$ should in principle lead to similar results.

In the following example this scalability law has been applied to initial parameters ($N = 1 \times 10^3$,$\eta = 70.0\kappa$, $U_0 = -0.004\kappa$) and cooling has been demonstrated for 5×10^3, 1×10^4, 1×10^5 and , 1×10^6 particles.

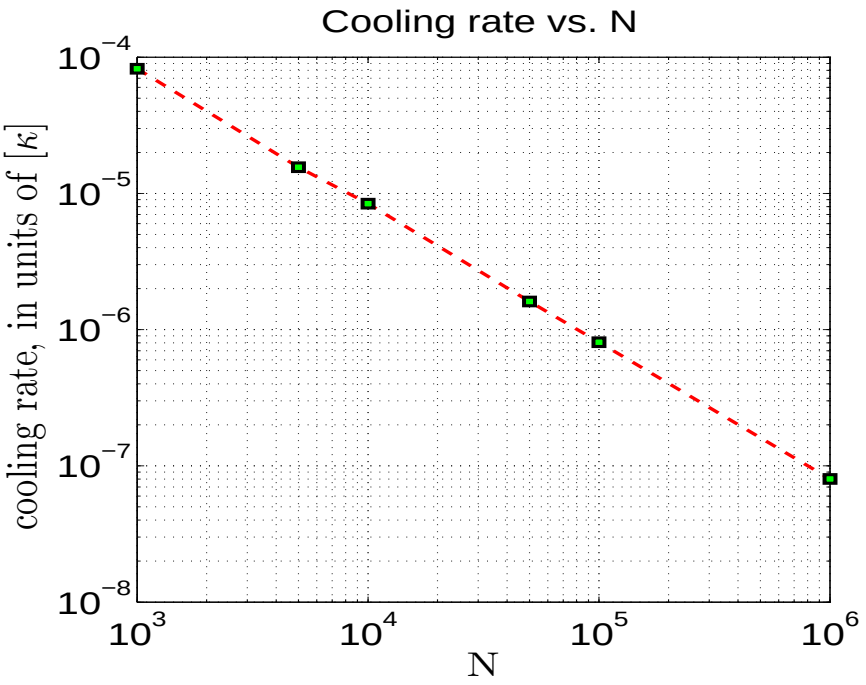

Figure 2.5: Cooling rate (constant cooling parameter) as a function of number of particles (N). The linear decrease of the cooling rate with atom number is clearly visible here.

As shown in fig. 2.5 the cooling time scales linearly with respect to the number of atoms inside the cavity and increases if the number of atoms increases.

Note, the scaled parameters found for $N = 1 \times 10^6$ atoms

η = 2300.0 κ

Δ_a = -125.0 κ

Γ = 3.25 κ

g_0 = 0.02 κ

σ = 28.0 $\hbar k$

correspond to those being used in current cavity cooling experiments at UCL (University College of London), where the above parameters correspond to the real experimental parameters:

cavity linewidth:	κ	= 1.6×10^6	Hz
laser wavelength:	λ	= 852.4 $\times10^{-9}$	m
Cs decay rate:	Γ_{lw}	= 5.23 $\times10^6$	Hz
coupling constant:	g_0	= 35.4 $\times10^3$	Hz
Cs mass:	m	= 2.21 $\times10^{-25}$	kg
Initial temperature:	T_{ini}	= 160.0 $\times10^{-6}$	K
atom-cavity detuning:	Δ_A	= -200 $\times10^6$	Hz
laser power:	P	$\leq$ 0.1	W

2.3 Validity of the Classical Model of Cavity Cooling

In previous studies of cavity cooling [27, 37, 38, 39], which assumed a single atom or a small number of atoms and a cavity mode containing few photons, the atomic momentum spread or temperature is mainly due to fluctuations in the forces acting on the atoms and is limited by the cavity linewidth. In this thesis, we consider cases where the number of atoms is very large (typically $N > 10^5$ in e.g. the UCL experiments) and consequently the cavity fields are relatively intense and contain a large number of photons (i.e. $|\alpha|^2$). In these cases the behaviour of the system will be essentially classical and the temperature/momentum spread of the atomic ensemble will be mainly due to the relatively large height of the optical potential energy associated with the cavity mode amplitude [47, 48]. In what follows this qualitative argument for the validity of the classical model is investigated in more detail and a condition for its validity is derived.

Starting from the expression for the force on an atom in the cavity (eq. 2.21)

$$F = \hbar k U_0 |\alpha|^2 sin(2kx) \tag{2.23}$$

then it is possible to derive a position-dependent potential energy

$$V(x) = -\int F dx = \frac{1}{2}\hbar U_0 |\alpha|^2 cos(2kx) \tag{2.24}$$

The temperature associated with this potential energy can be deduced by considering the fact that the atoms trapped in the potential will have a maximum kinetic energy of

$$\frac{p^2}{2m} = \frac{1}{2}V_{max}(x) = \hbar U_0|\alpha|^2 \tag{2.25}$$

so the variance in atomic momentum will be

$$\langle p^2 \rangle \sim m\hbar U_0|\alpha|^2 \tag{2.26}$$

and the associated classical momentum spread of the ensemble will be

$$\sigma_p = \sqrt{\langle p^2 \rangle} = \sqrt{m\hbar U_0}|\alpha|. \tag{2.27}$$

For comparison the kinetic energy of individual atoms due to stochastic fluctuations in the dipole force has been shown to be [37, 49]

$$\frac{p^2}{2m} \sim \hbar\kappa \tag{2.28}$$

so

$$p^2 \sim 2m\hbar\kappa \tag{2.29}$$

with a corresponding momentum spread

$$\sigma_p \sim \sqrt{2m\hbar\kappa} \tag{2.30}$$

Consequently, the ratio of the spreads can be written as

$$\frac{\sigma_p(int)}{\sigma_p(fluc)} = \frac{\sqrt{m\hbar U_0}|\alpha|}{\sqrt{m\hbar\kappa}} = \sqrt{\frac{1}{2}\frac{U_0}{\kappa}}|\alpha| \tag{2.31}$$

For a cavity pumped close to resonance, the mode amplitude $|\alpha|$ will be

$$|\alpha| \sim \frac{\eta}{\kappa} = \bar{\eta}, \quad \frac{U_0}{\kappa} = \bar{U}_0 \tag{2.32}$$

so in terms of the parameters defined in section 2.1, the ratio of the classical interaction spread and the quantum mechanical "fluctuations" spread is

$$\frac{\sigma_p(int)}{\sigma_p(fluc)} = \sqrt{\frac{1}{2}\bar{U}_0\bar{\eta}} \tag{2.33}$$

Consequently, a classical model which neglects stochastic fluctuations in the optical forces should be a good approximation in the limit where $\sigma_p^{int} \gg \sigma_p^{fluc}$ i.e.

$$\frac{1}{2}\bar{U}_0\bar{\eta}^2 \gg 1 \tag{2.34}$$

which in real dimensional units can be written as

$$\frac{1}{2}\frac{g_0^2}{\Delta_a}\frac{\eta}{\kappa^3} \gg 1 \tag{2.35}$$

which implies strong-atom field coupling and large pump photon numbers as would be expected from a classical limit.

The validity of this classical limit can be demonstrated by a comparison of the classical model (eqs. 2.20 and 2.22) where the momentum diffusion due to fluctuating optical forces is neglected, with the corresponding equations which include momentum diffusion arising as a result of stochastic fluctuations in the optical dipole force i.e.

$$\frac{d\alpha}{dt} = [-\kappa - \gamma_o \sum_j cos^2(kx_j) + i\Delta_c - iU_o \sum_j cos^2(kx_j)\ ]\alpha + \eta \tag{2.36}$$

$$\frac{dp_j}{dt} = -\hbar U_o |\alpha^2| \frac{d}{dx} cos^2(kx_j) + \xi(t) \tag{2.37}$$

$$\frac{dx_j}{dt} = \frac{p_j}{m} \tag{2.38}$$

where $\xi(t)$ is a Gaussian random variable with zero mean and variance D such that $\overline{\xi(t)} = 0$ and $\overline{\xi(t)\xi(t-T)} = 2D\delta(T)$ where the overbar indicates a time average [50, 51]. The effect of the random part of the force in eq. (2.37), $\xi(t)$, is therefore to cause momentum diffusion such that $\overline{p^2} \simeq 2Dt$. The momentum diffusion coefficient, D is defined as [39, 47]

$$D = 2\gamma_0 |\alpha|^2 \left[\hbar \frac{d}{dx} g(x)\right]^2 + \hbar^2 k^2 \bar{u^2} g(x)^2 \tag{2.39}$$

where g(x) is the cavity mode function and $k^2\bar{u^2}$ is the mean value of the recoil momentum projected onto the cavity axis.

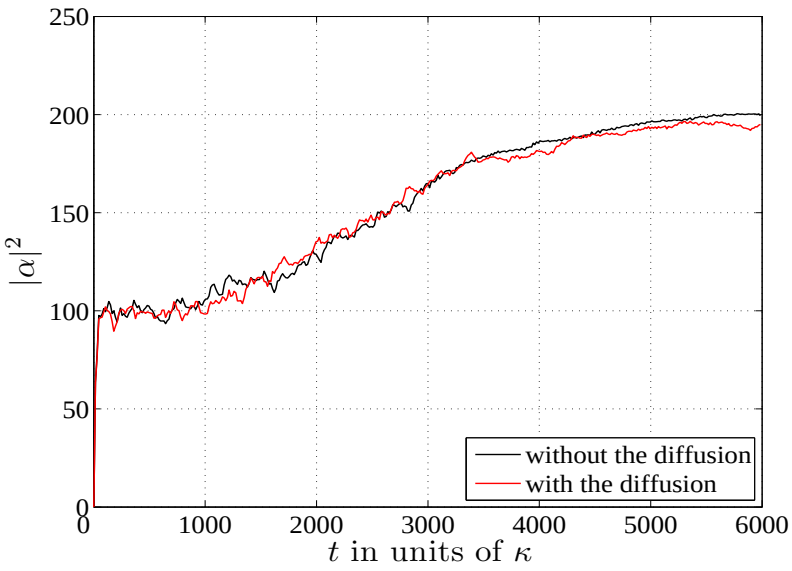

Figure 2.6: Comparison of the time evolution of the field intensity with and without momentum diffusion due to fluctuating optical forces. The parameters used are: $N = 100, \Delta_a = -40\kappa, U_0 = -2.5 \times 10^{-2}\kappa, \gamma_0 = 6.25 \times 10^{-5}\kappa, \eta = 15\kappa$

Figures 2.6 and 2.7 show a comparison of the classical model defined by eqs. (2.20 and 2.22), where momentum diffusion is neglected, and its quantum counterpart eqs. (2.36 and 2.38) where momentum diffusion is included.

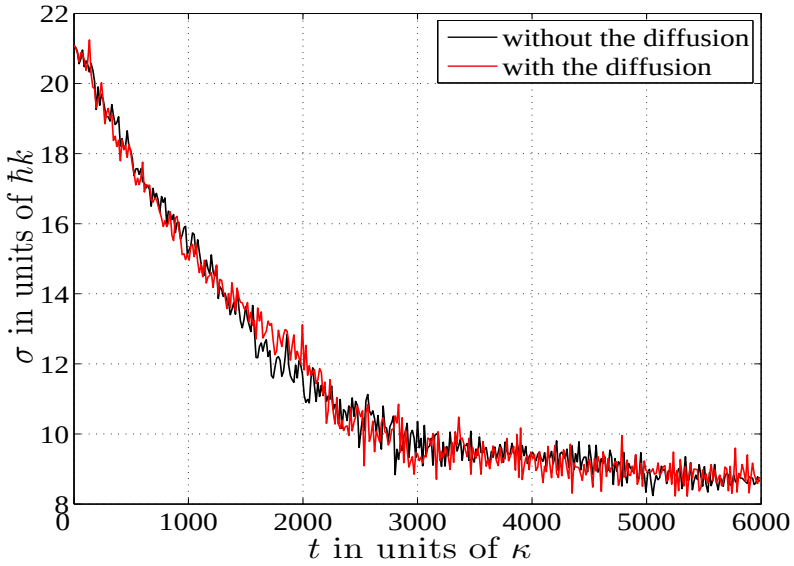

Figure 2.7: Comparison of the time evolution of the particle's momentum spread with and without momentum diffusion due to fluctuating optical forces. The parameters used are: $N = 100, \Delta_a = -40\kappa, U_0 = -2.5 \times 10^{-2}\kappa, \gamma_0 = 6.25 \times 10^{-5}\kappa, \eta = 15\kappa$

The parameters used in figures 2.6 and 2.7 are: $N = 100, \Delta_a = -40\kappa, U_0 = -2.5 \times 10^{-2}\kappa, \gamma_0 = 6.25 \times 10^{-5}\kappa, \eta = 15\kappa$ so the condition derived in eq. (2.34) for the validity of the classical model, i.e. neglects of quantum mechanical momentum diffusion, is satisfied. It can be seen from figures 2.6 and 2.7 that the condition is valid as the behaviour of the momentum spread and the field intensity is not significantly affected by the inclusion of momentum diffusion.

2.4 Vlasov Model of the Many Atom-Cavity System

The particle model is a powerful tool for simulating a limited number of particles. For larger ensembles the requirement of information about the position and momentum of all the atoms at all times makes the numerical simulations more time-consuming. An alternative method to simulate systems involving large numbers of atoms or particles is to use a distribution function $f(\boldsymbol{x}, \boldsymbol{p}, t)$.

In the absence of collisions an ensemble of particles can be described by a distribution function $f(\boldsymbol{x}, \boldsymbol{p}, t)$ in six-dimensional phase space. Liouville's theorem

$$\frac{df}{dt} = 0 \tag{2.40}$$

asserts that the phase-space distribution function is constant along the trajectories of the system - that is, the density of system points in the vicinity of a given system point travelling through phase-space is constant with time. For a large number of particles, moving under the influence of an electromagnetic field, equation (2.40) is called the Vlasov equation [52].

The Vlasov equation describing the evolution of 1-D distribution function $f(x, p, t)$, for a collisionless gas of particles is:

$$\frac{df}{dt} = \frac{\partial f}{\partial t} + \dot{x}\frac{\partial f}{\partial x} + \dot{p}\frac{\partial f}{\partial p} = 0 \tag{2.41}$$

where $\cdot \equiv \frac{\partial}{\partial t}$ and $f(x, p, t)$ is normalised such that:

$$\iint f(x, p, t)\, dx\, dp = 1.$$

For a gas of N atoms, equations (2.20) - (2.22) can be written as

$$\frac{d\alpha}{dt} = \left[-\kappa - \bar{\gamma} + i\Delta_c - i\bar{U}\right]\alpha + \eta \tag{2.42}$$

$$\frac{dp_j}{dt} = \hbar k U_0 \left|\alpha\right|^2 \sin(2kx_j) \tag{2.43}$$

$$\frac{dx_j}{dt} = \frac{p_j}{m} \tag{2.44}$$

where the sum over the N atoms has been replaced with the overbar $\overline{(...)} \equiv \sum_{j=1}^{N}(...)$.

Using equations (2.43) and (2.44) the Vlasov equation, eq. (2.41), can be written as

$$\frac{\partial f}{\partial t} + \frac{p}{m}\frac{\partial f}{\partial x} + \hbar k U_0 |\alpha|^2 \sin(2kx)\frac{\partial f(x,p,t)}{\partial p} = 0 \tag{2.45}$$

and consequently

$$\frac{\partial f}{\partial t} + \frac{p}{m}\frac{\partial f}{\partial x} - i\frac{\hbar k U_0}{2}|\alpha|^2 \left(e^{2ikx} - e^{-2ikx}\right)\frac{\partial f(x,p,t)}{\partial p} = 0. \tag{2.46}$$

The spatial periodicity of the forces on the atoms allows us to assume that the atomic distribution function is also spatially periodic with period $\lambda/2$. Consequently, we can expand f as a Fourier series such that

$$f(x,p,t) = \frac{2}{\lambda}\sum_{n=-\infty}^{\infty} f_n(p,t)e^{2inkz} \qquad \text{where } f_{-n} = f_n^* \tag{2.47}$$

and rewrite the Vlasov equation in eq. (2.46) as

$$\frac{\partial f_n}{\partial t} + 2ink\frac{p}{m}f_n - i\frac{\hbar k U_0}{2}|\alpha|^2 \left(\frac{\partial f_{n-1}}{\partial p} - \frac{\partial f_{n+1}}{\partial p}\right) = 0. \tag{2.48}$$

The wave equation, (2.42), can be written in terms of the Fourier series (eq. (2.47)) using

$$\begin{aligned}\frac{d\alpha}{dt} &= (-\kappa + i\Delta_c)\,\alpha - (\gamma_0 + iU_0)\,\overline{\cos^2(kx)}\alpha + \eta \\ &= (-\kappa + i\Delta_c)\alpha - \frac{(\gamma_0 + iU_0)}{2}\overline{(1+\cos(2kx))}\alpha + \eta \\ &= \left(-\kappa + i\Delta_c - \frac{N}{2}\,(\gamma_0 + iU_0)\right)\alpha - \frac{1}{4}\,(\gamma_0 + iU_0)\,\overline{(e^{2ikx} + e^{-2ikx})}\alpha + \eta\end{aligned}$$

so that replacing

$$\overline{(...)} \equiv N\int_{-\infty}^{\infty}\int_{0}^{\lambda/2} f(x,p,t)(...)\,dx\,dp$$

produces

$$\frac{d\alpha}{dt} = \left(-\kappa + i\Delta_c - \frac{N\gamma_0}{2} - i\frac{NU_0}{2}\right)\alpha - \frac{N}{4}\,(\gamma_0 + iU_0)\int_{-\infty}^{\infty}(f_{-1} + f_1)\;dp\;\alpha + \eta. \tag{2.49}$$

It is useful, for numerical simulations, to define the dimensionless variables $\bar{p} = \frac{p}{\hbar k}$, $\bar{t} = \kappa t$, $\bar{\gamma_0} = \frac{\gamma_0}{\kappa}$, $\bar{U_0} = \frac{U_0}{\kappa}$, $\bar{\omega_r} = \frac{2\hbar k^2}{m\kappa}$, $\bar{\eta} = \frac{\eta}{\kappa}$ and $\bar{f} = \hbar k f$, so that equations (2.48) and (2.49) can be rewritten in the dimensionless form

$$\frac{\partial \bar{f}_n}{\partial \bar{t}} = -in\bar{\omega_r}\bar{p}\bar{f}_n + \frac{i}{2}\bar{U}_0|\alpha|^2\left(\frac{\partial \bar{f}_{n-1}}{\partial \bar{p}} - \frac{\partial \bar{f}_{n+1}}{\partial \bar{p}}\right) \tag{2.50}$$

$$\frac{d\alpha}{d\bar{t}} = \left(-1 + i\bar{\Delta_c} - \frac{N\bar{\gamma}_0}{2} - i\frac{N\bar{U}_0}{2}\right)\alpha - \frac{N(\bar{\gamma}_0 + i\bar{U}_0)}{4}\int_{-\infty}^{\infty}\left(\bar{f}_{-1} + \bar{f}_1\right)\;d\bar{p}\;\alpha + \bar{\eta} \tag{2.51}$$

The Vlasov model equations (2.50) - (2.51) are completely equivalent to the particle

model equations (2.20) - (2.22) derived earlier. In the following section numerical solution of both models will be presented. It will be shown that using the same initial conditions and parameters both models display excellent agreement [53].

2.5 Comparison Between the Particle Model and the Vlasov Model (Cavity-Pump Configuration)

The time evolution of the field intensity and the particles average momentum for the Vlasov and particle model are now investigated for the case of the cavity pump configuration (fig. 2.4).

Figure 2.8 shows the time evolution of the field intensity for the cavity-pump configuration, as calculated from the particle model (eqs. (2.20) - (2.22)) and the Vlasov model (eqs. (2.50) - (2.51)). It can be seen from fig. 2.8 that both models display rapid saturation of the field at ($\kappa t \approx 5$) and small oscillations at longer times.

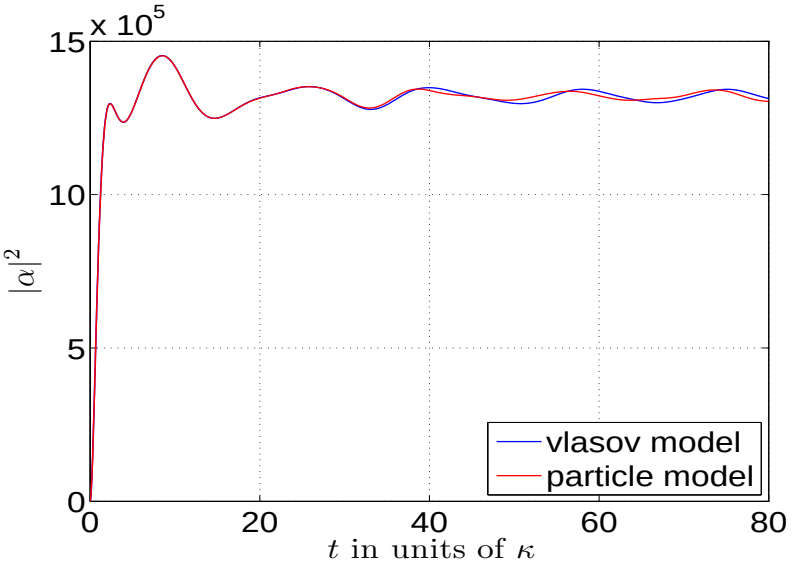

Figure 2.8: Cavity pump configuration: comparison of the field intensity evolution of the Vlasov (blue curve) and the Particle model (red curve). Scaled parameters: $N = 2 \times 10^5$, $\Delta_c = -1.5\kappa$, $\eta = 1500\kappa$, $U_0 = -5.0 \times 10^{-6}\kappa$

In addition to agreement in the evolution of the cavity field both the particle and Vlasov models also give almost identical results for the evolution of averaged quantities of the atomic sample like the average momentum and momentum spread. For demonstration purposes the initial mean velocity of the particles has been chosen to be nonzero, so that $\langle p \rangle = 10\hbar k$ with a spread of $\sigma = 5\hbar k$. The damped oscillations of the average momentum shown in fig. 2.9 are due to the trapping of the atoms in the potential wells formed by the intracavity standing wave field. It is worth mentioning that despite the average velocity decrease, trapped particles initially gain some kinetic energy when falling towards the potential minima, so that the velocity spread initially increases in time (fig. 2.10).

The excellent agreement between the two models and the validity of the Vlasov approach is clearly demonstrated by figs. 2.8 - 2.10.

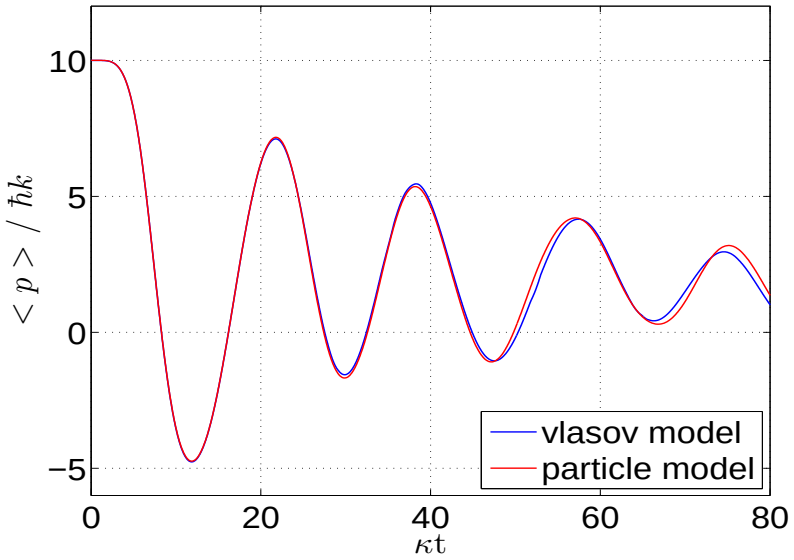

Figure 2.9: Cavity pump configuration: comparison of the mean momentum evolution of the Vlasov (blue curve) and the Particle model (red curve). Scaled parameters: $N = 2 \times 10^5$, $\Delta_c = -1.5\kappa$, $\eta = 1500\kappa$, $U_0 = -5.0 \times 10^{-6}\kappa$, $\langle p_0 \rangle = 10\hbar k$

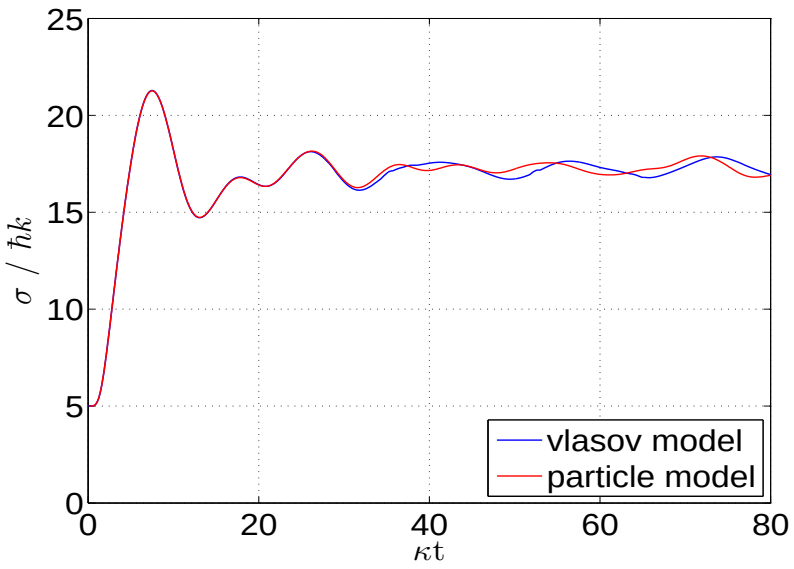

Figure 2.10: Cavity pump configuration: comparison of the momentum spread evolution of the Vlasov (blue curve) and the Particle model (red curve). Scaled parameters: $N = 2 \times 10^5$, $\Delta_c = -1.5\kappa$, $\eta = 1500\kappa$, $U_0 = -5.0 \times 10^{-6}\kappa$, $\langle p_0 \rangle = 10\hbar k$, $\sigma = 5\hbar k$

The good agreement between the two models can be further demonstrated by comparison of phase space evolution in both the particle model and the Vlasov model. A simulation of the phase space evolution for the particle model is presented in figure 2.11. Initially the particles are uniformly distributed over one wavelength of the wave and normally distributed in momentum space with a Gaussian momentum distribution. Depending on a particle's position in the optical potential it can be accelerated or decelerated. Particles which do not have enough kinetic energy to escape the potential are trapped in the single potential well ($\kappa t = 10$, $\kappa t = 15$). The half-wavelength periodicity of the potential field in this configuration is clearly visible.

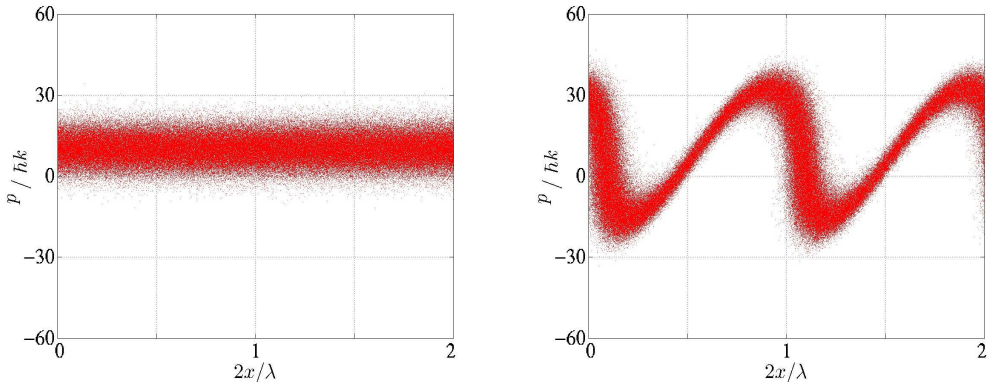

(a) $\kappa t = 0$ (b) $\kappa t = 5$

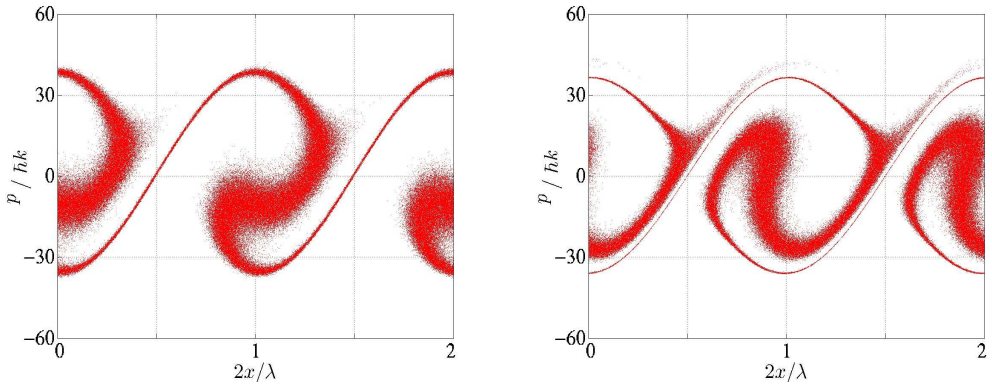

(c) $\kappa t = 10$ (d) $\kappa t = 15$

Figure 2.11: Time evolution of phase space calculated from a numerical simulation of the particle model, eqs. (2.20) - (2.22). Scaled parameters:: $N = 2 \times 10^5$, $\Delta_c = -1.5\kappa$, $\eta = 1500\kappa$, $U_0 = -5.0 \times 10^{-6}\kappa$, $\langle p_0 \rangle = 10\hbar k$, $\sigma = 5\hbar k$

Figure 2.12 shows the time evolution of the momentum distribution function $f(x, p, t)$ for the Vlasov model. It shows that the same behaviour is also demonstrated by the Vlasov model. Here equations (2.50) - (2.51) have been solved numerically with the same parameters as previously used in the particle model (fig. 2.11).

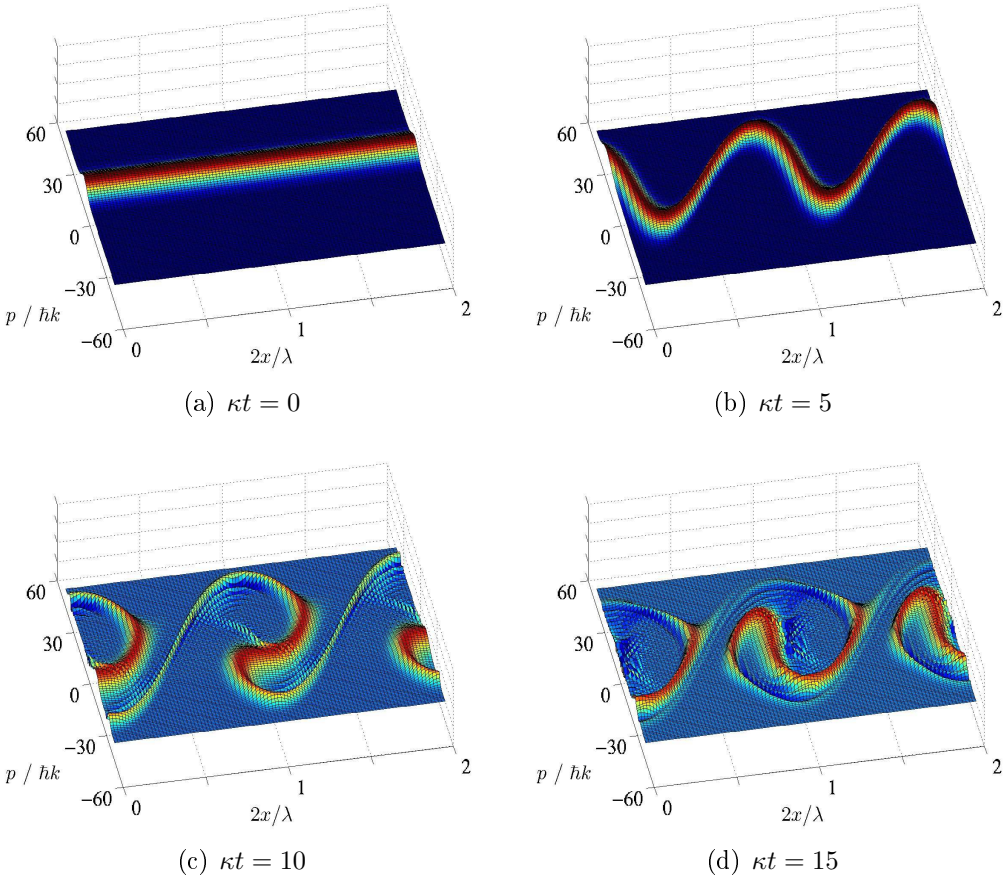

(a) $\kappa t = 0$ (b) $\kappa t = 5$

(c) $\kappa t = 10$ (d) $\kappa t = 15$

Figure 2.12: Time evolution of the momentum distribution function $f(x, p, t)$ from a numerical simulation of the Vlasov model, eqs. (2.50) - (2.51). Parameters used are the same as those in fig. 2.11 i.e $N = 2 \times 10^5$, $\Delta_c = -1.5\kappa$, $\eta = 1500\kappa$, $U_0 = -5.0 \times 10^{-6}\kappa$, $\langle p_0 \rangle = 10\hbar k$, $\sigma = 5\hbar k$

Numerically, the agreement of the Vlasov model with the particle model depends mainly on a sufficient number of Fourier harmonics f_n used to represent the distribution function in the expansion eq. (2.47) and a sufficient number of discrete points used to simulate the momentum distribution. In this case the number of spatial harmonics was chosen to be 30 and the number of momentum points was equal 100.

2.6 Numerical Methods for the Particle Model and the Vlasov Model

The particle model is composed of the (2N + 1) coupled differential equations (2.20) - (2.22) hence the simulation of this model is based on the simultaneous numerical solution of each of the equations. Since this is a typical initial value problem the 4th order Runge-Kutta method, commonly used in similar models, has been applied here. The 4th order Runge-Kutta method makes an excellent compromise between the speed and the accuracy of numerical calculations [54]. In contrast, the Vlasov model is a set of two partial differential equations (2.50) - (2.51). From the variety of numerical methods for solving partial differential equations, the Finite Difference Method was chosen. More specifically the implicit Crank-Nicholson scheme was used due to its simplicity and good accuracy.

The codes for both particle and the Vlasov methods were written using Fortran 90. This general-purpose programming language is especially suited to high-performance numeric computation and scientific computing. In order to further improve the speed and performance of the calculations some of the codes were parallelised with the memory shared multiprocessing method also known as OpenMP. More details of the numerical method for solving the Vlasov model can be found in Appendix A.

Chapter 3

Atom-Pump Configuration

In the previous chapter, the optical cavity was assumed to be pumped directly via one of the cavity mirrors. In this chapter an alternative pumping configuration is considered, where atoms are illuminated by the pump field which propagates transversely into the cavity (fig. 3.1). This results in an atomic-position effective pumping term, which is responsible for the presence of an additional force acting on the atoms. This force, dependent on field intensity, originates from the coherent redistribution of photons between the pump and the field mode and leads to cooperative action and self-organization of the atoms in the cavity [39, 55, 56].

3.1 Classical Derivation of Atom-Pump Configuration

Consider a system consisting of an optical cavity containing atoms illuminated by the field being sent transversely into the cavity (fig. 3.1).

The external field induces a dipole moment in the atom which in turn contributes to the electric field as a driving term in the wave equation

$$-\frac{\partial^2}{\partial x^2}E(x,t)+\frac{1}{c^2}\frac{\partial^2}{\partial t^2}E(x,t)+\mu_o\sigma\frac{\partial}{\partial t}E(x,t)=-\mu_o\frac{\partial^2}{\partial t^2}P(x,t) \tag{3.1}$$

where σ is the conductivity of the cavity mirrors, μ_o is the magnetic permeability

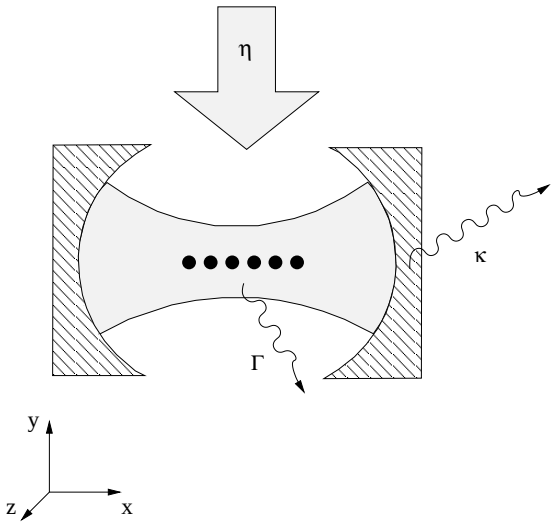

Figure 3.1: Schematic representation of an atom-pumped resonator. The cavity pumping rate, spontaneous loss rate and cavity decay rate are determined by the parameters η, Γ and κ respectively

and c is the speed of light.

The electric fields (pump and cavity) and polarisation are defined as follows

$$E_p(y,t) = \xi_p e^{-i\omega_p t}\ u_p(y) + c.c. \tag{3.2}$$

$$E_c(x,t) = \xi_c e^{-i\omega_c t}\ u_c(x) + c.c. \tag{3.3}$$

$$P(x,t) = \mathcal{P} e^{-i\omega_p t}\ + c.c. \tag{3.4}$$

where $u_c(x)$ is the intracavity mode function $cos(kx)$ with wave number k. Substituting (3.2) - (3.4) into (3.1), finding the derivatives and assuming that ξ and $\mathcal{P}$ are slowly varying amplitudes then eq. (3.1) can be reduced to

$$\dot{\xi}_c + (\kappa - i\Delta_c)\ \xi_c \approx \frac{i\omega_p \mathcal{P}}{2\epsilon_o}. \tag{3.5}$$

where Δ_c is the detuning between the pumping field and cavity frequency ($\Delta_c = \omega_p - \omega_c$).

The polarisation has a contribution from both the cavity and transverse pump fields and can be written as

$$P(x,t) = \alpha_{pol}\left[\xi_c u_c(x) + \xi_p u_p(y)\right] e^{-i\omega t}\ \delta(x - x_a)/A \tag{3.6}$$

where $\delta(x - x_a)$ is a Dirac delta function and A is the cavity cross-section. α_{pol} is an electronic polarisability defined as [57]

$$\alpha_{pol} = \frac{e^2}{(2m\omega_p)(-i\Gamma + (\omega_o^2 - \omega_p^2))/2\omega_p} \tag{3.7}$$

or

$$\alpha_{pol} = \frac{e^2}{(2m\omega_p)(-i\Gamma - \Delta_a)}. \tag{3.8}$$

where we have used the approximation $(\omega_o^2 - \omega_p^2)/2\omega_p = (\omega_o - \omega_p)(\omega_o + \omega_p)/2\omega_p \approx -\Delta_a$. Using (3.4), (3.6) and with $\mathcal{P} = \frac{2}{d}\int_{-d/2}^{d/2} dx P(x,t) cos(kx)$, where d denotes the cavity length, then

$$\mathcal{P} = \frac{\alpha_{pol}}{V}\left[\xi_c u_c(x) + \xi_p u_p(y)\right] cos(kx) \tag{3.9}$$

so

$$\mathcal{P} = i\ \frac{e^2}{(2m\omega_p V)}\frac{cos^2(kx_a)}{(\Gamma - i\Delta_a)}\xi_c + i\ \frac{e^2}{(2m\omega_p V)}\frac{cos(kx)\ u_p(y)}{(\Gamma - i\Delta_a)}\xi_p \tag{3.10}$$

Inserting (3.10) into (3.5) the latter becomes

$$\dot{\xi}_c = -\frac{e^2}{(2mV\epsilon_o)}\frac{cos^2(kx)}{(\Gamma - i\Delta_a)}\xi_c - (\kappa - i\Delta_c)\ \xi_c - \frac{e^2}{(2mV\epsilon_o)}\frac{cos(kx)\ u_p(y)}{(\Gamma - i\Delta_a)}\ \xi_p \tag{3.11}$$

which can be written in terms of the position dependent scattering rate $\gamma(x)$ and frequency shift $U(x)$, defined as

$$\gamma(x) = \frac{\Gamma}{\Gamma^2 + \Delta_a^2} g_o^2 cos^2(kx) = \gamma_o cos^2(kx), \tag{3.12}$$

and

$$U(x) = \frac{\Delta_a}{\Gamma^2 + \Delta_a^2} g_o^2 cos^2(kx) = U_o cos^2(kx) \tag{3.13}$$

respectively, where g_o is the cavity-atom coupling strength, i.e

$$g_o = \sqrt{\frac{e^2}{(2mV\epsilon_o)}} \tag{3.14}$$

Consequently, eq. (3.11) can be written as

$$\dot{\xi}_c = [-\kappa - \gamma(x) + i\Delta_c - iU(x)\ ]\xi_c - \frac{g_o^2 cos(kx)\ u_p(y)}{(\Gamma - i\Delta_a)}\xi_p. \tag{3.15}$$

It is useful to rewrite eq. (3.15) in terms of a dimensionless variable α, whose squared absolute value is associated with the average cavity photon number:

$$|\alpha^2| = \frac{\epsilon_o |\xi^2| V}{\hbar\omega_p} \tag{3.16}$$

so that

$$\xi_c = \sqrt{\frac{\epsilon_o V}{\hbar\omega_p}}\alpha, \quad \xi_p = \sqrt{\frac{\epsilon_o V}{\hbar\omega_p}}\alpha_p \tag{3.17}$$

and finally after substitution

$$\dot{\alpha} = [-\kappa - \gamma(x) + i\Delta_c - iU(x)\ ]\alpha - \eta_{eff} u_p(y) cos(kx) \tag{3.18}$$

In the above we have defined the laser pumping rate $\eta = g_o\alpha_p$ and effective pumping strength $\eta_{eff} = \eta g_o/(\Gamma - i\Delta_a)$.

As was demonstrated in section 2.1 the total force acting on an atom is given by

$$\boldsymbol{F} = \vec{\nabla}(\vec{d}\cdot\vec{E}). \tag{3.19}$$

Assuming that both cavity and pump fields are polarised in the z direction

$$\boldsymbol{E}_c(x,t) = (\xi_c e^{-i\omega_c t}\ u_c(x) + c.c.)\hat{\boldsymbol{z}} \tag{3.20}$$

$$\boldsymbol{E}_p(y,t) = (\xi_p e^{-i\omega_p t}\ u_p(y) + c.c.)\hat{\boldsymbol{z}} \tag{3.21}$$

we have

$$\boldsymbol{F} = \left(\boldsymbol{d}\cdot\frac{\partial \boldsymbol{E}}{\partial x}, \boldsymbol{d}\cdot\frac{\partial \boldsymbol{E}}{\partial y}, \boldsymbol{d}\cdot\frac{\partial \boldsymbol{E}}{\partial z}\right) \tag{3.22}$$

so the force in the "x" direction is

$$F_x = \boldsymbol{d}\cdot\frac{d\boldsymbol{E}}{dx} = \left(\frac{d_x\partial E_x}{\partial x} + \frac{d_y\partial E_y}{\partial x} + \frac{d_z\partial E_z}{\partial x}\right) = \frac{d_z\partial E_z}{\partial x} \tag{3.23}$$

Defining the electron dipole moment

$$d_z = \alpha_{pol} E = \left\{ \alpha_{pol} \left[\xi_c u_c(x) + \xi_p u_p(y) \right] e^{-i\omega_p t} + c.c. \right\} \tag{3.24}$$

and the derivative of the total electric field

$$\frac{\partial E_z}{\partial x} = \xi_c \frac{du_c(x)}{dx} e^{-i\omega_p t} + \xi_c^* \frac{du_c(x)}{dx} e^{i\omega_p t} \tag{3.25}$$

into (3.23) gives

$$F_x = \frac{|\xi_c|^2}{2} \frac{du_c^2(x)}{dx} (\alpha_{pol} + \alpha_{pol}^*) + \left(\alpha_{pol} \xi_p \xi_x^* u_p(y) \frac{du_c(x)}{dx} + c.c. \right) \tag{3.26}$$

where the fast oscillating terms $(e^{-2i\omega_p t}, e^{2i\omega_p t})$ have been dropped.

For clarity each term on the RHS of eq. (3.26) will now be considered individually. The polarizability α_{pol} is defined in eq. (3.8) so it can be rewritten in the form

$$\alpha_{pol} = \frac{e^2(-\Delta_a + i\Gamma)}{(2m\omega_p)(\Delta_a^2 + \Gamma^2)}. \tag{3.27}$$

Writing (3.26) in the form $F_x = F_{x_1} + F_{x_2}$ then substituting α_{pol} into (3.26) gives

$$(\alpha_{pol} + \alpha_{pol}^*) = -\frac{e^2}{m\omega_p} \frac{\Delta_a}{\Delta_a^2 + \Gamma^2} \tag{3.28}$$

so the first term of (3.26) i.e. F_{x_1} is

$$F_{x_1} = -|\xi_c|^2 \left[\frac{e^2}{2m\omega_p} \frac{\Delta_a}{\Delta_a^2 + \Gamma^2} \right] \frac{du_c^2(x)}{dx}. \tag{3.29}$$

Multiplying and dividing (3.29) by V, ϵ_o and $\hbar$ and introducing U_o, g_o^2 and $|\alpha|^2$ (eqs. (3.13) (3.14) and (3.16) respectively) then it is possible to write

$$F_{x_1} = -\hbar U_o |\alpha|^2 \frac{du_c^2(x)}{dx} \tag{3.30}$$

The second term of (3.26) can be written as

$$F_{x_2} = u_p(y) \frac{du_c(x)}{dx} (\alpha_{pol} \xi_c^* \xi_p + c.c.) \tag{3.31}$$

and one can use the dimensionless variable, α, previously defined, so that

$$\alpha = \sqrt{\frac{\epsilon_o V}{\hbar \omega_p}} \xi \qquad \alpha_p = \sqrt{\frac{\epsilon_o V}{\hbar \omega_p}} \xi_p \tag{3.32}$$

$$\xi_c = \sqrt{\frac{\hbar \omega_c}{\epsilon_o V}} \alpha_c \qquad \xi_c^* = \sqrt{\frac{\hbar \omega_c}{\epsilon_o V}} \alpha_c^* \tag{3.33}$$

$$\xi_p = \sqrt{\frac{\hbar \omega_p}{\epsilon_o V}} \alpha_p \qquad \xi_p^* = \sqrt{\frac{\hbar \omega_p}{\epsilon_o V}} \alpha_p^* \tag{3.34}$$

and consequently

$$F_{x_2} = \frac{\hbar \omega_p}{\epsilon_o V} u_p(y) \frac{du_c(x)}{dx} (\alpha_{pol} \alpha^* \alpha_p + c.c.) \tag{3.35}$$

or alternatively

$$F_{x_2} = i\hbar u_p(y) \frac{du_c(x)}{dx} \left(\frac{e^2}{(2m\epsilon_o V)(\Gamma - i\Delta_a)} \alpha_p \alpha^* + c.c. \right). \tag{3.36}$$

Introducing the laser pumping rate, $\eta = g_o\alpha_p$, and effective pumping term $\eta_{eff} = \eta g_o/(\Gamma - i\Delta_a)$ gives the final expression for F_{x_2}:

$$F_{x_2} = -i\hbar u_p(y)\frac{du_c(x)}{dx}\left(\eta^*_{eff}\alpha - \eta_{eff}\alpha^*\right). \tag{3.37}$$

Combining both parts of the total force (3.30) and (3.37) and recalling equation (3.18) we obtain self-consistent set of equations which describe the dynamics of the field amplitude α and the centre of mass motion of N dipoles along the cavity axis x, [39]:

$$\begin{aligned}\dot{\alpha} = i&\left[\Delta_c - U_o\sum_j cos^2(kx_j)\right]\alpha \\ &-\left[\kappa + \gamma_o\sum_j cos^2(kx_j)\right]\alpha - \eta_{eff}\sum_j cos(kx_j)\end{aligned} \tag{3.38}$$

$$\begin{aligned}\dot{p_j} = &-\hbar U_o\left(|\alpha^2|\right)\frac{d}{dx_j}cos^2(kx_j) \\ &- i\hbar\left(\eta^*_{eff}\alpha - \eta_{eff}\alpha^*\right)\frac{d}{dx_j}cos(kx_j)\end{aligned} \tag{3.39}$$

$$\dot{x_j} = \frac{p_j}{m} \tag{3.40}$$

In the following section more detailed features of the atom-pump particle model will be demonstrated. Moreover, analogously to the cavity pump configuration, an alternative Vlasov model of the atom-pump configuration will be derived and numerical simulations from both models will be compared.

3.2 Particle Model of Atom-Pumped Configuration

Using (3.38 - 3.40) derived in section 3.1, it is now possible to investigate the dynamical behaviour of an atom-pumped cavity containing a gas of N atoms. The parameters in (3.38 - 3.40) describe the same physical quantities as in the cavity pump model described in section 2.2, in eqs. (2.20) - (2.22). Note that the main difference between the field evolution equations in each configuration (eq. 2.20 and eq. 3.38) is in the pumping term. For atom-pumping, eq. (3.38) is described by $\eta_{eff} \sum_j cos(kx_j)$ which is a position dependent pumping term proportional to

$$\eta_{eff} = \frac{\eta g_o}{-i\Delta_a + \Gamma}, \tag{3.41}$$

where η is the pumping strength, given by the maximum free-space Rabi frequency.

The force on each atom in the atom-pumped configuration, eq. (3.39) contains a sum of two terms. The first term corresponds to a force arising from an optical dipole potential $\propto cos^2(kx)$, which has potential minima at $kx = n\pi$. The second term in (3.39) originates from coherent redistribution of photons between the pump and the field mode. This second force is proportional to $cos(kx)$ and has opposite signs at $kx = 2n\pi$ and $kx = (2n+1)\pi$. If for instance momentarily there are more atoms in even wells so that $\sum cos(kx) > 0$ and the detuning is such that $\Delta_c - U_o \sum cos^2(kx_j) < 0$, then the cosine potential has wells at $kx = 2n\pi$ that deepen the $cos^2(kx)$ optical lattice and has hills at $kx = (2n+1)\pi$ that reduce attractive wells at $cos^2(kx)$. During the cooling process those two forces compete with each other and self-amplify until all the atoms are in the same even or odd wells. Once the atoms redistribute the constructive interference of the scattered light gives rise to the stationary field intensity and self-organization is further stabilised. In other words the self-organisation of the atoms in the cavity can be understood as a

bunching of the atoms on the scale of the optical wavelength (or potential), giving rise to coherent scattering [39].

Self-organisation in the atom-pump model strongly depends on the number of atoms inside the cavity. It can be seen from fig. 3.2 that for low number of atoms the field does not build up and self-organisation cannot be established. For a sufficient number of atoms generated photons build up the field which can be recognised as a growth of the cavity field intensity.

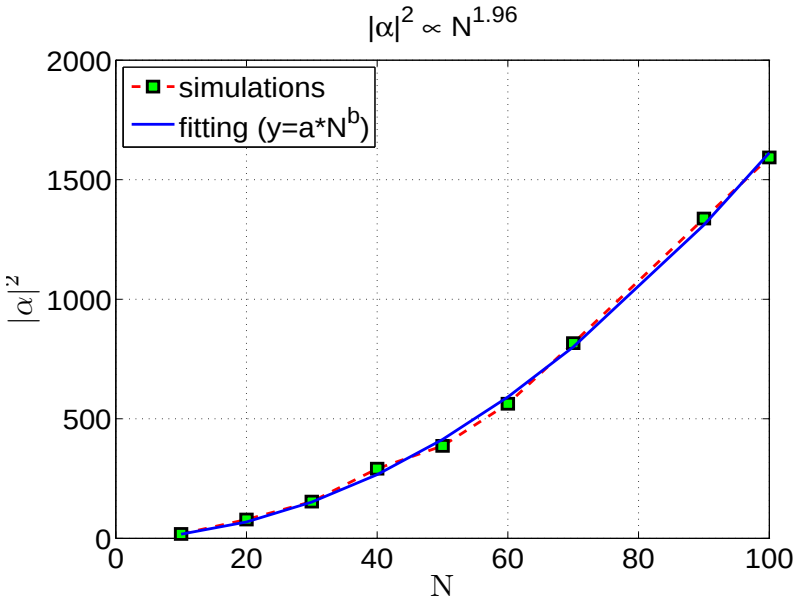

Figure 3.2: Steady-state intensity $|\alpha|^2$ as a function of number of atoms N for the atom-pump configuration. Quadratic dependence of the cavity mode intensity on the atom number demonstrates the cooperative effect. The parameters used are: $U_0 = -1.0 \times 10^{-3}\kappa$, $\gamma_0 = 1.0 \times 10^{-6}\kappa$, $\eta = 500\kappa$.

Strong self-organisation of the atoms can, in fact, lead to faster trapping and cooling of the atomic cloud. Since the number of atoms inside the cavity plays an important role in this process it can be seen that, for given parameters, increasing the number

of atoms (N) can increase the cooling rate.

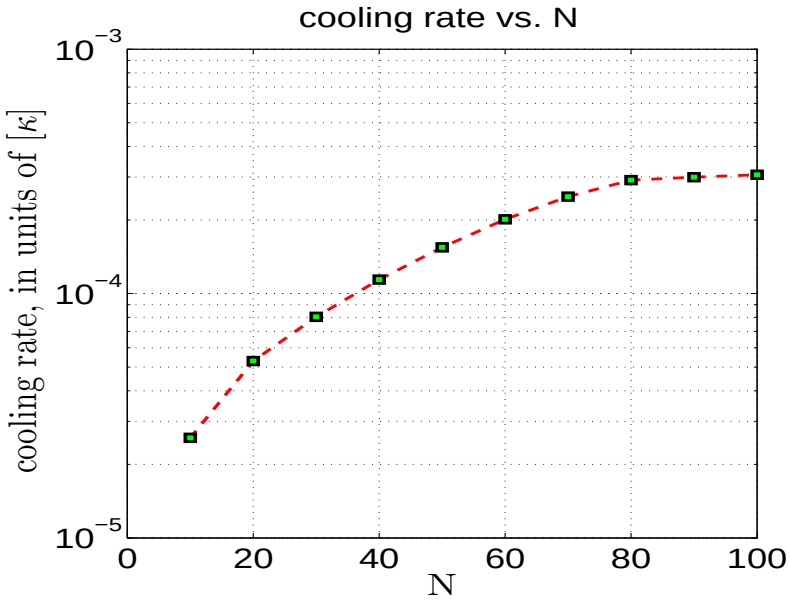

Figure 3.3: Cooling rate vs. number of particles N for the atom-pump configuration. The parameters used are: $U_0 = -1.0 \times 10^{-3}\kappa$, $\gamma_0 = 1.0 \times 10^{-6}\kappa$, $\eta = 500\kappa$.

The cavity cooling rates and their dependence on the number of atoms inside the cavity are presented in fig. 3.3 for the atom-pump configuration. Comparison of fig. 3.3 with the corresponding graph for cavity-pump configuration (fig. 2.5) shows a dramatic difference in the dependence of the cooling rates on N for each configurations.

The self-organisation of the atoms in the atom-pumped cavity configuration will be further demonstrated in the following section where the particle model will be compared with the alternative momentum distribution (Vlasov) model and the time evolution of the phase space will be presented.

3.3 Vlasov Model

It is possible to follow the same procedure as was carried out in the case of the cavity pump configuration (section 2.4) to find the Vlasov model for a gas of atoms in a cavity being pumped off-axis (fig. 3.1). For a gas of N atoms equations (3.38 - 3.40) become

$$\frac{d\alpha}{dt} = \left[-\kappa - \bar{\gamma} + i\Delta_c - i\bar{U}\right]\alpha + \bar{\eta}_{eff} \tag{3.42}$$

$$\frac{dp_j}{dt} = \hbar k U_o |\alpha^2|\ sin(2kx_j) + i\ \hbar k \left(\eta^*_{eff}\alpha - \eta_{eff}\alpha^*\right) sin(kx_j) \tag{3.43}$$

$$\frac{dx_j}{dt} = \frac{p_j}{m} \tag{3.44}$$

where the sum over the N atoms has been replaced with the overbar $\overline{(...)} \equiv \sum_{j=1}^{N}(...)$.

The Vlasov equation for the distribution function $f(x,p,t)$ of the atomic gas is

$$\frac{df}{dt} = \frac{\partial f}{\partial t} + \dot{\boldsymbol{x}}\frac{\partial f}{\partial \boldsymbol{x}} + \dot{\boldsymbol{p}}\frac{\partial f}{\partial \boldsymbol{p}} = 0 \tag{3.45}$$

which with equations (3.43) and (3.44) can be rewritten in the form

$$\frac{\partial f}{\partial t} + \frac{p}{m}\frac{\partial f}{\partial x} + \hbar k U_0 |\alpha|^2 \sin(2kx)\frac{\partial f(x,p,t)}{\partial p} + i\ \hbar k \left(\eta^*_{eff}\alpha - \eta_{eff}\alpha^*\right) \times \\ \times \sin(kx)\frac{\partial f(x,p,t)}{\partial p} = 0 \tag{3.46}$$

so consequently

$$\frac{\partial f}{\partial t} + \frac{p}{m}\frac{\partial f}{\partial x} - i\ \frac{\hbar k U_0}{2}|\alpha|^2\Big(e^{2ikx} - e^{-2ikx}\Big)\frac{\partial f(x,p,t)}{\partial p} + \ \frac{\hbar k}{2}\left(\eta^*_{eff}\alpha - \eta_{eff}\alpha^*\right) \times \\ \times\Big(e^{ikx} - e^{-ikx}\Big)\frac{\partial f(x,p,t)}{\partial p} = 0. \tag{3.47}$$

It can again be assumed that the atomic distribution function $f(x,p,t)$ is spatially periodic in space (on this occasion with period λ), which allows f to be written as a Fourier series such that

$$f = \frac{1}{\lambda}\sum_{n=-\infty}^{\infty} f_n e^{inkz} \quad , \quad \text{where } f_{-n} = f_n^*$$

and Vlasov equation in eq. (3.47) can be expressed as

$$\frac{\partial f_n}{\partial t} + ink\frac{p}{m}f_n - \frac{i}{2}\ \hbar k U_0|\alpha|^2\left(\frac{\partial f_{n-2}}{\partial p} - \frac{\partial f_{n+2}}{\partial p}\right) + \frac{1}{2}\ \hbar k\left(\eta^*_{eff}\alpha - \eta_{eff}\alpha^*\right) \times \\ \times\left(\frac{\partial f_{n-1}}{\partial p} - \frac{\partial f_{n+1}}{\partial p}\right) = 0. \tag{3.48}$$

Similarly, the wave equation, eq.(3.42), can be written as

$$\begin{aligned}\frac{d\alpha}{dt} &= (-\kappa + i\Delta_c)\,\alpha - (\gamma_0 + iU_0)\,\overline{\cos^2(kx)}\alpha - \eta_{eff}\overline{\cos(kx)} \\ &= (-\kappa + i\Delta_c)\alpha - \frac{(\gamma_0 + iU_0)}{2}\overline{(1+\cos(2kx))}\alpha - \eta_{eff}\overline{\cos(kx)} \\ &= \left(-\kappa + i\Delta_c - \frac{1}{2}(\gamma_0 + iU_0)\right)\alpha - \frac{1}{4}(\gamma_0 + iU_0)\,\overline{(e^{2ikx} + e^{-2ikx})}\alpha - \\ &- \frac{1}{2}\eta_{eff}\overline{(e^{ikx} + e^{-ikx})} \end{aligned} \tag{3.49}$$

where the overbar $\overline{(...)} \equiv \sum_{j=1}^{N}(...)$ represents a sum over the atoms. Rewriting this sum in terms of the distribution function f

$$\overline{(...)} \equiv N\int_{-\infty}^{\infty}\int_{0}^{\lambda} f(x,p,t)(...)\,dx\,dp$$

then (3.49) becomes

$$\begin{aligned}\frac{d\alpha}{dt} = \left(-\kappa + i\Delta_c - \frac{N\gamma_0}{2} - i\frac{NU_0}{2}\right)\alpha - \frac{N}{4}(\gamma_0 + iU_0)\int_{-\infty}^{\infty}(f_{-2} + f_2)\;dp\;\alpha - \\ \frac{N}{2}\eta_{eff}\int_{-\infty}^{\infty}(f_{-1} + f_1)\;dp\end{aligned} \tag{3.50}$$

Defining the dimensionless variables $\bar{p} = \frac{p}{\hbar k}$, $\bar{t} = \kappa t$, $\bar{\gamma_0} = \frac{\gamma_0}{\kappa}$, $\bar{U_0} = \frac{U_0}{\kappa}$, $\bar{\omega_r} = \frac{2\hbar k^2}{m\kappa}$, $\bar{\eta} = \frac{\eta}{\kappa}$ and $\bar{f} = \hbar k f$, then eq. (3.48) and (3.50) can be rewritten in the dimensionless form

$$\frac{\partial \bar{f}_n}{\partial \bar{t}} = -\frac{1}{2} in\bar{\omega}_r \bar{p} \bar{f}_n + \frac{i}{2}\bar{U}_0 |\alpha|^2 \left(\frac{\partial \bar{f}_{n-2}}{\partial \bar{p}} - \frac{\partial \bar{f}_{n+2}}{\partial \bar{p}} \right) - \frac{1}{2} \left(\eta^*_{eff}\alpha - \eta_{eff}\alpha^* \right) \times \\ \times \left(\frac{\partial \bar{f}_{n-1}}{\partial \bar{p}} - \frac{\partial \bar{f}_{n+1}}{\partial \bar{p}} \right) \tag{3.51}$$

$$\frac{d\alpha}{d\bar{t}} = \left(-1 + i\bar{\Delta}_c - \frac{N\bar{\gamma}_0}{2} - i\frac{N\bar{U}_0}{2} \right) \alpha - \frac{N(\bar{\gamma}_0 + i\bar{U}_0)}{4} \int_{-\infty}^{\infty} \left(\bar{f}_{-2} + \bar{f}_2 \right) \, d\bar{p} \, \alpha - \\ \frac{N}{2}\bar{\eta}_{eff} \int_{-\infty}^{\infty} \left(\bar{f}_{-1} + \bar{f}_1 \right) d\bar{p} \tag{3.52}$$

The Vlasov equations for the atom-pump configuration eqs. (3.51 - 3.52) are completely equivalent to the particle model equations (3.38 - 3.40) derived in section 3.1 and, as will be shown in the following section, both models are in excellent agreement [53].

3.4 Comparison Between the Particle Model and the Vlasov Model (Atom-Pump Configuration)

In this section, numerical simulations of both the particle model and the Vlasov model are carried out for the case of the atom-pump configuration.

A comparison between evolution of the field intensity from the particle model and the Vlasov model is shown in fig. 3.4. In contrast to the cavity pump configuration, where the field intensity indicated almost instantaneous saturation (fig. 2.8), here both models display a slow saturation time after which the field oscillates. As has been mentioned in section 3.2 this is due to fact that the field builds up due to the scattering of the field from small initial density fluctuations. Initially the growth of the field is slow as the randomly positioned atoms scatter the pump field incoherently. However due to the self-organisation or bunching of the atoms under the action of the fields, the scattering of the pump becomes more coherent and the amplification of the field much more rapid, leading to the exponential amplification shown in fig. 3.4

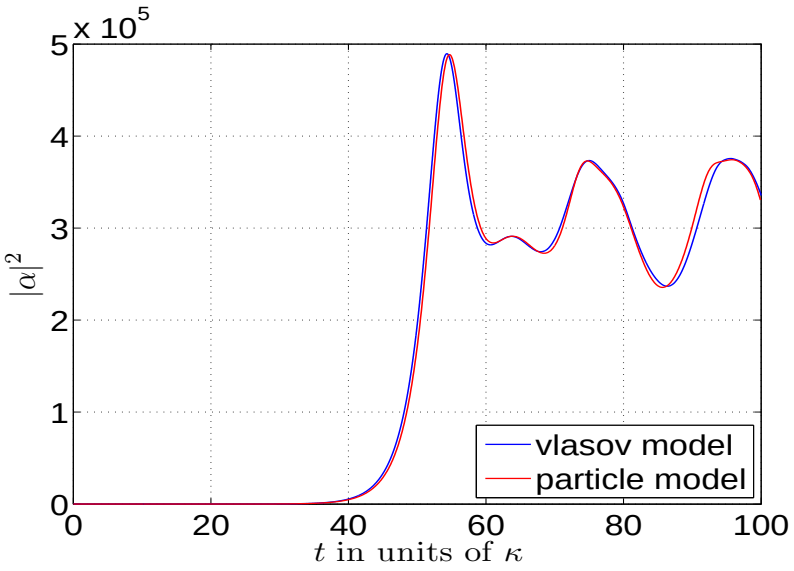

Figure 3.4: Atom-pump configuration: comparison of the field intensity evolution using the Vlasov model (blue curve) and the Particle model (red curve). Scaled parameters: $N = 2 \times 10^5$, $U_0 = -5.0 \times 10^{-6}\kappa$, $\Delta_c = -2.5\kappa$, $\eta = 10\kappa$.

In addition to the excellent agreement that was shown in the field intensity evolution between the particle model and the Vlasov model (fig. 3.4) both models show almost identical results when comparing the average momentum evolution (fig. 3.5) and the momentum spread evolution (fig. 3.6).

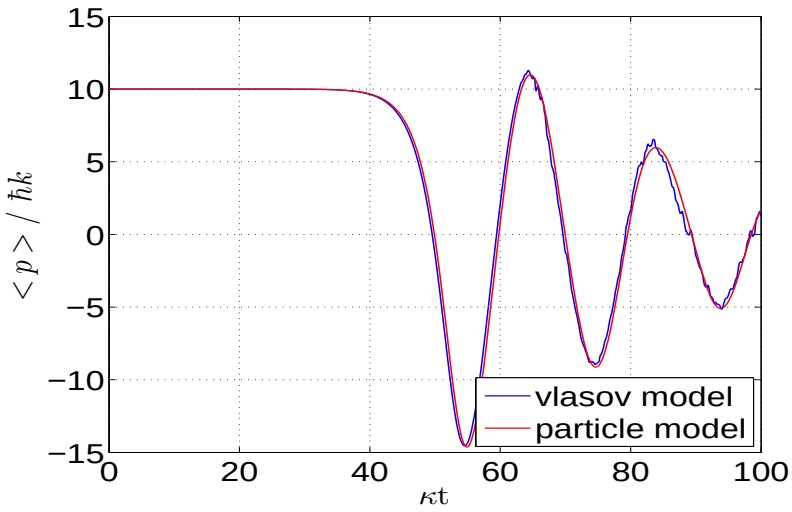

Figure 3.5: Comparison of the mean momentum evolution of 2×10^5 particles using the Vlasov model (blue curve) and the Particle model (red curve) (atom-pump configuration). The other parameters used are: $U_0 = -5.0 \times 10^{-6}\kappa$, $\Delta_c = -2.5\kappa$, $\eta = 10\kappa$.

Despite the fact that the atoms are trapped in the potential wells which can be seen as an oscillation of the average momentum shown in figure 3.5 the particles under the influence of the strong field still oscillate quickly in the potentials and hence the growth of the momentum spread can be observed (fig. 3.6).

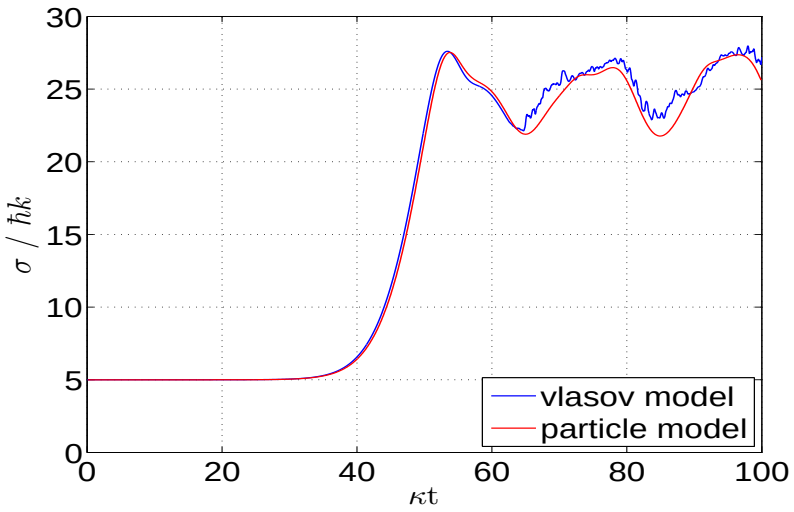

Figure 3.6: Comparison of the momentum spread evolution using the Vlasov (blue curve) and the Particle model (red curve). Scaled parameters: 2×10^5 particles, $U_0 = -5.0 \times 10^{-6}\kappa$, $\Delta_c = -2.5\kappa$, $\eta = 10\kappa$.

The process of self-organisation of atoms inside the cavity is clearly visible in figure 3.7, showing the phase space evolution as calculated using the particle model (3.38 - 3.40). Initially the particles are uniformly distributed over one wavelength of the wave and normally distributed in momentum space (t=0). Finally, however, more particles are localised in the even than odd wells which confirms the different structure of the potential field in this configuration (t=60) (compare the phase space evolution for the case of cavity pump configuration shown in fig. 2.11). As mentioned in section 3.2 this is due to the fact that there are two different potentials in the atom-pump configuration. The potentials compete with each other and self-amplify until all the atoms are in the same even or odd wells.

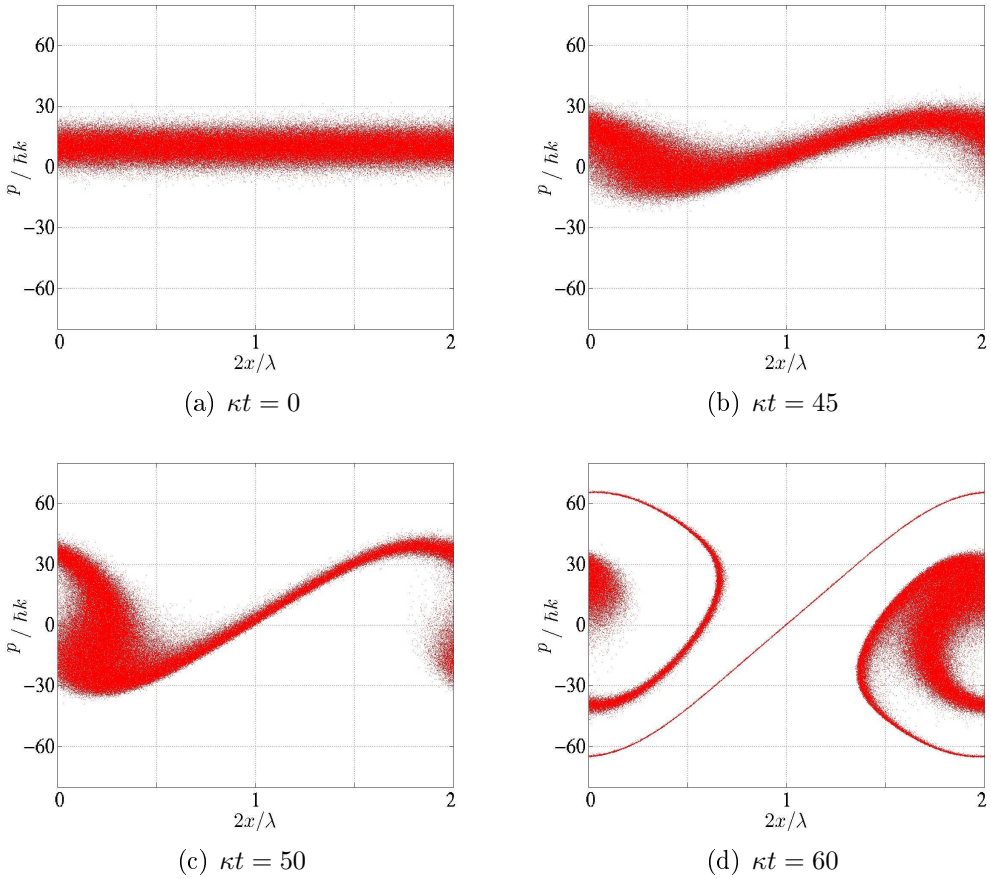

(a) $\kappa t = 0$ (b) $\kappa t = 45$

(c) $\kappa t = 50$ (d) $\kappa t = 60$

Figure 3.7: Time evolution of phase space density (atom-pumping) from a numerical simulation of the particle model eq. (3.38) - (3.40). Scaled parameters: $N = 2 \times 10^5$, $U_0 = -5.0 \times 10^{-6}\kappa$, $\Delta_c = -2.5\kappa$, $\eta = 10\kappa$.

The Vlasov model of the atom-pump configuration (eqs. (3.51) and (3.52)) was solved numerically with the same initial conditions as used for the model – particles need to be uniformly distributed over one wavelength of the wave and normally distributed in momentum space. The results from the Vlasov model are presented in figure 3.8. The distribution function evolves from the initial conditions, at $\kappa t = 0$ to the final state at $\kappa t = 60$. The periodicity of the potential field is already visible at $\kappa t = 50$ and becomes sharper for longer times. This result again agrees well with the results obtained from the particle model simulations (see fig. 3.7 for comparison)

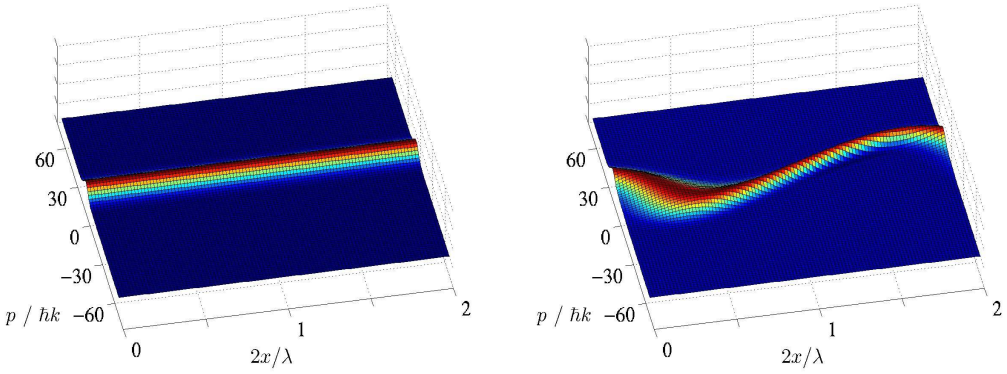

(a) $\kappa t = 0$ (b) $\kappa t = 45$

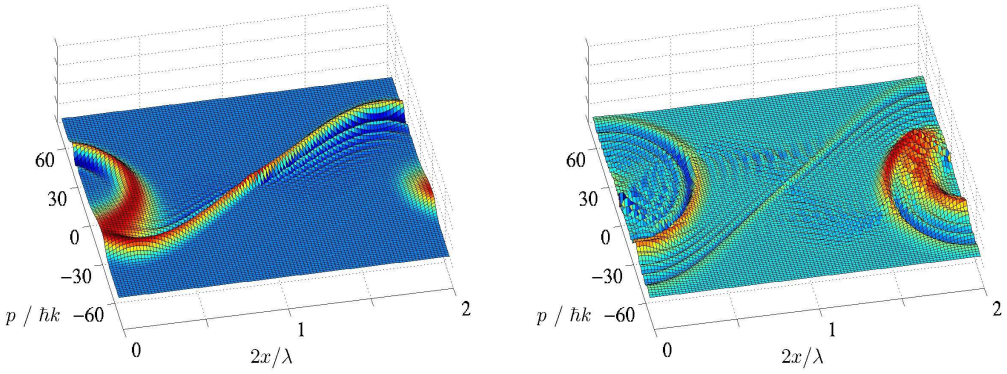

(c) $\kappa t = 50$ (d) $\kappa t = 60$

Figure 3.8: Time evolution of the momentum distribution function $f(x, p, t)$ (atom-pumping) from a numerical simulation of the Vlasov model eq. (3.51) - (3.52). Scaled parameters: $N = 2 \times 10^5$, $U_0 = -5.0 \times 10^{-6}\kappa$, $\Delta_c = -2.5\kappa$, $\eta = 10.0\kappa$.

From the numerical point of view, the Vlasov equations for the atom-pump configuration eqs. (3.51 - 3.52) are more complex that the Vlasov equations derived for cavity pump configuration eqs. (2.50 - 2.51), however the same numerical method – Finite Difference Method (see Appendix A), as was used to solve eqs. (2.50 - 2.51), was used in the case of the atom-pump configuration.

Chapter 4

Semi-Classical Model of Two-Level Atoms in a Cavity

In previous chapters it has been assumed that the atoms behave as classical polarisable particles and the internal dynamics of the atoms are essentially neglected. In order to include the effects associated with the internal atomic dynamics it is possible to use a system of Maxwell-Bloch equations extended to include the atomic of centre mass motion. This is the so-called semi-classical model as it treats the internal atomic degrees of freedom (dipole moment, population difference) quantum mechanically and the electromagnetic field along with external degrees of freedom (atomic position and momentum) classically. The semi-classical model is complementary to the classical model and in the limit of negligible atomic excitation must simplify to show the same behaviour as in the classical model. The cavity and atom-pump configuration derived in previous chapters were assumed to be valid for the case of low atomic excitation. In such a limit where the atom-pump frequency detuning is large the semi-classical model must reduce to classical one.

4.1 Semi-Classical Derivation of Cavity-Pump Configuration

The model consists of an ensemble of two-level atoms confined inside a simple Fabry-Perot cavity illuminated by the pump field directed along the cavity axis, as shown

schematically in fig. 4.1. In the following sections the evolution equations for the internal atomic degrees of freedom (dipole moment and the population difference), external degrees of freedom (position and momentum) and cavity field are derived.

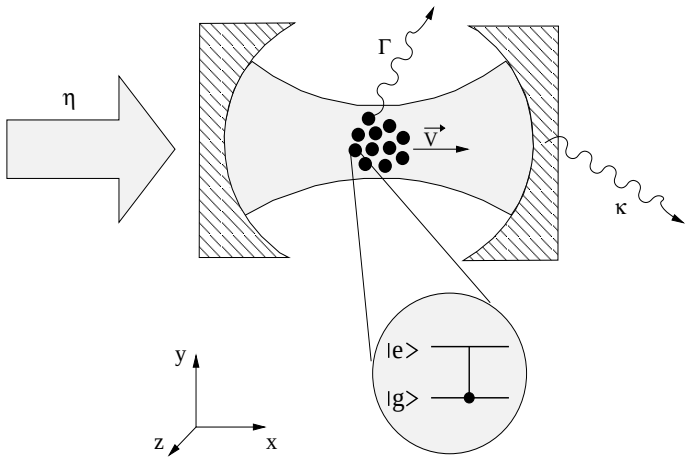

Figure 4.1: An ensemble of two-level atoms in a cavity pumped along its axis via one of the cavity mirrors (cavity-pump configuration). $|g\rangle$ represents a ground state of an atom while $|e\rangle$ represents an excited state of an atom. The cavity pumping rate, spontaneous loss rate and cavity decay rate are determined by the parameters η, Γ and κ respectively.

4.1.1 Internal Degrees of Freedom

The atoms in the ensemble are assumed to have two internal energy states. The lower and upper energy states are labelled $|g\rangle$ and $|e\rangle$ respectively. The Bloch equations for the density matrix elements associated with each atom $\rho_{jk}, j, k = e, g$ are:

$$\frac{\partial \rho_{eg}}{\partial t} = -\left(\Gamma_{eg} + i\omega_{eg}\right)\rho_{eg} + \frac{iE\mu}{\hbar}\left(\rho_{gg} - \rho_{ee}\right) \tag{4.1}$$

$$\frac{\partial}{\partial t}\left(\rho_{gg} - \rho_{ee}\right) = -\Gamma_{ee}\left(\rho_{gg} - \rho_{ee}\right) + \frac{2iE\mu}{\hbar}\left(\rho_{eg} - \rho_{eg}^{*}\right), \tag{4.2}$$

where Γ_{ee} and Γ_{eg} are the longitudinal and transverse atomic decay rates, respec-

tively and the dipole moment is:

$$\boldsymbol{d}_j = \mu \left(\rho_{ge} + \rho_{ge}^*\right) \hat{\boldsymbol{e}} \tag{4.3}$$

where μ is the dipole matrix element and ρ_{eg} is the density matrix element defined as

$$\rho_{eg} = S(x)e^{-i\omega t}, \quad (\rho_{ge} = \rho_{eg}^*) \tag{4.4}$$

and S is the coherence of the atom.

The population difference is here defined as

$$D = \frac{\rho_{gg} - \rho_{ee}}{2}. \tag{4.5}$$

The field in the cavity can be written in the form:

$$E = \left(A(x)e^{-i\omega t} + c.c.\right) g(x) \tag{4.6}$$

where g(x) is a cavity mode function and it has been assumed $\boldsymbol{E} = E\hat{\boldsymbol{e}}$, $\boldsymbol{\mu}_{ge} = \boldsymbol{\mu}_{eg} = \mu\hat{\boldsymbol{e}}$,

Inserting (4.4) and (4.6) into (4.1) produces

$$\left(\frac{dS}{dt} - i\omega S\right) e^{-i\omega t} = -\left(\Gamma_{eg} + i\omega_{eg}\right) S e^{-i\omega t} + \frac{i\mu}{\hbar}\left(\rho_{gg} - \rho_{ee}\right)\left(Ae^{-i\omega t} + c.c.\right) g(x) \tag{4.7}$$

Multiplying (4.7) by $e^{i\omega t}$ and using the definition of eq. (4.5) eq. (4.7) becomes

$$\frac{dS}{dt} = -\Gamma_{eg} S + i\left(\omega - \omega_{eg}\right) S + \frac{2i\mu D}{\hbar} A g(x) \tag{4.8}$$

where terms varying as $e^{2i\omega t}$ have been neglected.

Similarly, substituting for (4.4), (4.5) and (4.6) in (4.2) gives

$$\frac{dD}{dt} = -\Gamma_{ee}\left(D - D^{eq}\right) - \frac{i\mu}{\hbar}\left(AS^* - A^* S\right) g(x) \tag{4.9}$$

where $D^{eq} = 0.5$ in the absence of any external excitation of the atom and we have again fast oscillating terms have been neglected.

Equations (4.8) and (4.9) describe the internal degrees of freedom of each atom under the influence of the cavity field.

4.1.2 Atomic Centre-of-Mass Dynamics

The external degrees of freedom of atoms - the position and momentum - will be described classically.

As shown in chapter 2, the dipole force in the x direction acting on the jth atom is given by:

$$F_x = \boldsymbol{d} \cdot \frac{\partial \boldsymbol{E}}{dx} \tag{4.10}$$

which using (4.3) and (4.6) becomes

$$
\begin{aligned}
F_x &= \mu \left(Ae^{-i\omega t} + c.c.\right)\left(Se^{-i\omega t} + c.c.\right)\frac{dg(x)}{dx} \\
&= \left(SA^* + S^*A\right)\frac{dg(x)}{dx}
\end{aligned} \tag{4.11}
$$

4.1.3 Electromagnetic Field Dynamics

Maxwell's wave equation is

$$
\left(\nabla^2 - \frac{1}{c^2}\frac{\partial^2}{\partial t^2}\right)\boldsymbol{E} = \frac{1}{\epsilon_0 c^2}\frac{\partial^2 \boldsymbol{P}}{\partial t^2} \tag{4.12}
$$

where the polarisation, $\boldsymbol{P}$, is defined as

$$
\begin{aligned}
\boldsymbol{P} &= \sum_j \boldsymbol{d}_j\ \delta\left(\boldsymbol{r} - \boldsymbol{r}_j\right) \\
&= \mu\hat{\boldsymbol{e}}\sum_j \left(Se^{-i\omega t} + c.c.\right)\delta\left(\boldsymbol{r} - \boldsymbol{r}_j\right)
\end{aligned} \tag{4.13}
$$

After finding the derivatives for an ensemble of point-like atoms eq. (4.12) can be rewritten as

$$
\left[-k^2 A + \frac{2\omega}{c^2}\left(i\frac{dA}{dt} + \frac{\omega A}{2}\right)\right] g(x)e^{-i\omega t} + c.c. = -\mu_0\omega^2\mu\sum_j \left(Se^{-i\omega t} + c.c.\right)\delta\left(\boldsymbol{r} - \boldsymbol{r}_j\right) \tag{4.14}
$$

$$
\left[-k^2 A + \frac{2\omega}{c^2}\left(i\frac{dA}{dt} + \frac{\omega A}{2}\right)\right] g(x) = -\mu_0\omega^2\mu\sum_j S\delta\left(\boldsymbol{r} - \boldsymbol{r}_j\right) \tag{4.15}
$$

where the slowly-varying envelope approximation (SVEA) has been used (i.e. $|\frac{\partial}{\partial t}| \ll \omega$, $|\frac{\partial}{\partial z}| \ll k$).

As $\frac{\omega^2}{c^2} = k^2$ and $\frac{1}{\sqrt{\mu_0\ \epsilon_0}} = c^2$, then eq. (4.15) becomes

$$\frac{dA}{dt} g(x) = \frac{i\omega\mu}{2\epsilon_0} \sum_j S\delta\left(\boldsymbol{r} - \boldsymbol{r}_j\right) \tag{4.16}$$

so multiplying both sides of (4.16) by $g(x)$ and integrating over the cross-section area of the cavity $\mathcal{A}$, ($V = \mathcal{A}L$) produces

$$\mathcal{A}\frac{dA}{dt} \int_0^L g(x)^2 dx = \frac{i\omega\mu}{2\epsilon_0} \int_0^L g(x) dx \sum_j S\delta\left(\boldsymbol{r} - \boldsymbol{r}_j\right) \tag{4.17}$$

Then, if the cavity mode function is of the form

$$g(x) = cos(kx), \ \ or \ \ g(x) = sin(kx) \tag{4.18}$$

eq. (4.17) can be expressed as

$$\begin{aligned} \frac{\mathcal{A}\lambda}{4}\frac{dA}{dt} &= \frac{i\omega\mu}{2\epsilon_0} \sum_j S g(x) \\ \Rightarrow \frac{dA}{dt} &= \frac{2i\omega\mu}{\mathcal{A}\lambda\epsilon_0} \sum_j S_j cos(kx_j) \\ \Rightarrow \frac{dA}{dt} &= \frac{i\omega\mu}{V\epsilon_0} \sum_j S_j cos(kx_j) \end{aligned} \tag{4.19}$$

Equations (4.8), (4.9), (4.11) and (4.19) together make a closed set of evolution equations which completely describe the self-consistent interaction of an ensemble of two-level atoms with the cavity mode inside a Fabry-Perot cavity:

$$\frac{dS_j}{dt} = -\Gamma_{eg} + i\left(\omega - \omega_{eg}\right) S_j + \frac{2i\mu D}{\hbar} A g(x) \tag{4.20}$$

$$\frac{dD_j}{dt} = -\Gamma_{ee}\left(D_j - D^{eq}\right) - \frac{i\mu}{\hbar}\left(AS^* - A^*S\right) g(x) \tag{4.21}$$

$$\frac{dp_j}{dt} = \left(SA^* + S^*A\right) \frac{dg(x)}{dx} \tag{4.22}$$

$$\frac{dA}{dt} = \frac{i\omega\mu}{V\epsilon_0} \sum_j S_j cos(kx_j) \tag{4.23}$$

As in previous chapters, it is convenient to introduce the dimensionless parameter α whose absolute squared value $|\alpha|^2$ is associated with the average photon number

$$|\alpha^2| = \frac{\epsilon_o |A|^2 V}{\hbar\omega} \tag{4.24}$$

This implies

$$\alpha = \sqrt{\frac{\epsilon_o V}{\hbar\omega_p}} A, \quad A = \sqrt{\frac{\hbar\omega_p}{\epsilon_o V}} \alpha \tag{4.25}$$

and equations (4.20)-(4.23) become

$$\frac{dS_j}{dt} = -\Gamma_{eg} S + i\Delta_a S + 2ig_0 D\alpha \ cos(kx_j) \tag{4.26}$$

$$\frac{dD_j}{dt} = -\Gamma_{ee}\left(D_j - D^{eq}\right) - ig_0\left(\alpha S^* - \alpha^* S\right) \ cos(kx_j) \tag{4.27}$$

$$\frac{dp_j}{dt} = -\hbar k g_0 \left(S\alpha^* + S^*\alpha\right) sin(kx_j) \tag{4.28}$$

$$\frac{d\alpha}{dt} = ig_0 \sum_j S_j \ cos(kx_j) \tag{4.29}$$

where $g_0 = \mu\sqrt{\frac{\omega}{\hbar\epsilon_0 V}}$ is the atom-cavity coupling constant and V is the cavity mode

volume.

4.1.4 Comparison with the Classical Model

In order to compare the classical and the semi-classical models it is necessary to ensure that the parameters used correspond to a regime in which both models are valid. As stated before the validity of the classical model that has been presented earlier implies negligible excitation of the atomic ensemble and within that limit only can a proper comparison wit the semi-classical model be carried out.

If it is assumed that all atoms remain in the ground state, which implies the condition $\Delta_a^2 \gg 4g_0^2|\alpha|^2$ which can be obtained from the steady states of eqs. (4.26 and 4.27), it is possible to set $D_j = 1/2$ (if assumed that all atoms are in the excited state then obviously $D_j = -1/2$). After performing this procedure eq. (4.26) produces

$$0 = -\Gamma_{eg} S_j + i\Delta_a S_j + 2ig_0 D\alpha \; cos(kx_j)$$

so

$$S_j = \frac{ig_0\alpha}{\Gamma_{eg} - i\Delta_a} \; cos(kx_j) \tag{4.30}$$

Substituting the steady state value of the coherence eq. (4.30) into the force equation (4.28) gives

$$
\begin{aligned}
F_x &= -\hbar k g_0 \left(S\alpha^* + S^*\alpha\right) sin(kx_j) \\
&= -\hbar k g_0^2 cos(kx_j)|\alpha|^2 \left[\frac{-i(\Gamma_{eg} - i\Delta_a)}{\Gamma_{eg}^2 + \Delta_a^2} + \frac{i(\Gamma_{eg} + i\Delta_a)}{\Gamma_{eg}^2 + \Delta_a^2}\right] sin(kx_j) \\
&= -2\hbar k g_0^2 cos(kx_j)|\alpha|^2 \left[\frac{\Delta_a}{\Gamma_{eg}^2 + \Delta_a^2}\right] sin(kx_j) \\
&= \hbar \frac{g_0^2 \Delta_a}{\Gamma_{eg}^2 + \Delta_a^2} |\alpha|^2 sin(2kx_j)
\end{aligned} \tag{4.31}
$$

where we have used the trigonometric identity $2sin(kx)cos(kx) = sin(2kx)$.

Recalling that the frequency shift and the position dependent scattering rate are defined as

$$
\gamma(x) = \frac{\Gamma}{\Gamma^2 + \Delta_a^2} g_o^2 cos^2(kx) = \gamma_o cos^2(kx) \ , \tag{4.32}
$$

$$
U(x) = \frac{\Delta_a}{\Gamma^2 + \Delta_a^2} g_o^2 cos^2(kx) = U_o cos^2(kx) \ . \tag{4.33}
$$

gives finally

$$
F_x = -\hbar |\alpha|^2 \frac{d}{dx} U(x) \tag{4.34}
$$

which is the same equation for the force produced by the cavity field as derived in section 2.1 from a classical model, see eq. (2.16).

Similarly substituting (4.30) into the field equation (4.29) we find

$$\begin{aligned}\frac{d\alpha}{dt} &= ig_0 \sum_j cos(kx_j) \frac{ig_0\alpha}{\Gamma_{eg} - i\Delta_a}\ cos(kx_j) \\ &= -g_0^2 \frac{(\Gamma_{eg} + i\Delta_a)}{\Gamma_{eg}^2 + \Delta_a^2} \alpha \sum_j cos^2(kx_j)\end{aligned} \tag{4.35}$$

Again using (4.32) and (4.33) gives

$$\frac{d\alpha}{dt} = -\left(\gamma_0 + iU_0\right) \alpha \sum_j cos^2(kx_j) \tag{4.36}$$

which is the equation as derived in section 2.1, see eq. (2.15) without the cavity decay and the external field pump rate. Nevertheless, as expected, the semi-classical model within the limit of low excitation population simplifies to the classical model.

The missing cavity decay rate and the pump term still need to be added to the RHS of (4.29) in order to be completely equivalent to the classical model equations. With an external field, equation (4.29) has an additional term

$$\frac{d\alpha}{dt} = ig_0 \sum_j S_j\ cos(kx_j) + \eta e^{-i\Delta_c t} \tag{4.37}$$

where $\eta = \kappa\ \alpha_{ext}$ is the pumping term and Δ_c is the pump-cavity frequency detuning. Defining new field and coherence variables $\alpha = \alpha' e^{-i\Delta_c t}$ and $S = S' e^{-i\Delta_c t}$, then equations (4.26)-(4.29) become

$$\frac{dS'_j}{dt} = -\Gamma_{eg} S' + i\Delta'_a S' + 2ig_0 D\alpha' \; cos(kx_j) \tag{4.38}$$

$$\frac{dD_j}{dt} = -\Gamma_{ee} \left(D_j - D^{eq}\right) - ig_0 \left(\alpha' S'^* - \alpha'^* S'\right) \; cos(kx_j) \tag{4.39}$$

$$\frac{dp_j}{dt} = -\hbar k g_0 \left(S'\alpha'^* + S'^*\alpha'\right) sin(kx_j) \tag{4.40}$$

$$\frac{d\alpha'}{dt} = ig_0 \sum_j S'_j \; cos(kx_j) - \left(\kappa - i\Delta_c\right)\alpha' + \eta \tag{4.41}$$

where $\Delta'_a = \omega_p - \omega_{eg}$ and the extra cavity decay term $-\kappa\alpha'$, has been added to the right side of (4.29).

4.2 Comparison Between the Classical and the Semi-Classical Models (Numerical Simulations)

Equations (4.38) - (4.41) have been solved numerically and the results were compared with the results obtained for the same parameters with the classical model of the cavity pump configuration (2.20) - (2.22).

Fig. 4.2 contains a series of simulations showing the cooling rates for a fixed number of atoms ($N = 1000$) and pumping strength $\eta = 70.0\kappa$ but varying Δ_a and g_0 so that $U_0 = const. = -4.0 \times 10^{-3}\kappa$. It shows that increasing the detuning improves the agreement between the semi-classical and the classical model.

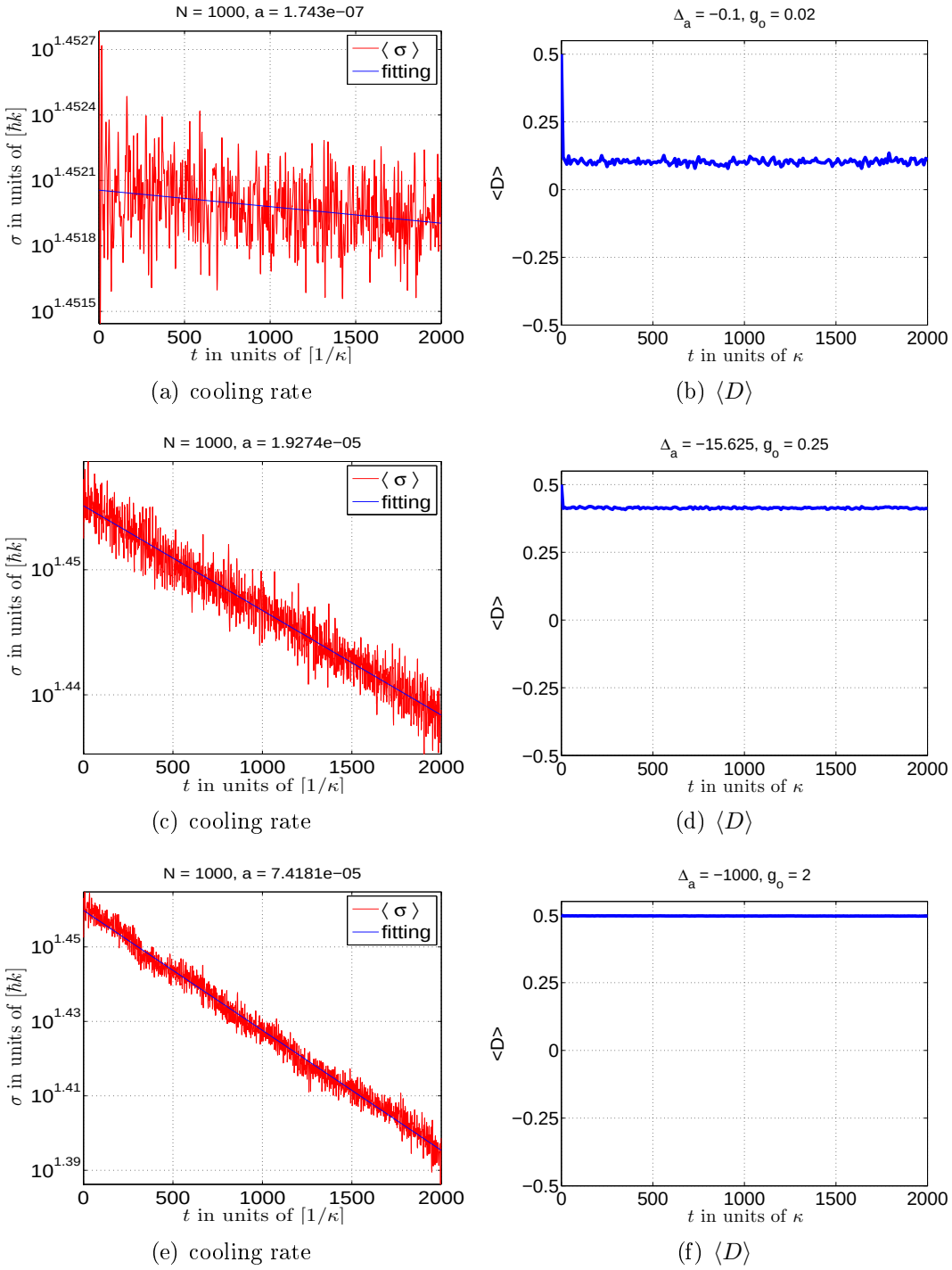

(a) cooling rate (b) $\langle D \rangle$

(c) cooling rate (d) $\langle D \rangle$

(e) cooling rate (f) $\langle D \rangle$

Figure 4.2: Evolution of atomic momentum spread and average population difference ($\langle D \rangle$) calculated using the semi-classical model for different Δ_a and g_0 for $N = 1000$ particles ($U_0 = const.$)

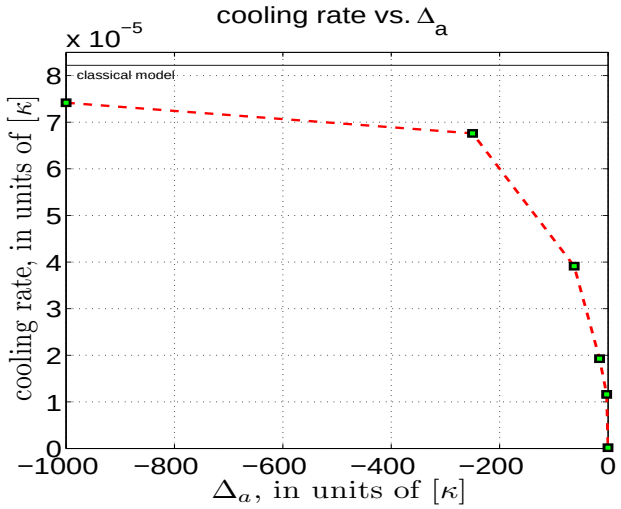

Figure 4.3: Cooling rates calculated using the semiclassical-model for different Δ_a and g_0 ($U_0 = const.$) (Data collected from the gradient of the momentum spread evolution graphs shown in fig. 4.2). The black horizontal line marks the cooling rate found from the classical model for $U_0 = -0.004\kappa$

This is seen more clearly in fig. 4.3 which shows the cooling rate as a function of the pump-atom detuning. The black line represents the result obtained from classical model and it is clear now that the results from the semi-classical model agrees well with the classical model for far detuned fields as predicted in the previous chapter.

For demonstration purposes the evolution of the field intensity (fig. 4.4), momentum (fig. 4.5) and momentum spread (fig. 4.6) using both semi-classical and classical models has been also shown.

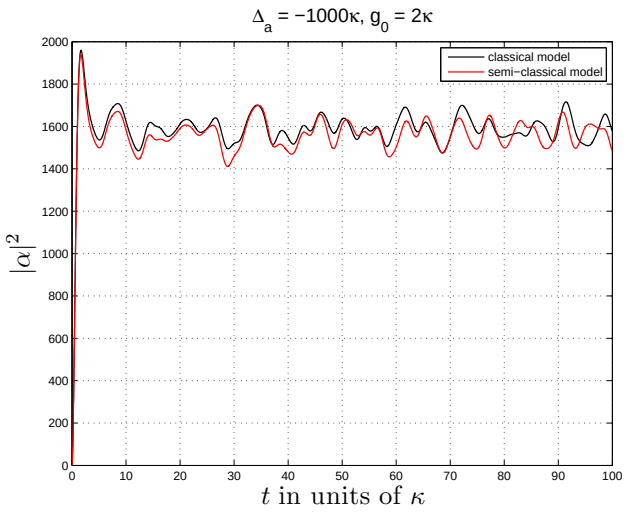

Figure 4.4: Comparison of the field intensity evolution of the classical (black curve) and semiclassical model (red curve) for far detuned fields in the cavity pump configuration. The parameters used are: $N = 1 \times 10^3$, $\eta = 70\kappa$, $\Delta_a = -1000\kappa$, $g_0 = 2.0\kappa$

Using the same parameters as previously, i.e.: $N = 1000$, $\eta = 70.0\kappa$ and with large pump-atom detuning $\Delta_a = -1000\kappa$ the agreement seems to be excellent even for longer times as shown in the three following figures:

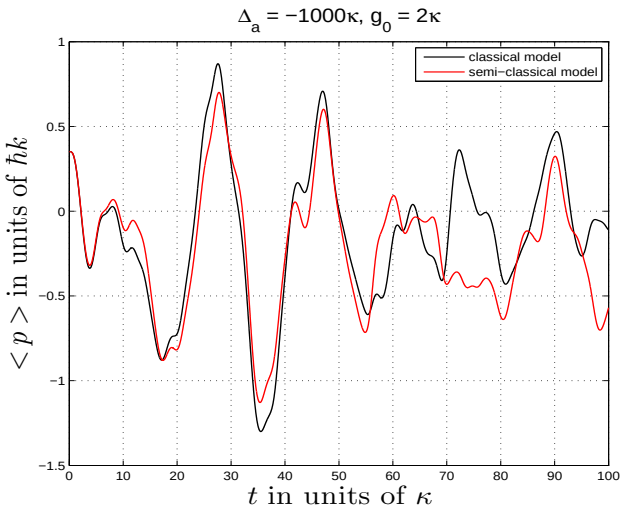

Figure 4.5: Comparison of the average momentum evolution of the classical (black curve) and semiclassical model (red curve) for a far detuned field in the cavity pump configuration. The parameters used are: $N = 1 \times 10^3$, $\eta = 70\kappa$, $\Delta_a = -1000\kappa$, $g_0 = 2.0\kappa$

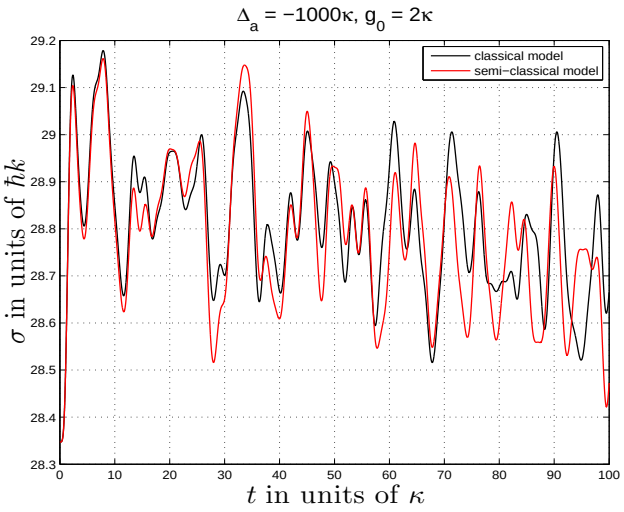

Figure 4.6: Comparison of the momentum spread evolution of the classical (black curve) and semiclassical model (red curve) for far detuned field in the cavity pump configuration. The parameters used are: $N = 1 \times 10^3$, $\eta = 70\kappa$, $\Delta_a = -1000\kappa$, $g_0 = 2.0\kappa$

Comparison of the classical model (eqs. (2.20) - (2.22)) and the semi-classical model (eqs. (4.38) - (4.41)) within the same negligible atomic excitation regime have been

carried out in this section. The results from numerical simulations using both models show excellent agreement and confirm the analytical result obtained in section 4.1.4 showing that for the negligible excitation of the atomic ensemble the semi-classical model is equivalent to the classical one.

4.3 Cooling Atoms with Blue Detuned Light

The results of the previous section show that in the low excitation regime ($\langle D \rangle \approx 1/2$), the semi-classical model agrees well with its classical counterpart. When atomic excitation is significant however ($\langle D \rangle \ll 1/2$) the classical model is, in principle, not sufficient approximation and may not fully represent the physical processes occurring in the system. Another advantage of the semi-classical model relies in the possibility of simulating cavity cooling processes in which the internal degrees of freedom of the atoms play an active part in the cooling mechanism. Such a process can occur when the cavity field is blue detuned with respect to the atomic resonance regime that involves stimulated emission and can lead to Sisyphus cooling as described in section 1.4.2.

As an example of cavity cooling using blue detuning, a setup similar to the UCL experiment is assumed. As mentioned earlier in section 1.5.3, the experiment involved the following parameters:

Number of atoms:	N	$\sim 1 \times 10^6$
Cavity linewidth:	κ	$= 10.0 \times 10^6\ Hz$
Laser wavelength:	λ	$= 852.4 \times 10^{-9}\ m$
Cs decay rate:	Γ_{lw}	$= 32.89 \times 10^6\ Hz$
Coupling constant:	g_0	$= 222.38 \times 10^3\ Hz$
Cs mass:	m	$= 2.21 \times 10^{-25}\ kg$

Initial temperature:	T_{ini}	$= 160.0 \times 10^{-6}\ K$
Pump-atom detuning:	Δ_A	$= (-250 : 250) \times 10^{6}\ Hz$
Laser power:	P	$\leq 0.3\ W$

Corresponding scaled parameters have been used in the series of numerical simulations with the semi-classical model, eqs. (4.38) - (4.41). The following simulations include the dependence of the cooling rate and the final temperature of the number on atoms in the cavity (figs. 4.7 and 4.8), pump-atom detuning (Δ_a) (figs. 4.9 and 4.10), pump-cavity detuning (Δ_c) (figs. 4.11 and 4.12) and the pump strength (η) (figs. 4.13 and 4.14):

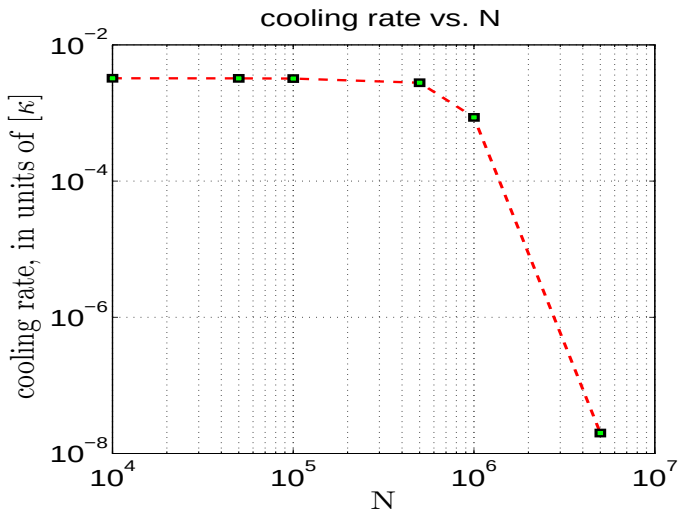

Figure 4.7: Cooling rates for blue detuned light calculated using the semi-classical model for varying number of atoms N. The parameters used are: $\eta = 2300.0\kappa$, $\Delta_a = 125\kappa$, $\Delta_c = 0.4\kappa$, $\Gamma = 3.25\kappa$, $g_0 = 0.02\kappa$, $\sigma = 28.0\hbar k$

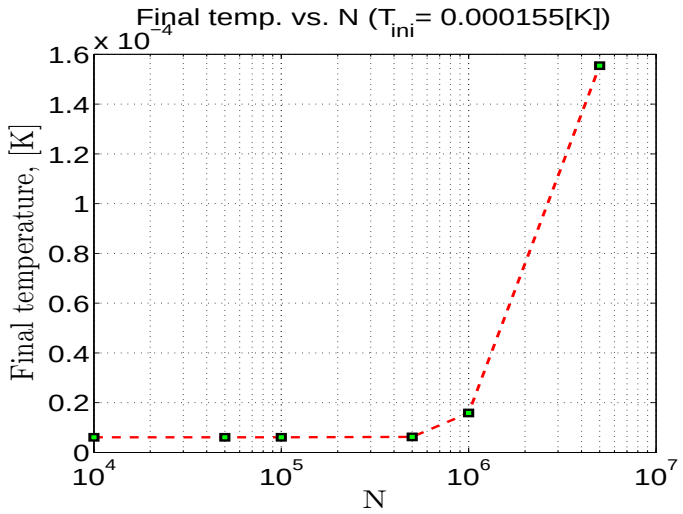

Figure 4.8: Final temperatures for blue detuned light calculated using the semi-classical model for varying number of atoms N. The parameters used are: $\eta = 2300.0\kappa$, $\Delta_a = 125\kappa$, $\Delta_c = 0.4\kappa$, $\Gamma = 3.25\kappa$, $g_0 = 0.02\kappa$, $\sigma = 28.0\hbar k$

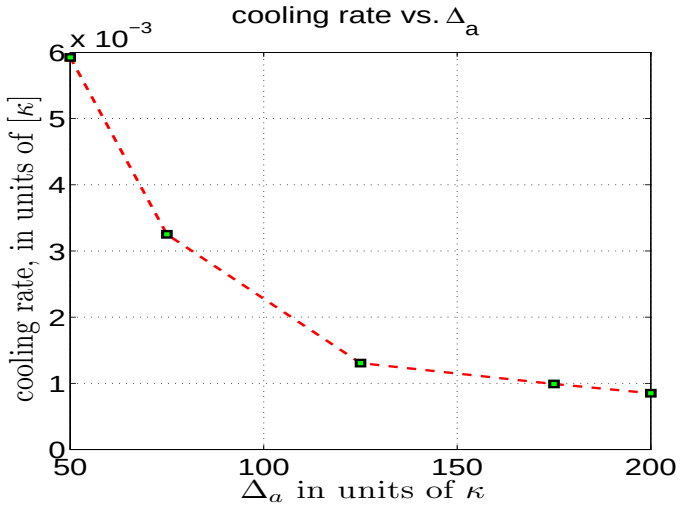

Figure 4.9: Cooling rates for blue detuned light calculated using the semi-classical model for varying pump-atom detuning Δ_a. The parameters used are: $N = 1 \times 10^6$, $\eta = 2300.0\kappa$, $\Gamma = 3.25\kappa$, $g_0 = 0.02\kappa$, $\sigma = 28.0\hbar k$

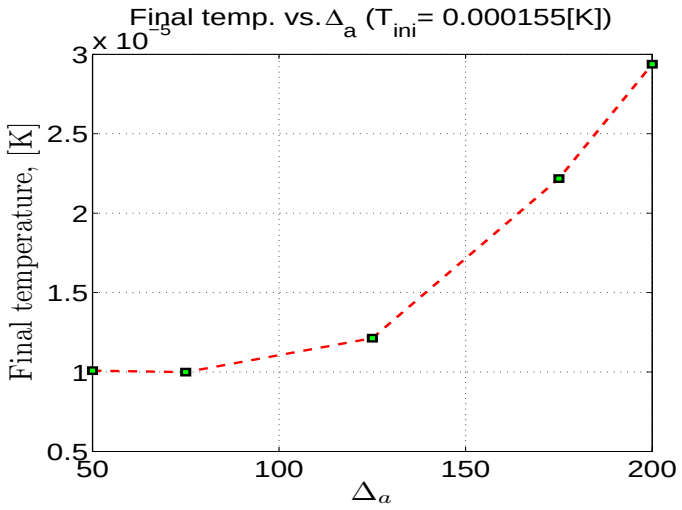

Figure 4.10: Final temperatures for blue detuned light calculated using the semi-classical model for varying pump-atom detuning Δ_a. The other parameters used are: $N = 1 \times 10^6$, $\eta = 2300.0\kappa$, $\Gamma = 3.25\kappa$, $g_0 = 0.02\kappa$, $\sigma = 28.0\hbar k$

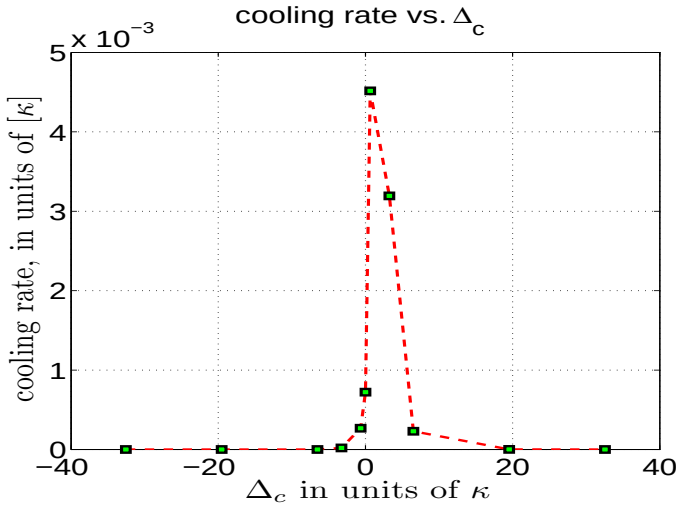

Figure 4.11: Cooling rates for blue detuned light calculated using the semi-classical model for varying pump-cavity detuning Δ_c. The other parameters used are: $N = 1 \times 10^6$, $\eta = 2300.0\kappa$, $\Delta_a = 75.0\kappa$, $\Gamma = 3.25\kappa$, $g_0 = 0.02\kappa$, $\sigma = 28.0\hbar k$

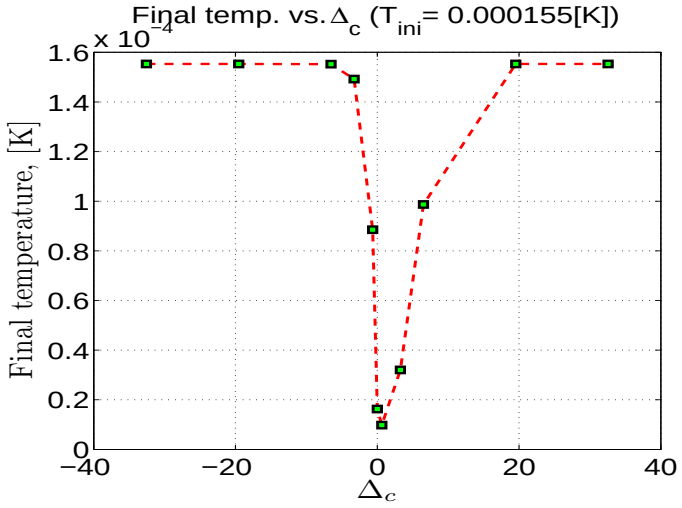

Figure 4.12: Final temperatures for blue detuned light calculated using the semi-classical model for varying pump-cavity detuning Δ_c. The other parameters used are: $N = 1 \times 10^6$, $\eta = 2300.0\kappa$, $\Delta_a = 75.0\kappa$, $\Gamma = 3.25\kappa$, $g_0 = 0.02\kappa$, $\sigma = 28.0\hbar k$

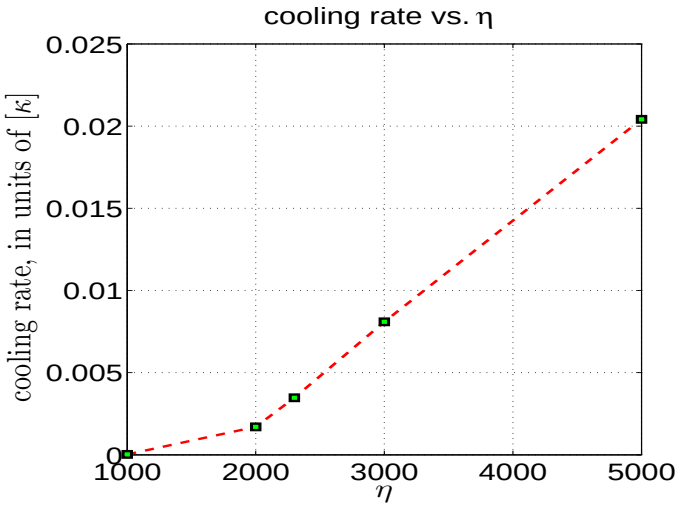

Figure 4.13: Cooling rates for blue detuned light calculated using the semi-classical model for varying pumping strength η. The other parameters used are: $N = 1 \times 10^3$, $\Delta_a = 125\kappa$, $\Delta_c = 0.7\kappa$, $\Gamma = 3.25\kappa$, $g_0 = 0.02\kappa$, $\sigma = 28.0\hbar k$

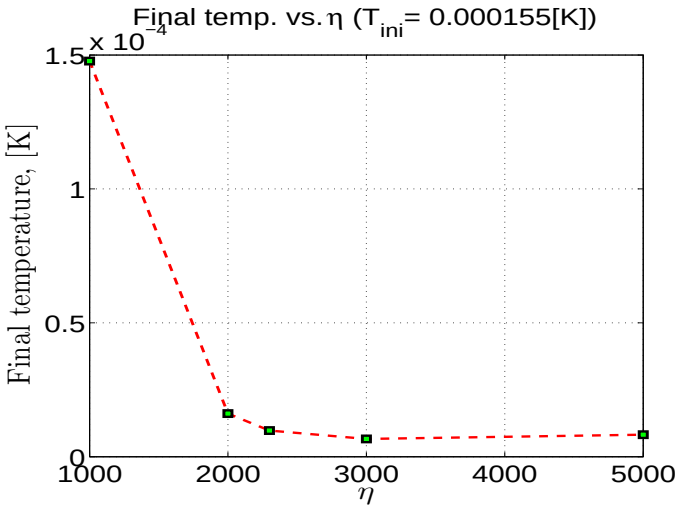

Figure 4.14: Final temperatures for blue detuned light calculated using the semi-classical model for varying pumping strength η. The other parameters used are: $N = 1 \times 10^3$, $\Delta_a = 125\kappa$, $\Delta_c = 0.7\kappa$, $\Gamma = 3.25\kappa$, $g_0 = 0.02\kappa$, $\sigma = 28.0\hbar k$

The first series of simulations for different numbers of particles ($N = 1 \times 10^4 \ldots 5 \times 10^6$ particles), fig. 4.7 and fig. 4.8, shows very fast cooling – almost independent of the number of particles inside the cavity (for comparison see the graphs of cooling rate vs. N for red detuned light in fig. 2.5). A significant decrease of the cooling rate was observed for samples containing more that 5×10^6 particles. Such a drop of cooling rate indicates a lack of a cooperative effect in this configuration. Similarly, the final temperatures for up to 1×10^6 particles reached values below $20\mu K$ and heating was seen for 5×10^6.

The second series of simulations for different pump-atom detunings ($\Delta_a = 50, 75, 125, 175, 200\kappa$), fig. 4.9 and fig. 4.10, shows a higher cooling rate for small detuning that decreases rapidly for larger detunings and reaches a minimum for $\Delta_a = 200$. The final temperature (initially $\sim 160\mu K$) varies from $30\mu K$ for $\Delta_a = 50\kappa$ to $110\mu K$ for $\Delta_a = 200\kappa$. Oscillations of the final momentum spread σ are responsible for the discrepancy of the final temperature for $\Delta_a = 50, 75\kappa$ (fig. 4.10).

In the third series of simulations for different pump-cavity detunings, fig. 4.11 and fig. 4.12, a narrow region of cooling was observed. The region extends from approximately $\Delta_c = 0.0\kappa$ to $\Delta_c = 5.0\kappa$, outside which the cooling rate decreases dramatically. The final temperature falls into the same region and reaches a minimum of $30\mu K$ for $\Delta_c \approx 1.0\kappa$. For all other values of Δ_c no cooling was observed.

The last, fourth series of simulations for different pump strengths (η), fig. 4.13 and 4.14, indicates rapid growth of the cooling rate for higher intensity. Such behaviour is rather characteristic for a Sisyphus-type cooling schemes. Despite the fact the cooling rate can increase with the pump intensity the final temperature can be limited by the optical potential energy associated with the cavity mode amplitude, which can be seen on fig. 4.14 where the similar final temperatures were obtained

for $\eta = 2, 3, 4, 5 \times 10^3 \kappa$. However it needs to be mentioned that the cooling was observed unchanged even when the field evolution was switched off i.e. α fixed at a value $\propto \frac{\eta}{\kappa + \Delta_c^2}$ (as obtained from the steady state of the field equation (4.41)). This leads to the conclusion that the role of the cavity is only to convert a unidirectional travelling wave pump field into a bidirectional standing wave field of higher intensity, and the dynamical evolution of the cavity field does not play a significant role. In this sense the cooling process is essentially that of free space blue molasses as originally discovered by Aspect et al. [32]

Chapter 5

Semi-Classical Model of Atom-Pump Configuration

In chapter 3 a classical model of the atom-pump configuration was derived. In this section this model is extended to include semi-classical atomic dynamics. The results from both classical and semi-classical models of atom-pumping are compared and found to agree within the limit where atomic excitation is negligible.

5.1 Derivation of Semi-Classical Model of Atom-Pump Configuration

As in chapter 4 the situation considered is an ensemble/gas of two-level atoms confined inside a Fabry-Perot resonator. Unlike in the cavity pump configuration described in chapter 4, here the atoms are directly illuminated by the pump field which travels perpendicular to the cavity axis as shown in fig 5.1. The field is assumed to be detuned from any atomic resonance.

5.1.1 Internal Degrees of Freedom

Following the derivation described in section 4.1, it assumed that the atoms have two internal energy states. The lower and upper energy states are labelled $|g\rangle$ and

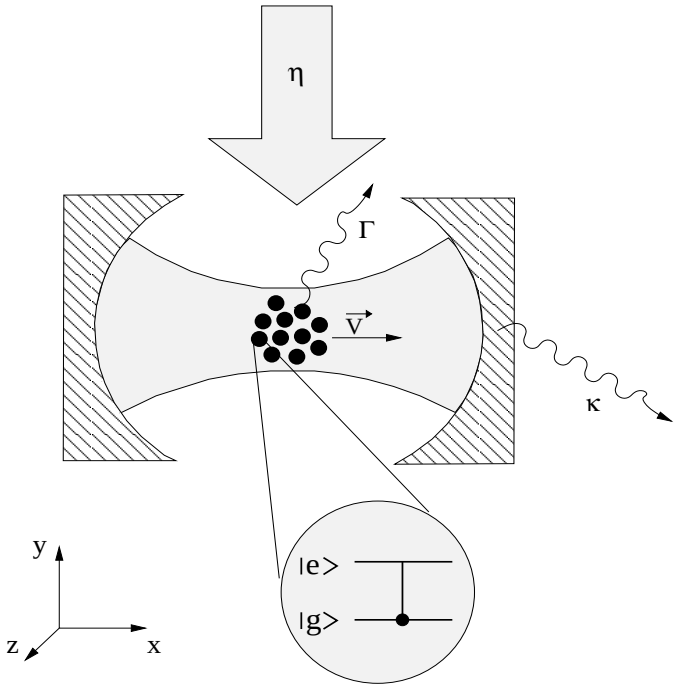

Figure 5.1: Two-level atom in a cavity (atom-pump configuration). The cavity pumping rate, spontaneous loss rate and cavity decay rate are determined by the parameters η, Γ and κ respectively. $|g\rangle$ represents a ground state of an atom while $|e\rangle$ represents an excited state of an atom

$|e\rangle$ respectively. The Bloch equations for the density matrix elements $\rho_{jk}, j, k = e, g$ are the same as those for the cavity-pump configuration but are restated here for completeness:

$$\frac{\partial \rho_{eg}}{\partial t} = -\left(\Gamma_{eg} + i\omega_{eg}\right)\rho_{eg} + \frac{iE\mu}{\hbar}\left(\rho_{gg} - \rho_{ee}\right) \tag{5.1}$$

$$\frac{\partial}{\partial t}\left(\rho_{gg} - \rho_{ee}\right) = -\Gamma_{ee}\left(\rho_{gg} - \rho_{ee}\right) + \frac{2iE\mu}{\hbar}\left(\rho_{eg} - \rho_{eg}^{*}\right) \tag{5.2}$$

As before, the dipole moment is

$$\boldsymbol{d}_j = \mu\left(\rho_{ge} + \rho_{ge}^{*}\right)\hat{\boldsymbol{e}} \tag{5.3}$$

and the density matrix element

$$\rho_{eg} = Se^{-i\omega t}, \quad (\rho_{ge} = \rho_{eg}^{*}). \tag{5.4}$$

The field in the atom-pump configuration includes two waves

$$E_1 = \left(A_1 e^{-i\omega t} + c.c.\right) g(x) \tag{5.5}$$

$$E_2 = \left(A_2 e^{-i\omega t} + c.c.\right) h(y) \tag{5.6}$$

where the E_1 and E_2 are the cavity and the pump fields respectively. and so the total field will be of the form

$$E = \left(A_1 e^{-i\omega t} g(x) + A_2 e^{-i\omega t} h(y) + c.c.\right) \tag{5.7}$$

where g(x) and h(y) are cavity mode functions and it has been assumed that $\boldsymbol{E_1} = E_1\hat{\boldsymbol{z}}$, $\boldsymbol{E_2} = E_2\hat{\boldsymbol{z}}$, $\boldsymbol{\mu}_{ge} = \boldsymbol{\mu}_{eg} = \mu\hat{\boldsymbol{z}}$,

Inserting (5.4) and (5.7) into (5.1) gives

$$\frac{dS}{dt} = -\Gamma_{eg} S - i\left(\omega_{eg} - \omega\right) S + \frac{2i\mu D}{\hbar}\left(A_1 g(x) + A_2 h(y)\right) \tag{5.8}$$

where we have used the population difference variable defined in chapter 4, $D = \left(\rho_{gg} - \rho_{ee}\right)/2$ and neglected terms varying as $e^{2i\omega t}$.

Similarly, substituting for (5.4), (4.5) and (5.7) into (5.2) gives

$$\frac{dD}{dt} = -\Gamma_{ee}\left(D - D^{eq}\right) - \frac{i\mu}{\hbar}\left\{\left[A_1 g(x) + A_2 h(y)\right] S^{*} - c.c.\right\} \tag{5.9}$$

where $D^{eq} = 0.5$ in the absence of any external excitation of the atom and we have

dropped fast oscillating terms.

Equations (5.8) and (5.9) describe the internal degrees of freedom of each atom under the influence of the cavity field in the atom-pump configuration.

5.1.2 Atomic Centre-of-Mass Dynamics

As in chapter 4, the external degrees of freedom of atoms - the position and momentum - are described classically.

The dipole force in the x direction acting on the jth atom is given by:

$$F_x = \boldsymbol{d}_j \cdot \frac{d\boldsymbol{E}}{dx} = \left(\frac{d_x \partial E_x}{\partial x} + \frac{d_y \partial E_y}{\partial x} + \frac{d_z \partial E_z}{\partial x} \right) = \frac{d_z \partial E_z}{\partial x}. \tag{5.10}$$

Substituting the dipole moment

$$d_z = \mu \left(S e^{-i\omega t} + c.c \right) \tag{5.11}$$

and the total field derivative

$$\frac{\partial E_z}{\partial x} = \left(A e^{-i\omega t} + c.c. \right) \frac{dg(x)}{dx} \tag{5.12}$$

into (5.10) gives the final expression of the dipole force in the x direction

$$F_x = \mu \left(A^* S + S^* A\right) \frac{dg(x)}{dx}. \tag{5.13}$$

5.1.3 Electromagnetic Field Dynamics

Following similar procedure to that of section 4.1.3 and starting with Maxwell's wave equation

$$\left(\nabla^2 - \frac{1}{c^2}\frac{\partial^2}{\partial t^2} - \mu_0 \sigma \frac{\partial}{\partial t}\right) \boldsymbol{E} = \frac{1}{\epsilon_0 c^2}\frac{\partial^2 \boldsymbol{P}}{\partial t^2} \tag{5.14}$$

where σ is the conductivity of the cavity mirrors, μ_o is the magnetic permeability and the polarisation $\boldsymbol{P}$ is defined as

$$\begin{aligned} \boldsymbol{P} &= \sum_j \boldsymbol{d}_j \; \delta\left(\boldsymbol{r} - \boldsymbol{r}_j\right) \\ &= \mu \hat{\boldsymbol{e}} \sum_j \left(S e^{-i\omega t} + c.c.\right) \delta\left(\boldsymbol{r} - \boldsymbol{r}_j\right) \end{aligned} \tag{5.15}$$

where eq. (5.4) has been used.

After finding the derivatives the wave equation eq. (5.14) can be rewritten as

$$\left[k^2 A_1 - \frac{i2\omega}{c^2}\frac{dA_1}{dt} - \frac{\omega^2}{c^2}A_1 - i\omega\mu_0\sigma A_1\right] g(x)e^{-i\omega t} + c.c. =$$

$$\mu_0\omega^2\mu \sum_j \left(Se^{-i\omega t} + c.c.\right)\delta\left(\boldsymbol{r} - \boldsymbol{r}_j\right)$$

$$\left[k^2 A_1 - \frac{i2\omega}{c^2}\frac{dA_1}{dt} - \frac{\omega^2}{c^2}A_1 - i\omega\mu_0\sigma A_1\right] g(x) =$$

$$\mu_0\omega^2\mu \sum_j S\delta\left(\boldsymbol{r} - \boldsymbol{r}_j\right) \tag{5.16}$$

where we have assumed the slowly-varying envelope approximation (SVEA), i.e. $\frac{\partial A_1}{\partial t} << \omega A_1$.

Multiplying both sides of (5.16) by $-c^2/i\ 2\omega$ we get

$$\left[-\frac{\omega_c^2 A_1}{2i\omega} + \frac{dA_1}{dt} + \frac{\omega^2 A_1}{2i\omega} + \frac{c^2\mu_0\sigma A_1}{2}\right] g(x) = \frac{i\mu_0\omega c^2\mu}{2} \sum_j S\delta\left(\boldsymbol{r} - \boldsymbol{r}_j\ \delta\right) \tag{5.17}$$

In the first and third terms of the LHS of eq. (5.17) the cavity and the pump field frequency are ω_c and ω respectively. These terms can be a further approximated since

$$-\frac{(\omega_c^2 - \omega^2)}{2\ i\ \omega} = -\frac{(\omega_c - \omega)(\omega_c + \omega)}{2\ i\ \omega} = \frac{\Delta_c 2\omega}{2\ i\ \omega} = -i\Delta_c \tag{5.18}$$

where $\Delta_c = \omega - \omega_c$ is the pump-cavity frequency detuning. Hence equation (5.17) becomes

$$\left[\frac{dA_1}{dt} + (\kappa - i\Delta_c)\, A_1\right] g(x) = \frac{i\omega\mu}{2\epsilon_0} \sum_j S\delta\left(\boldsymbol{r} - \boldsymbol{r}_j\right) \tag{5.19}$$

as

$$c = \frac{1}{\sqrt{\epsilon_0 \mu_0}}, \quad \kappa = \frac{\sigma}{2\epsilon_0} \tag{5.20}$$

Multiplying both sides of (5.19) by $g(x)$ and integrating over the cross-section area of the sample $\mathcal{A}$, gives

$$\mathcal{A}\frac{dA_1}{dt}\int_0^L g(x)^2 dx + (\kappa - i\Delta_c)\, A_1 \mathcal{A}\int_0^L g(x)^2 dx = \frac{i\mu\omega}{2\epsilon_0}\sum_j S_j g(x) \tag{5.21}$$

Substituting the cavity mode function of the form

$$g(x) = cos(kx) \tag{5.22}$$

into eq. (5.21) produces

$$\frac{dA_1}{dt} = (-\kappa + i\Delta_c)\, A_1 + \frac{2i\mu\omega}{\mathcal{A}\lambda\epsilon_0}\sum_j S g(x) \tag{5.23}$$

which can be further simplified and the final form of the field equation becomes

$$\frac{dA_1}{dt} = (-\kappa + i\Delta_c)\, A_1 + \frac{i\mu\omega}{V\epsilon_0}\sum_j S g(x) \tag{5.24}$$

Equations (5.8), (5.9), (5.13) and (5.24) make a closed set of evolution equations

which completely describe the self-consistent interaction of an ensemble of two-level atoms with the cavity mode inside a Fabry-Perot cavity:

$$\frac{dS_j}{dt} = -\Gamma_{eg} S_j + i\left(\omega - \omega_{eg}\right) S_j + \frac{2i\mu D}{\hbar}\left(A_1 g(x) + A_2 h(y)\right) \tag{5.25}$$

$$\frac{dD_j}{dt} = -\Gamma_{ee}\left(D_j - D^{eq}\right) - \frac{i\mu}{\hbar}\left\{\left[A_1 g(x) + A_2 h(y)\right] S_j^* - c.c.\right\} \tag{5.26}$$

$$\frac{dp_j}{dt} = \mu\left(S_j A_1^* + S_j^* A_1\right)\frac{dg(x)}{dx} \tag{5.27}$$

$$\frac{dA_1}{dt} = \left(-\kappa + i\Delta_c\right) A_1 + \frac{i\mu\omega}{V\epsilon_0}\sum_j S_j g(x) \tag{5.28}$$

Rewriting eqs. (5.25 - 5.28) in terms of α defined in eq. (4.24)

then equations (5.25)-(5.28) for (1D) become

$$\frac{dS_j}{dt} = -\Gamma_{eg} S_j + i\Delta_a S_j + 2ig_0 D(\alpha_1 cos(kx) + \alpha_2) \tag{5.29}$$

$$\frac{dD_j}{dt} = -\Gamma_{ee}\left(D_j - D^{eq}\right) - ig_0\left\{\left[\alpha_1 cos(kx) + \alpha_2\right] S_j * - c.c.\right\} \tag{5.30}$$

$$\frac{dp_j}{dt} = -\hbar k g_0\left(S_j \alpha_1^* + S_j^* \alpha_1\right) sin(kx) \tag{5.31}$$

$$\frac{d\alpha_1}{dt} = \left(-\kappa + i\Delta_c\right)\alpha_1 + ig_0 \sum_j S_j cos(kx_j) \tag{5.32}$$

where $\Delta_a = \omega - \omega_{eg}$ is the pump – atom detuning and $g_o = \mu\sqrt{\frac{\omega}{\hbar\epsilon_o V}}$ is the atom-cavity coupling constant.

5.1.4 Comparison with the Classical Model

In order to compare the classical and the semi-classical equations for the atom-pump configuration we must remain within the same regime for both models. As stated

before the validity of the classical model that has been presented earlier implies low excitation condition of the atomic ensemble so within that limit the semi-classical model should reduce to the classical model.

Lets assume all atoms to be in a ground state. Setting $D = 1/2$, as the condition for negligible excitation, then at steady state equation (5.29) can be written as

$$S_j = \frac{ig_0(\alpha_1 cos(kx_j) + \alpha_2)}{\Gamma_{eg} - i\Delta_a} \tag{5.33}$$

Substituting the steady state of the coherence variable S, (eq. 5.33) into the force equation, (eq. 5.31), gives

$$\begin{aligned} F_x = &- \hbar k g_0 \left[\frac{-ig_0(|\alpha_1|^2 cos(kx_j) + \alpha_1\alpha_2^*)}{\Gamma_{eg} - i\Delta_a} + \frac{ig_0(|\alpha_1|^2 cos(kx_j) + \alpha_1^*\alpha_2)}{\Gamma_{eg} + i\Delta_a} \right] sin(kx_j) \\ \Rightarrow &- \hbar k \left[\frac{-2ig_0^2|\alpha_1|^2 cos(kx_j)\Delta_a}{\Gamma_{eg}^2 + \Delta_a^2} - \frac{ig_0\alpha_1\alpha_2^*}{\Gamma_{eg} - i\Delta_a} + \frac{ig_0\alpha_1\alpha_2^*}{\Gamma_{eg} + i\Delta_a} \right] sin(kx_j) \end{aligned} \tag{5.34}$$

Rearranging eq. 5.34 and recalling that the frequency shift and the position dependent scattering rate are defined as

$$\gamma(x) = \frac{\Gamma}{\Gamma^2 + \Delta_a^2} g_o^2 cos^2(kx) = \gamma_o cos^2(kx) \ , \tag{5.35}$$

$$U(x) = \frac{\Delta_a}{\Gamma^2 + \Delta_a^2} g_o^2 cos^2(kx) = U_o cos^2(kx) \ . \tag{5.36}$$

gives

$$F_x = -\hbar U_0 |\alpha|^2 \frac{d}{dx} cos^2(kx_j) - i\hbar \left(\eta_{eff}^* \alpha_1 - \eta_{eff} \alpha_1^* \right) \frac{d}{dx} cos(kx_j) \tag{5.37}$$

where we have used the trigonometric identity $sin(2kx) = 2sin(kx)cos(kx)$ and where

$$\eta = g_0\alpha_2 \tag{5.38}$$

and

$$\eta_{eff} = \frac{\eta g_0}{\Gamma - i\Delta_a} \tag{5.39}$$

Equation 5.37 is the same equation as derived in section 3.1, eq. (3.39) for the classical model.

Similarly substituting the steady state value of S (5.33) into the derived field equation (5.32) gives

$$\begin{aligned}\frac{d\alpha_1}{dt} &= (-\kappa + i\Delta_c)\,\alpha_1 + ig_0 \sum_j \left(\frac{ig_0\alpha_1}{\Gamma_{eg} - i\Delta_a} cos(kx_j) + \frac{ig_0\alpha_2}{\Gamma_{eg} - i\Delta_a}\right) cos(kx_j) \\ &= (-\kappa + i\Delta_c)\,\alpha_1 - \alpha_1\,(\gamma_0 + iU_0) \sum_j cos^2(kx_j) - \eta_{eff} \sum_j cos(kx_j)\end{aligned} \tag{5.40}$$

where we have again used known identities (5.35), (5.36), (5.38) and (5.39)

After rearranging (5.40) we finally obtain

$$\frac{d\alpha}{dt} = i\Big[\Delta_c - U_o \sum_j cos^2(kx_j)\Big]\alpha - \Big[\ \kappa + \gamma_o \sum_j cos^2(kx_j)\Big]\alpha - \eta_{eff} \sum_j cos(kx_j) \tag{5.41}$$

which is the same equation as derived in section 3.1 see eq. (3.38) from the classical model. As expected, the semi-classical model within the limit of low excitation simplifies to the classical model.

In the next section, results from numerical simulations of the classical model and the semi-classical model will be compared.

5.2 Comparison Between the Classical and the Semi-Classical Models (Numerical Simulations)

It is instructive to show, using numerical results, that in the low excitation limit the semi-classical model shows similar behaviour to that of the classical model, as predicted by the analysis described in section 5.1.4. The classical model eqs. (3.38 - 3.40) and the semi-classical model, eqs. (5.29 - 5.32) have been solved numerically for the same initial parameters and the results are presented below.

Figure 5.2 shows the time evolution of the field intensity within the time period of $t = 100\kappa$. The number of atoms here is 1×10^3, $\Delta_a = -1000\kappa$ (rather large pump-atom detuning), $g_0 = 1.0\kappa$ and $\eta = 100\kappa$. It can be seen that both models show very good agreement during the entire time of interaction. In both models the field evolution is seen to display small oscillations.

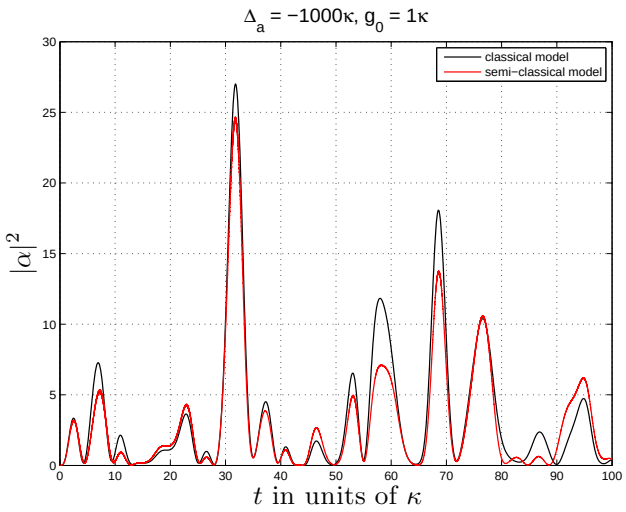

Figure 5.2: Comparison of the field intensity evolution of the classical (black curve) and semiclassical model (red curve) for a far detuned field in the atom-pump configuration. The parameters used are: $N = 1 \times 10^3$, $\eta = 100\kappa$, $\Delta_a = -1000\kappa$, $g_0 = 1.0\kappa$

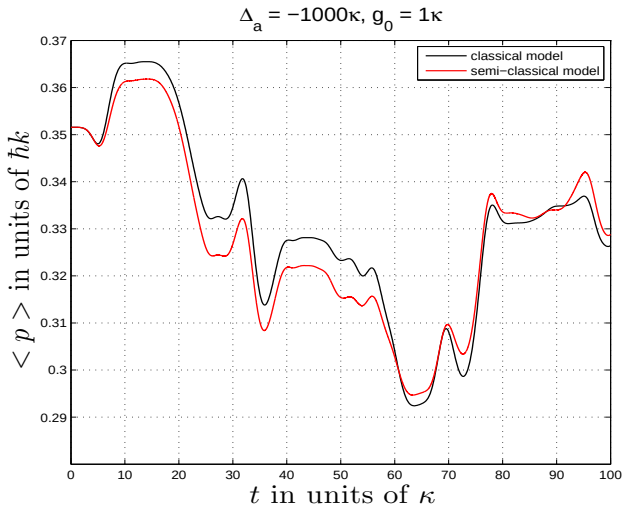

Figure 5.3: Comparison of the average momentum evolution of the classical (black curve) and semiclassical model (red curve) for a far detuned field in the atom-pump configuration. The parameters used are: $N = 1 \times 10^3$, $\eta = 100\kappa$, $\Delta_a = -1000\kappa$, $g_0 = 1.0\kappa$

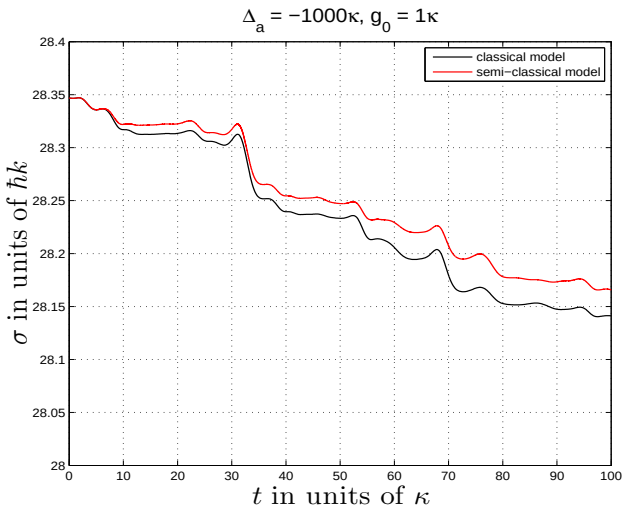

Figure 5.4: Comparison of the momentum spread evolution of the classical (black curve) and semiclassical model (red curve) for a far detuned field in the atom-pump configuration. The parameters used are: $N = 1 \times 10^3$, $\eta = 100\kappa$, $\Delta_a = -1000\kappa$, $g_0 = 1.0\kappa$

The time evolution of the average momentum, and the momentum spread is presented in fig. 5.3 and fig. 5.4, respectively. Both figures compare the results from the classical and the semi-classical models within a short time period of $t = 100\kappa^{-1}$ and for the same parameters as used in the previous figure (N$= 1 \times 10^3$, $\Delta_a = -1000\kappa$, $g_0 = 1.0\kappa$, $\eta = 100\kappa$). As expected, the results from both models again agree very well and confirm the analytical result obtained in the previous section 5.1.4.

5.3 Cooling Atoms with Blue Detuned Light (Atom-Pump Configuration)

In the previous section the results from numerical simulation of the classical model (eqs. (3.38 - 3.40)) and the semi-classical model (eqs. (5.29 - 5.32)) for the case of the atom-pump configuration were compared. As shown, in the negligible atomic excitation regime, the results confirmed (with the analytical result, section 5.1.4)

excellent agreement between the two models. However, as demonstrated earlier in section 4.3 the semi-classical model has an advantage in that it can describe cavity cooling processes in which the internal degrees of freedom of the atoms play an active part in the cooling mechanism. In the case when the cavity field is blue detuned with respect to the atomic resonance, stimulated emission can lead to Sisyphus cooling as described in section 1.4.2. In this section an example of cavity cooling using blue detuned light for the case of the atom-pump configuration is demonstrated.

The semi-classical model equations (eqs. (5.29 - 5.32)) have been solved numerically for the following parameters: $N = 1 \times 10^3$, $\Delta_a = 1000\kappa$, $\eta = 400\kappa$, $\Gamma_{ee} = \Gamma_{eg} = 1.0\kappa$ and the results are presented in the figures below.

Fig. 5.5 shows the time evolution of the field intensity. The field intensity grows rapidly within $\kappa t \approx 2500$ and slowly saturates for longer times.

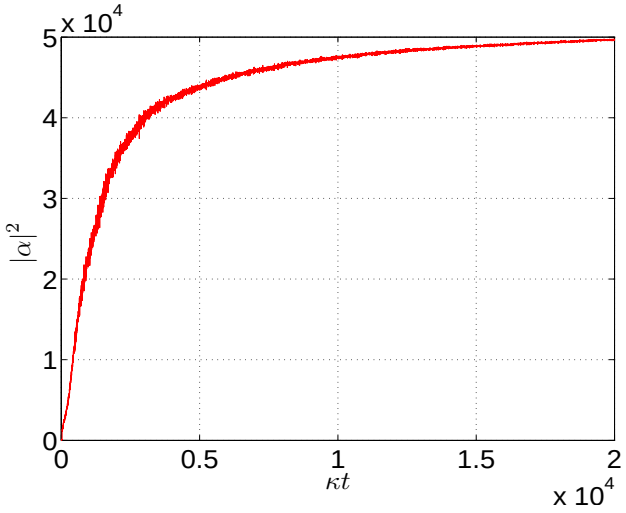

Figure 5.5: Time evolution of the field intensity calculated from a numerical simulation of the semiclassical model (eqs. (5.29 - 5.32)) for blue detuned light in the atom-pump configuration. Parameters used are: $N = 1 \times 10^3$, $\Delta_a = 1000\kappa$, $\eta = 400\kappa$, $\Gamma_{ee} = \Gamma_{eg} = 1.0\kappa$

The evolution of the field intensity shown in fig. 5.5 is strongly correlated with the evolution of the bunching parameter (fig. 5.6), $|b|$, and the evolution of the

momentum spread (fig. 5.7) with respect to time.

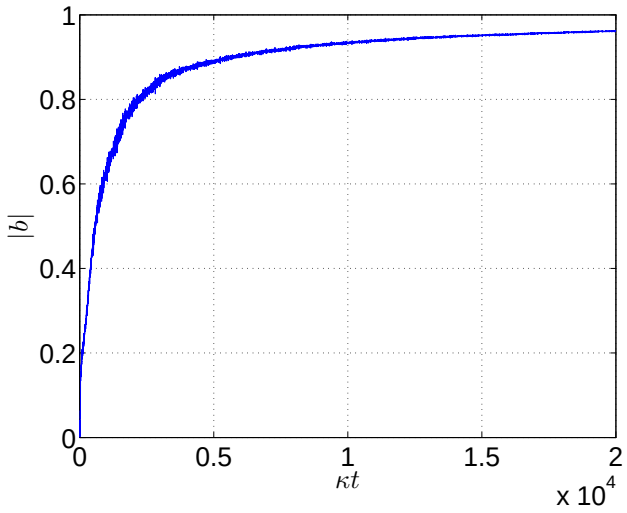

Figure 5.6: Time evolution of the bunching, $|b|$, parameter calculated from a numerical simulation of the semiclassical model (eqs. (5.29 - 5.32)) for blue detuned light in the atom-pump configuration. Parameters used are: $N = 1 \times 10^3$, $\Delta_a = 1000\kappa$, $\eta = 400\kappa$, $\Gamma_{ee} = \Gamma_{eg} = 1.0\kappa$

The time evolution of the bunching parameter $|b|$ (fig. 5.6) indicates very strong bunching of the atoms in the cavity. The steady state value of $|b|$ for $\kappa t > 1 \times 10^4$ approaches $|b| \approx 1$ which, as mentioned in section 3.2, is responsible for collective scattering of the light on atoms and their self-organisation in the optical potentials.

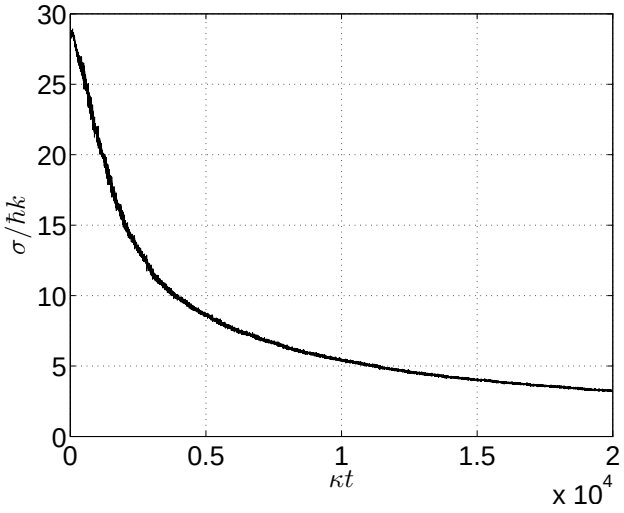

Figure 5.7: Time evolution of the momentum spread calculated from a numerical simulation of the semiclassical model (eqs. (5.29 - 5.32)) for blue detuned light in the atom-pump configuration. Parameters used are: $N = 1 \times 10^3$, $\Delta_a = 1000\kappa$, $\eta = 400\kappa$, $\Gamma_{ee} = \Gamma_{eg} = 1.0\kappa$

As explained in section 3.2 collective scattering and the self-organisation of atoms can lead to effective cooling of the atomic ensemble. This can be seen in fig. 5.7 showing the time evolution of the momentum spread. As the atoms redistribute in the cavity and increase the field intensity, the momentum spread decreases rapidly (fig. 5.7) indicating trapping and cooling of the atomic ensemble.

Chapter 6

Ring Cavity and Phase Modulated Pump Field

The previous chapters involved studies of the dynamics of an ensemble of atoms confined in a simple Fabry-Perot cavity (see fig. 2.4 and 3.1). The previously considered cases differ only in the direction of the pump field, however both are based on the standing wave cavity field for which the nodes and the antinodes of the oscillating field are fixed in space. This means that the potentials created by the field are also fixed in space and cannot travel inside the cavity. This restriction can be removed using a ring cavity with two counter propagating light fields inside (fig. 6.1). In this configuration the optical fields produce potentials that are not fixed in space but are able to move inside the cavity.

It has been recently shown that the effect of a phase-modulated beam on Collective Atomic Recoil Lasing (CARL) [58, 59] can give rise to three different dynamical regimes depending on the frequency of modulation [60]. Moreover it has been demonstrated experimentally [61] that even weakly modulated light can produce relatively strong optical forces that can be potentially used for cooling or deflection of moving atoms. In this chapter we will give a deeper insight into this idea and show how this can be used to control the dynamics of atoms and eventually for slowing or cooling atomic beams.

6.1 Model

The dynamics of N linearly polarisable particles moving inside a high-Q ring cavity can be, to a good approximation, described by four coupled classical equations of motion [62, 63]:

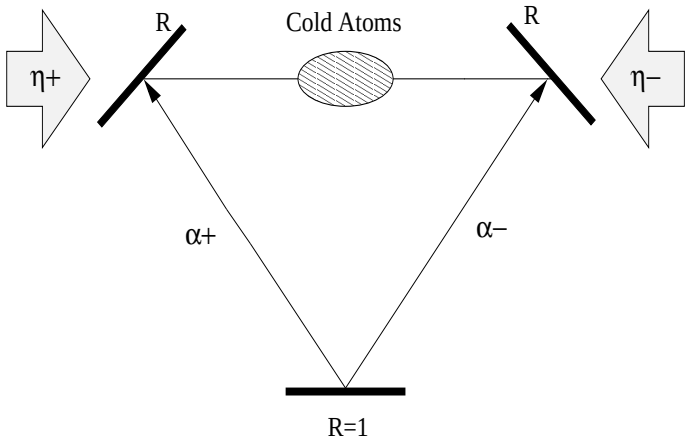

Figure 6.1: Schematic diagram of a bidirectional ring cavity driven by two monochromatic fields with pump rates η_+, η_-. α_- and α_+ are the amplitudes of the pump and the probe fields, respectively.

$$\frac{dx_j}{dt} = \frac{p_j}{m} \tag{6.1}$$

$$\frac{dp_j}{dt} = 2\hbar k \left[U_0 i \left(\alpha_+^* \alpha_- e^{-2ikx} - \alpha_-^* \alpha_+ e^{2ikx}\right) + \gamma_0 \left(\alpha_+^* \alpha_+ - \alpha_-^* \alpha_-\right)\right] \tag{6.2}$$

$$\frac{d\alpha_\pm}{dt} = \left[i\Delta_\pm - N(\gamma_0 + iU_0) - \kappa\right] \alpha_\pm - N(\gamma_0 + iU_0) \left\langle e^{\mp 2ikx} \right\rangle \alpha_\mp + \eta_\pm \tag{6.3}$$

If we restrict the general model to a uni-directionally pumped cavity only (see fig. 6.2) and modify it to include the effect of pump phase modulation the model becomes:

$$\frac{dx_j}{dt} = \frac{p_j}{m} \tag{6.4}$$

$$\frac{dp_j}{dt} = 2\hbar k U_0 i \left[\alpha_+^* \alpha_- e^{-2ikx} - \alpha_-^* \alpha_+ e^{2ikx}\right] \tag{6.5}$$

$$\frac{d\alpha_+}{dt} = \left[i\Delta_+ - NiU_0 - \beta\kappa_-\right]\alpha_+ - NiU_0 \left\langle e^{-2ikx}\right\rangle \alpha_- \tag{6.6}$$

$$\frac{d\alpha_-}{dt} = \left[i\Delta_- - NiU_0 - \kappa_-\right]\alpha_- - NiU_0 \left\langle e^{2ikx}\right\rangle \alpha_+ + \eta_- \, e^{(i\alpha_m sin(\Omega_m t))} \tag{6.7}$$

where $\gamma_0 \ll |U_0|$ has been assumed.

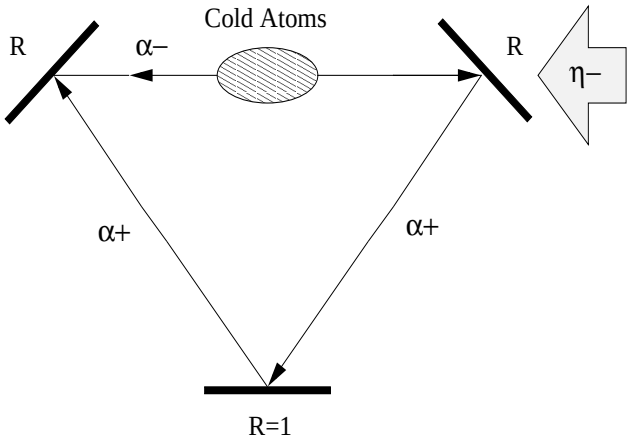

Figure 6.2: Schematic diagram of uni-directionally pumped ring cavity. Two counter propagating fields circulate in a high-finesse cavity, η_- is the pumping rate term, α_- and α_+ are the amplitudes of the pump and the probe fields, respectively.

The first two equations (6.4 - 6.5) describe the dynamics of the jth atom moving under the influence of the dipole force in the potential created by the counterpropagating cavity fields; x_j and p_j are the position and the momentum of jth atom respectively, m is the atomic mass and $k = 2\pi/\lambda$ is the wavenumber. Equations (6.6 - 6.7) describe the evolution of the amplitudes of the two counterpropagating fields: the pump field (α_-) and the backscattered probe field (α_+). The parameter $\beta = \frac{\kappa_+}{\kappa_-}$ describes the ratio of the probe (κ_+) and the pump (κ_-) cavity decay (note, the relative size of cavity decay rates can be modified using devices such as a Faraday

rotator [64, 65]). $\Delta_{\pm}$ is the cavity-field detuning for the probe (+) and the pump(-) field and U_0 is the effective mode frequency shift:

$$U_0 = \frac{\Delta_a}{\Gamma^2 + \Delta_a^2} g^2. \tag{6.8}$$

where Δ_a is the atom-pump detuning, Γ is the spontaneous emission linewidth and g the atom-mode coupling constant defined as $g^2 = e^2/4\epsilon_0 mV$. Here we have assumed that the pump and probe fields are far-detuned from any atomic resonance ($\Delta_a \gg \Gamma$).

The phase-modulated effective pumping rate, eq. (6.7) is:

$$\eta_- \; e^{(i\alpha_m sin(\Omega_m t))} \tag{6.9}$$

where η_- is the pumping rate term, α_m is the modulation strength and Ω_m is the phase modulation frequency of the cavity pump field.

6.2 CARL Instability and Derivation of a Growth Rate (g_r)

Finding the frequency modulation regimes requires finding the growth rate of the probe field intensity. The growth rate (g_r) can be found numerically using (eqs. (6.4) and (6.7) from the slope of the evolution of $|\alpha|^2$ in absence of pump modulation $\alpha_m = 0$. However the result can be confirmed by the result that can be found analytically using following approximation.

It is possible to introduce small fluctuations about the steady state system and see whether the system is stable and returns to the initial state or unstable and grows in time [66]. In absence of pump modulation $\alpha_m = 0$ the system of previously derived equations, (6.4) - (6.7) becomes

$$\frac{dx_j}{dt} = \frac{p_j}{m} \tag{6.10}$$

$$\frac{dp_j}{dt} = -2\hbar k U_0 i \left(\alpha_-^* \alpha_+ e^{2ikx} - c.c.\right) \tag{6.11}$$

$$\frac{d\alpha_+}{dt} = \left(i\Delta_+ - iNU_0 - \beta\right)\alpha_+ - iNU_0 \left\langle e^{-2ikx} \right\rangle \alpha_- \tag{6.12}$$

Introducing small fluctuations (δ_x, δ_p, δ_{α_+}) of the form

$$x_j(t) = x_{j_0} + \delta x(t) \tag{6.13}$$

$$p_j(t) = p_{j_0} + \delta p(t) \tag{6.14}$$

$$\alpha_+(t) = \alpha_{+_0} + \delta\alpha_+(t) \tag{6.15}$$

where the steady states values are defined as

$$x_{j_0} = (0, 2\pi]$$
$$p_{j_0} = 0$$
$$\alpha_{+_0} = 0$$
$$\alpha_{-_0} = \alpha_-$$

and where $\delta x(t)$, $\delta p(t)$ and $\delta\alpha_+(t)$ are the fluctuations of the jth atoms position, momentum and the fluctuation of the probe field amplitude respectively. Note we have neglected the fluctuation of the pump field amplitude (α_-) as it can be shown that they do not play a role in the linear stability of the system.

Substituting (6.13) - (6.15) into equations (6.10 - 6.12) gives:

$$\frac{d\delta x_j}{dt} = \frac{\delta p_{j_0}}{m} \tag{6.16}$$
$$\frac{dp_j}{dt} = -2\hbar k i U_0 \left(\delta\alpha_+\alpha_-^* e^{2ikx_{j_0}} - \delta\alpha_+^*\alpha_- e^{-2ikx_{j_0}}\right) \tag{6.17}$$
$$\frac{d\delta\alpha_+}{dt} = \left(i\Delta_+ - iNU_0 - \beta\right)\delta\alpha_+ - 2kNU_0\left\langle \delta x e^{-2kix_{j_0}}\right\rangle \alpha_- \tag{6.18}$$

where $\langle e^{-ikx_{j_0}}\rangle = 0$ as the atoms are initially evenly distributed. We can rewrite equations (6.16) - (6.18) in terms of collective variables [67]

$$b = -2ik\left\langle \delta x e^{-2ikx_{j_0}}\right\rangle$$
$$P = \left\langle \delta p e^{-2ikx_{j_0}}\right\rangle$$

which greatly reduces the number of equations to be solved from $2N+1$ to 3:

$$\frac{db}{dt} = \frac{-2ik}{m}P \tag{6.19}$$

$$\frac{dP}{dt} = -2i\hbar k U_0 \delta\alpha_+ \alpha_-^* \tag{6.20}$$

$$\frac{d\delta\alpha_+}{dt} = \left(i\Delta_+ - iNU_0 - \beta\right)\delta\alpha_+ - iNU_0\ b\ \alpha_-. \tag{6.21}$$

If we now look for solutions of eqs. (6.19)-(6.21) with the form $b, P, \delta\alpha_+ \propto e^{\lambda t}$ then it can be shown that

$$\lambda b = \frac{-2ik}{m}P \tag{6.22}$$

$$\lambda P = -2i\hbar k U_0 \delta\alpha_+ \alpha_-^* \tag{6.23}$$

$$\lambda\delta\alpha_+ = \left(i\Delta_+ - iNU_0 - \beta\right)\delta\alpha_+ - iNU_0\ b\ \alpha_- \tag{6.24}$$

from which we can find b and P

$$P = \frac{-2i\hbar k U_0 \delta\alpha_+ \alpha_-^*}{\lambda}$$
$$b = \frac{-4\hbar k^2 U_0 \delta\alpha_+ \alpha_-^*}{m\ \lambda^2}$$

and hence obtain:

$$\lambda\delta\alpha_+ = \left(i\Delta_+ - iNU_0 - \beta\right)\delta\alpha_+ + \frac{4iN\hbar k^2 U_0^2 |\alpha_-|^2}{m\ \lambda^2}\delta\alpha_+$$
$$\left[\lambda^3 - \lambda^2\left(i\Delta_+ - iNU_0 - \beta\right) - \frac{4iN\hbar k^2 U_0^2|\alpha_-|^2}{m}\right]\delta\alpha_+ = 0$$
$$\lambda^3 - \lambda^2\left(i\Delta_+ - iNU_0 - \beta\right) - \frac{4iN\hbar k^2 U_0^2|\alpha_-|^2}{m} = 0. \tag{6.25}$$

Since the growth rate is simply defined as $g_r = Re(\lambda)$ we can compare the analytical result of the growth rate and the result obtained from numerical simulations of the CARL model equations (eqs. (6.4) and (6.7)) in absence of pump modulation $\alpha_m = 0$.

For the following parameters: $\Delta_+ = -0.3\kappa, U_0 = 1 \times 10^{-4}\kappa, |\alpha_-|^2 \approx 2 \times 10^5, m = 5 \times 10^4 \hbar k^2/\kappa$ substituted into eq. (6.25)

$$\lambda^3 + \lambda^2 (0.3i - 0.1i)\,\kappa - \frac{4i \cdot 1 \times 10^3 \cdot 1 \times 10^{-8}\kappa^2 \cdot 2 \times 10^5}{5 \times 10^4 \hbar k^2/\kappa} = 0$$

the result $Re(\lambda) = 0.0283\kappa$ was obtained. Since for $Re(\lambda) > 0$ required for instability this result clearly indicates a growth of α_+.

The behaviour of the growth rates as a function of detuning and pump intensity is shown in figures 6.3 and 6.4 respectively.

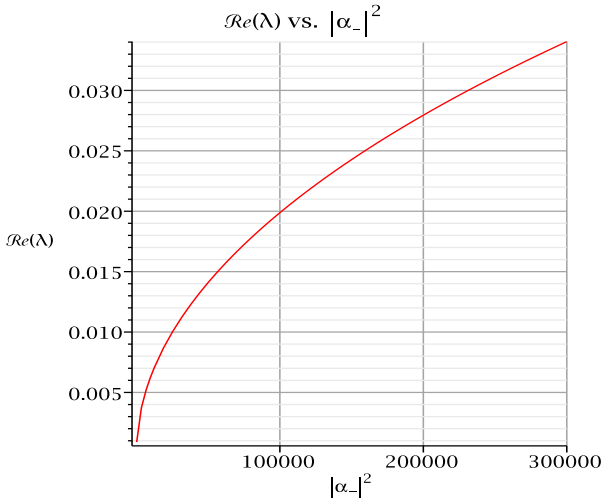

Figure 6.3: Growth rate as a function of the pump intensity obtained from the solution of eq. (6.25). The parameters used are: $N = 1000, \Delta_+ = -0.3\kappa, U_0 = 1 \times 10^{-4}\kappa, m = 5 \times 10^4 \hbar k^2/\kappa$

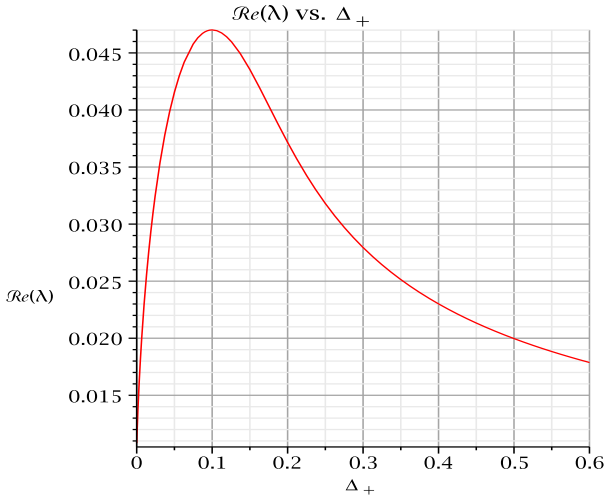

Figure 6.4: Growth rate as a function of the pump-cavity detuning obtained from the solution of eq. (6.25). The parameters used are: $N = 1000, U_0 = 1 \times 10^{-4}\kappa, |\alpha_-|^2 = 2 \times 10^5, m = 5 \times 10^4 \hbar k^2/\kappa$

As we looked for the solution of $\alpha_+ \propto e^{\lambda t}$ so for $|\alpha_+|^2 \propto e^{\lambda 2t}$ the growth rate of the probe intensity is finally $g_r \approx 0.056\kappa$. This result very well agrees with the value of $g_r \approx 0.055$ found numerically from the slope of the $|\alpha|^2$ as shown in fig. 6.5 obtained for the same parameters as used above in the analytical formula, eq. (6.25).

6.3 Frequency Modulation Regimes

The nature of the atom-field interaction in the model can be deduced by combining the Bessel function identity [68]:

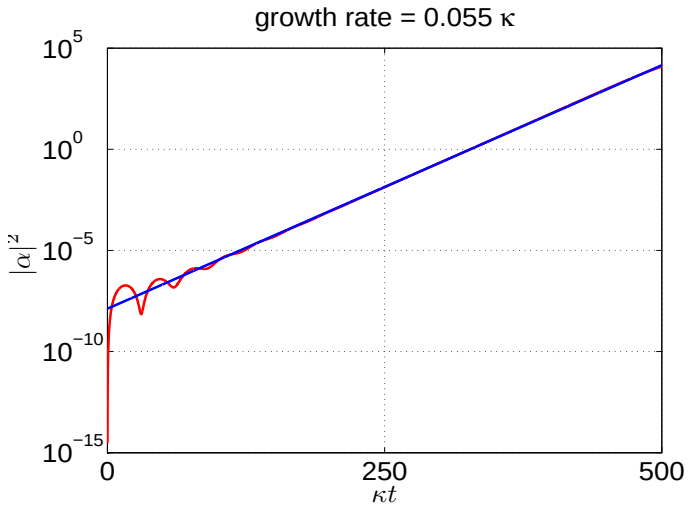

Figure 6.5: Growth rate of the probe field (α_+) obtained from the numerical simulation of eqs. (6.4) and (6.7) in the absence of pump modulation $\alpha_m = 0$. The parameters used are: $N = 1000, \eta_- = 450\kappa, \Delta_+ = -0.3\kappa, U_0 = 1 \times 10^{-4}\kappa, \mu = 5000\hbar k, m = 5 \times 10^4 \hbar k^2/\kappa$

$$exp(i\ z\ sin(\phi)) = \sum_{n=-\infty}^{\infty} J_n(z) e^{in\phi} \tag{6.26}$$

performing adiabatic elimination on eq. (6.7) gives

$$\begin{aligned} \alpha_- &= \frac{NiU_0\langle e^{2ikx}\rangle}{[i\Delta_{c_-} - NiU_0 - \kappa_-]} - \frac{1}{[i\Delta_{c_-} - NiU_0 - \kappa_-]}\eta_- e^{i\alpha_m sin(\Omega_m t)} \\ &= \frac{1}{[NiU_0 - \Delta_{c_-} + \kappa_-]}\eta_- e^{i\alpha_m sin(\Omega_m t)}. \end{aligned} \tag{6.27}$$

Substituting the expression eq. (6.27) into eq. (6.5) then the force on the jth atom can be written as

$$\frac{dp_j}{dt} = \frac{2\hbar k U_o i}{NiU_o - i\Delta_- + \kappa_-}\left[\alpha_+^* \eta_- e^{-i(2kx - \alpha_m sin(\Omega_m t))} - c.c\right], \tag{6.28}$$

which after applying (6.26) to (6.28) leads to the form:

$$\frac{dp_j}{dt} = \frac{2\hbar k U_o i}{N i U_o - i\Delta_- + \kappa_-} \left[\alpha_+^* \eta_- \sum_{n=-\infty}^{\infty} J_n(\alpha_m) e^{-i(2kx - n\Omega_m t)} - c.c \right]. \tag{6.29}$$

It can be seen from eq. (6.29) that the force acting on the atoms can be interpreted as an due to infinite number of optical potentials (n), each of which moves with a phase velocity that is proportional to an integer number of the modulation frequency $n\Omega_m$. These potentials can be consequently resonant with the atoms, if: $\frac{p_j}{m} \approx \frac{n\Omega_m}{2k}$, i.e. if the atomic velocity $\approx$ phase velocity of the nth optical potential.

Further inspection of eq. (6.29) shows that the width of each potential/resonance is proportional to $\propto \sqrt{|\alpha_+| J(\alpha_m)}$ while the separation,in frequency or phase velocity, between the resonances is proportional to Ω_m. It will be shown in what follows that the number of the potentials/resonances that interact with the atoms can significantly affect the atomic dynamics.

The behaviour of the system can be divided into three main regimes (fig. 6.6) depending on the value of the modulation frequency with respect to the collective recoil bandwidth (growth rate, g_r) i.e. the growth rate of the probe field in the absence of modulation: the high modulation frequency ($\Omega_m \gg g_r$), intermediate modulation frequency ($\Omega_m \approx g_r$) and low modulation frequency ($\Omega_m \ll g_r$). The growth rate of the probe field, g_r, can be found keeping $|\alpha_-|$ constant and setting $\kappa_+ = 0$, also assuming no phase modulation of the pump field.

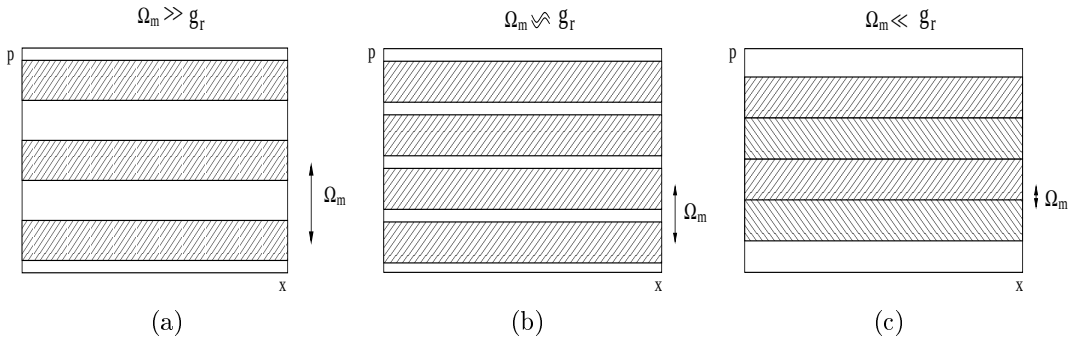

Figure 6.6: Schematic diagram showing the width and the separation of the potentials/resonances (shaded regions) for three frequency modulation regimes: (a) high frequency (b) intermediate frequency (c) low frequency. Here Ω_m is proportional to the separation of the potential/resonance while the width of the potential/resonance is proportional to: $\propto \sqrt{|\alpha_+| J(\alpha_m)}$

6.4 High Modulation Frequency ($\Omega_m \gg g_r$)

In the high frequency modulation regime the resonances are widely separated (fig. 6.6(a)) and it is possible to assume that the atoms interact with only one of the resonances. In the following example N=1000 particles with initial mean momentum $\mu = 5000\hbar k$ and momentum spread $\sigma = 0\hbar k$ have been uniformly distributed in phase space. Initially we set the pump field $\eta_- = 450\kappa$ and the probe-cavity detuning $\Delta_+ = -0.3\kappa$ (here and later the parameters given in the units of κ refer to the pump cavity decay rate κ_-).

For such initial parameters the characteristic growth rate/frequency was found to be $g_r = 0.055\kappa$, as shown in fig. 6.5 in section 6.2. Consequently we set the modulation frequency $\Omega_m = 0.55\kappa$ and the amplitude modulation $\alpha_m = 1$. It can be seen in fig. 6.7 that the intensity of the probe field $|\alpha_+^2|$ is amplified exponentially then oscillates after saturation, similar to the case of no pump modulation, section 6.2.

In turn the average momentum of the sample $\langle p \rangle$ and the momentum spread σ do not differ substantially from their initial values, as shown in

fig. 6.8, which shows histograms of the atomic momentum distribution at three

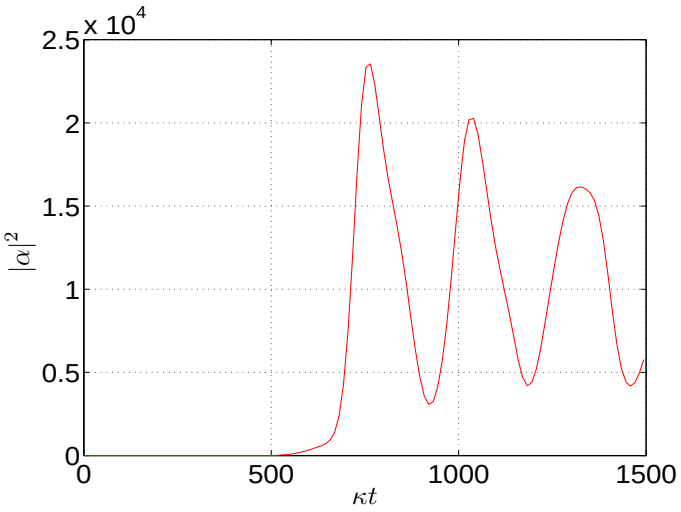

Figure 6.7: Time evolution of the probe intensity. The parameters used are: $N = 1 \times 10^3$, $\langle p_0 \rangle = 5000\hbar k$, $m = 50 \times 10^3 \hbar k^2/\kappa$, $\Delta_+ = -0.3\kappa$, $\eta = 450\kappa$, $U_0 = 0.0001\kappa$, $\Omega_m = 0.55\kappa$

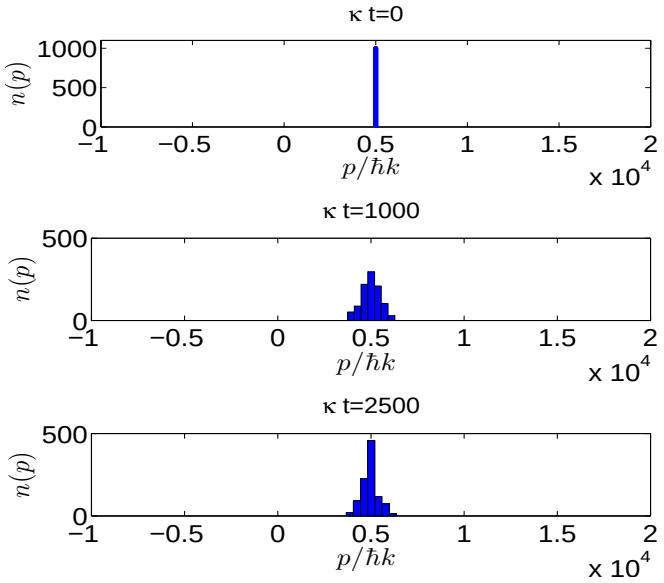

Figure 6.8: Histograms of the atomic momentum distribution for the high modulation frequency regime ($\Omega_m \gg g_r$) at κt=0, 1000, 2500. The parameters used are the same as in fig. 6.7

different times, and in figures (6.9 & 6.10) which show the time evolution of the average momentum and momentum spread respectively.

The general feature of the evolution of both the field intensity and the atomic dy-

namics are similar to those where the pump phase modulation is absent (section 6.2). The reason for this is that in both cases where high frequency pump modulation and no modulation occurs, the atom-field interaction involves only a single resonance. In the following sections it will be shown that changing the frequency of the phase modulation can introduce additional resonances into the atom-field interaction and dramatically alter the evolution of both the field intensity and the atomic dynamics.

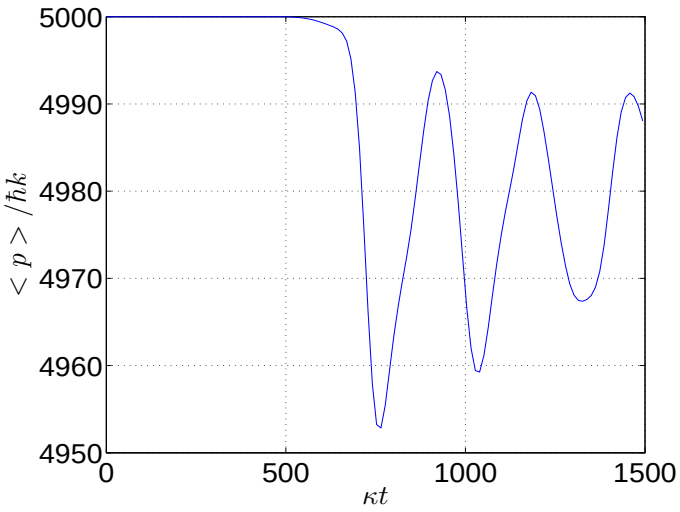

Figure 6.9: Time evolution of the average momentum in the high modulation frequency regime ($\Omega_m \gg g_r$). The parameters used are the same as in fig. 6.7

6.5 Intermediate Modulation Frequency ($\Omega_m \sim g_r$)

In the case of intermediate frequency modulation, ($\Omega_m \sim g_r$), the resonances are much closer to each other than in the high modulation frequency case as shown schematically in fig. 6.6(b). When the field is sufficiently amplified the width of the resonances ($\sim \sqrt{|\alpha_+|}$) increases and the resonances can overlap. Once the overlap takes place atoms diffuse chaotically within a large momentum range. The momentum range can be found using results from previous studies of the parametrically forced pendulum i.e. there are nonlinear resonances which occur when the phase

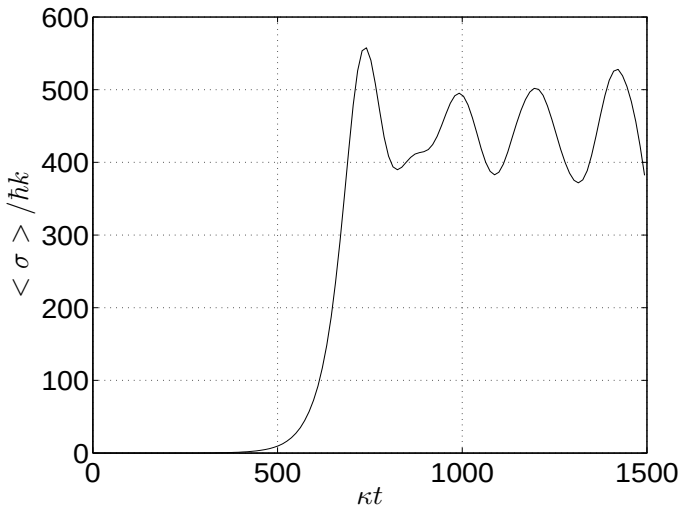

Figure 6.10: Time evolution of the momentum spread in the high modulation frequency regime ($\Omega_m \gg g_r$). The parameters used are the same as in fig. 6.7

term on the RHS of eq. (6.28) is stationary i.e. when

$$p/m + \alpha_m \Omega_m cos(\Omega_m t)/2k = 0 \tag{6.30}$$

It is known from studies of kicked rotors and pendula that these nonlinear resonances gives 'kicks' which tend to randomise the motion of the atoms leading to the diffusion of the atomic momenta [69]. In the case where the probe field is detuned from cavity resonance so that $\alpha_+ \propto e^{i\Delta_+ t}$ we can use eq. (6.30) to predict the velocity range within which the atom can diffuse:

$$\frac{-\Delta_+ - \alpha_m \Omega_m}{2k} \leq \frac{p}{m} \leq \frac{\alpha_m \Omega_m - \Delta_+}{2k}. \tag{6.31}$$

Assuming the atoms diffuse uniformly over the momentum space between these limits, the average momentum of the atoms will eventually be $\langle p \rangle = -\Delta_+ m/2k$. In

order to satisfy the intermediate frequency modulation condition ($\Omega_m \sim g_r$) we set $\Omega_m = 0.055\kappa$ and $\alpha_m = 10$. From eq. (6.31) and for the following initial parameters: $\langle p_0 \rangle = 5000\hbar k$, $\sigma = 0\hbar k$ and $m = 50000\hbar k^2/\kappa$ the predicted momentum diffusion range should be approximately: $-6000\hbar k \leq p \leq 20000\hbar k$.

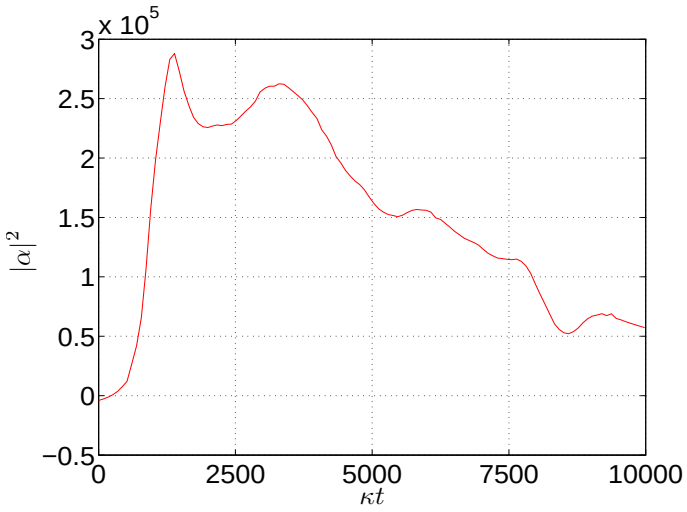

Figure 6.11: Time evolution of the probe intensity in the intermediate modulation frequency regime. The parameters used are: $N = 1 \times 10^3$, $\langle p_0 \rangle = 5000\hbar k$, $m = 50 \times 10^3 \hbar k^2/\kappa$, $\Delta_+ = -0.3\kappa$, $\eta = 450\kappa$, $U_0 = 0.0001\kappa$, $\Omega_m = 0.055\kappa$

Numerical results confirm this result and a similar momentum range can be found in the momentum distribution at $\kappa t = 10000$ shown in fig. 6.12. Since $\beta \approx 1 \times 10^{-5}$ is nonzero the probe intensity eventually decreases after being amplified as seen in fig. 6.11.

6.6 Low Modulation Frequency ($\Omega_m \ll g_r$)

In the case of low frequency modulation where ($\Omega_m \ll g_r$) the resonances are sufficiently close together (see schematic diagram, fig. 6.6(c)) that they can overlap even at the very early stages of the interaction.

Since many resonances are involved at the early stage of probe amplification the

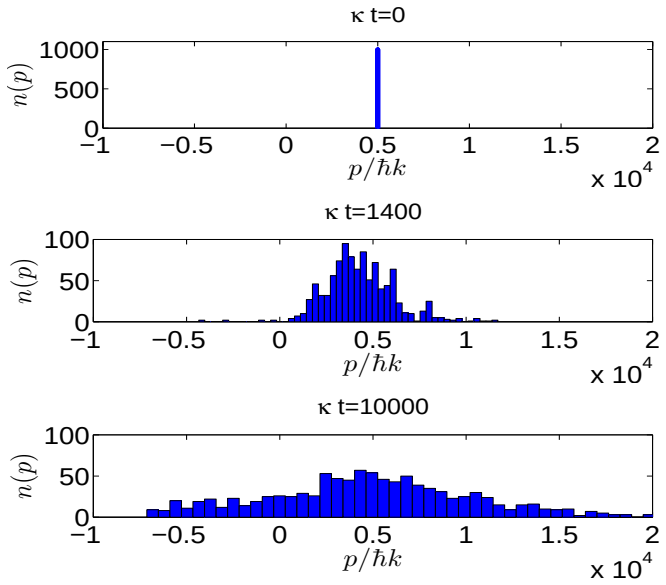

Figure 6.12: Histograms showing the evolution of the momentum distribution for the intermediate modulation frequency regime ($\Omega_m \sim g_r$) at κt=0, 1400, 10000. The parameters used are the same as in fig. 6.11

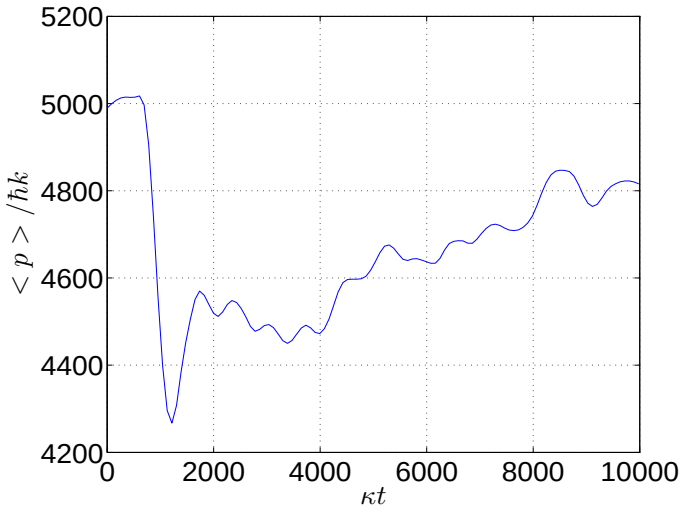

Figure 6.13: Time evolution of the average momentum in the intermediate modulation frequency regime ($\Omega_m \sim g_r$). The parameters used are the same as in fig. 6.11

atoms pass through successive resonances decreasing their momentum and consequently amplifying the probe field.

Similarly to eq. (6.30) the atom will be resonant with the ponderomotive force/potential

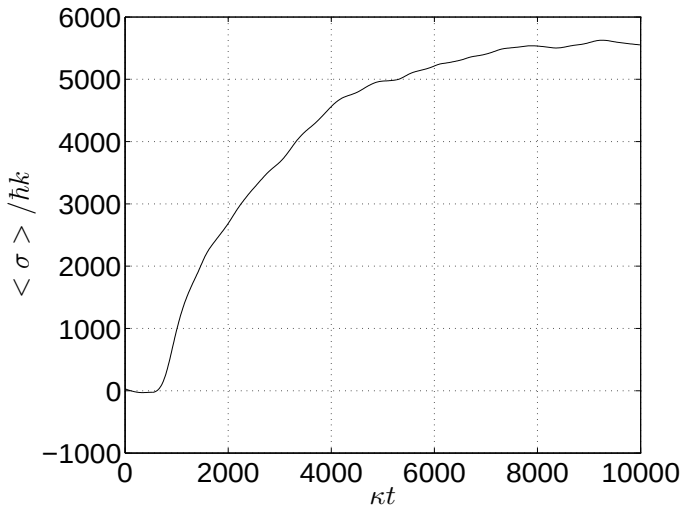

Figure 6.14: Time evolution of the momentum spread in the intermediate modulation frequency regime ($\Omega_m \sim g_r$). The parameters used are the same as in fig. 6.11

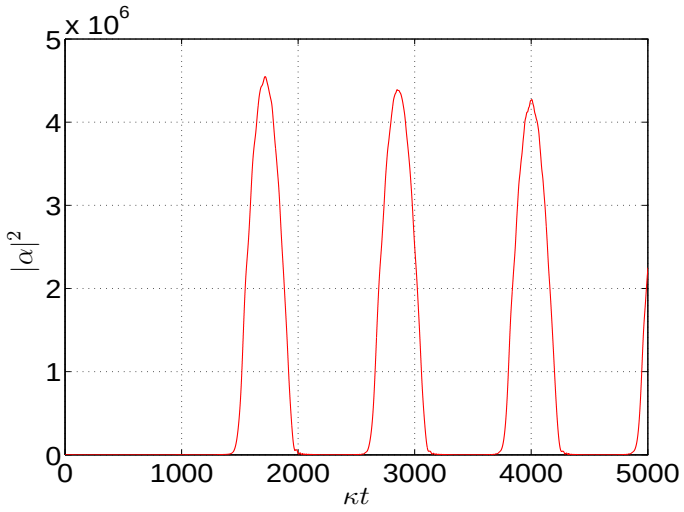

Figure 6.15: Time evolution of the probe intensity in the low modulation frequency regime ($\Omega_m \ll g_r$). Parameters used are: $N = 1 \times 10^3$, $\langle p_0 \rangle = 5000\hbar k$, $m = 50 \times 10^3 \hbar k^2/\kappa$, $\Delta_+ = -0.3\kappa$, $\eta = 450\kappa$, $U_0 = 0.0001\kappa$, $\Omega_m = 0.0055\kappa$

(i.e. experience a constant force) if:

$$p/m + (\alpha_m \Omega_m cos(\Omega_m t) + \Delta_+)/2k = 0. \tag{6.32}$$

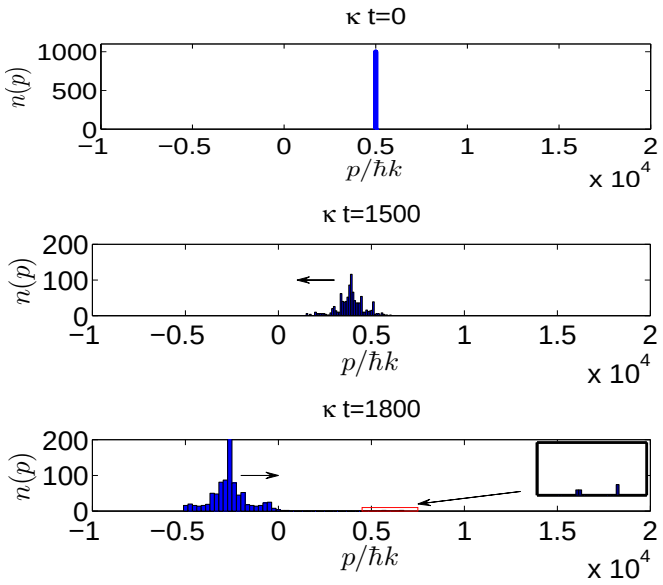

Figure 6.16: Histograms showing evolution of the atomic momentum distribution for the low modulation frequency regime ($\Omega_m \ll g_r$) at κt=0, 2700, 4000. The parameters used are the same as in fig. 6.15

We can assume, to a good approximation, that for sufficiently small β the system is Hamiltonian and obeys the constant of motion ($|\alpha_+^2| + \frac{N}{2\hbar k}\langle p\rangle \approx const.$). This implies that if the probe intensity $|\alpha|^2$ increases, resonance can be maintained only if we allow the atoms to decrease their momentum. For numerical simulation of the low modulation frequency regime we set $\Omega_m = 0.0055\kappa$ and $\alpha_m = 100$ with the other initial conditions unchanged. It can be seen in fig. 6.15 & fig. 6.16 that the increase of probe field intensity coincides with a decrease of the atomic momentum. During the whole interaction time the probe intensity and the average momentum oscillate periodically with a period of $2\pi/\Omega_m$ and from eq. (6.32) the lowest attainable momentum is predicted to be $p_{min} = -(\Delta_+ + \alpha_m\Omega_m)m/2k$. These predicted values of the oscillation period ($\approx 1100\kappa^{-1}$) and minimum attainable momentum ($\approx -6200\hbar k$) are confirmed by the results from the numerical simulations shown in fig. 6.16 & 6.17.

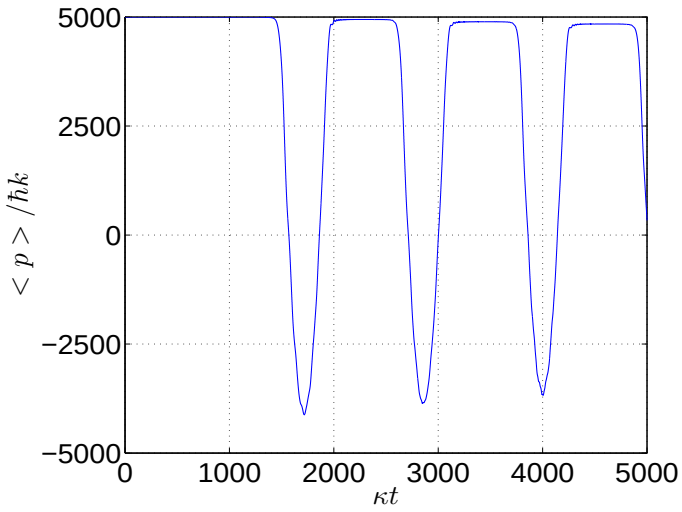

Figure 6.17: Time evolution of the average momentum for the low modulation frequency regime ($\Omega_m \ll g_r$). The parameters used are the same as in fig. 6.15

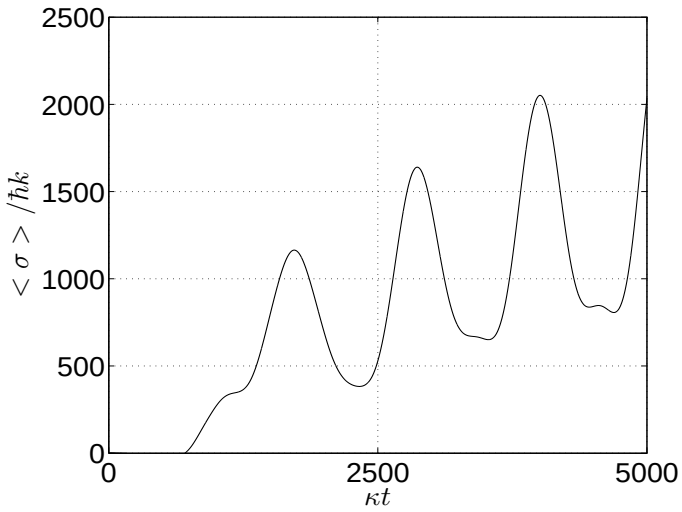

Figure 6.18: Time evolution of the momentum spread for the low modulation frequency regime ($\Omega_m \ll g_r$). The parameters used are the same as in fig. 6.15

It is important to notice that during the process atoms separate into two distinctive groups. The first group contains the atoms that do not exchange energy with the field and remains approximately at its initial momentum (fig. 6.16, $\kappa t = 4000$). The other group oscillates in momentum, moving from the top to bottom of the attainable phase space.

6.6.1 Slowing a Beam of Cold Atoms

Comparison of the three frequency modulation regimes indicates that the low frequency modulation to be the most useful for the purpose of slowing atomic beams.

Although both the intermediate and the low frequency modulation regimes allow a large decrease in the average atomic momentum to be produced, the intermediate frequency modulation regime produces diffusive momentum spread growth, which is generally undesirable for applications. In contrast, the low modulation frequency regime produces a large decrease in average atomic momentum while maintaining a relatively narrow momentum distribution for substantial fraction of the atomic ensemble.

As shown in fig. 6.17 the initial average momentum of the atoms can be decreased to the minimum attainable value ($p_{min} = -(\Delta_+ + \alpha_m\Omega_m)m/2k$), after which the atoms are again accelerated and along with the probe field intensity oscillate with period $2\pi/\Omega_m$. Here we can show that the final value of the minimum momentum is also a function of the parameter β which as explained earlier describes the ratio of the probe (κ_+) and the pump (κ_-) cavity decay ($\beta = \frac{\kappa_+}{\kappa_-}$). To maintain the oscillations of the probe field and the average atomic momentum, β has to be sufficiently small, otherwise the high cavity decay rate will prevent the field being amplified repeatedly. However, for the purpose of slowing beams of atoms this does not have to be fulfilled and a single oscillation of the average momentum will suffice to slow the atoms. Fig. 6.19 presents the minimum average momentum obtained within, single oscillation, for different values of β.

It can be seen in fig. 6.19 for a case where the initial atomic momentum $p_0 = 5000\hbar k$ that for $\beta \sim 0.06$ the initial average momentum of atoms was decreased to zero and for $\beta < 0.06$ the direction of the atomic beam was reversed ($\langle p_{min} \rangle < 0$).

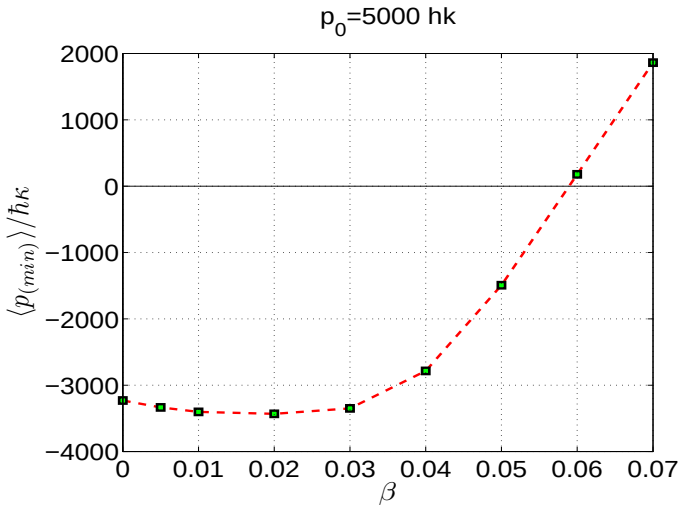

Figure 6.19: Minimum average momentum vs β. The parameters used are: $N = 1 \times 10^3$, $\langle p_0 \rangle = 5000\hbar k$, $m = 50 \times 10^3 \hbar k^2/\kappa$, $\Delta_+ = -0.3\kappa$, $\eta = 450\kappa$, $U_0 = 0.0001\kappa$, $\Omega_m = 0.0055\kappa$

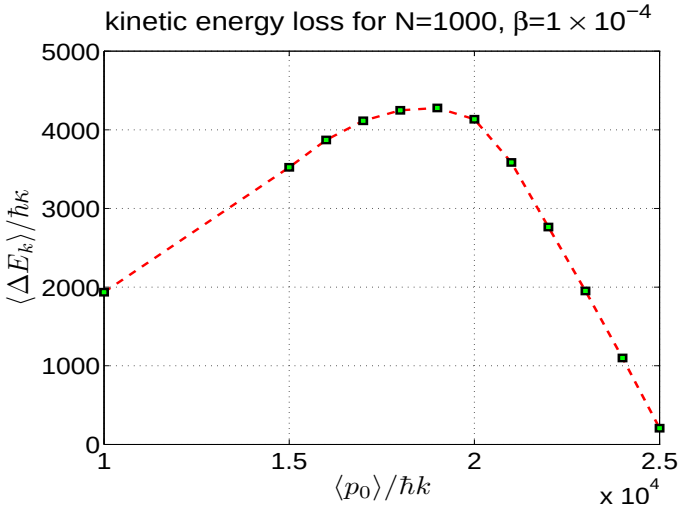

Figure 6.20: Kinetic energy loss vs $\langle p_0 \rangle$ for the low frequency modulation regime. The parameters used are: $N = 1 \times 10^3$, $\beta = 1 \times 10^{-3}$, $m = 50 \times 10^3 \hbar k^2/\kappa$, $\Delta_+ = -0.3\kappa$, $\eta = 450\kappa$, $U_0 = 0.0001\kappa$, $\Omega_m = 0.0055\kappa$

Figure 6.20 shows the total kinetic energy loss vs. initial average momentum of the atoms for fixed $\beta = 1 \times 10^{-3}$. Intuitively for larger values of initial values of $\langle p_0 \rangle$ one would expect the efficiency of slowing to decrease.

However as can be seen in fig. 6.20 the kinetic energy loss can be larger for higher

initial momentum. This is due to the fact that, as mentioned before, the system has a rather well defined minimum attainable momentum ($p_{min} = -(\Delta_+ + \alpha_m \Omega_m)m/2k$) which can be unchanged for a certain range of initial average momenta. For that reason the $\langle p_0 \rangle$ can be increased until the maximum efficiency of the slowing can be reached. When $\langle p_0 \rangle$ exceeds the optimum value ($\sim$ 18000 here), the efficiency decreases and eventually when $\langle p_0 \rangle$ becomes too large no slowing can be seen.

6.6.2 Slowing a Beam of Atoms with Finite Temperature

In the proceeding section it has been assumed that the atomic beam has been initially cold, with zero momentum spread, i.e. zero temperature. For the case of a beam of atoms with finite temperature the system preserves all the features that were observed for the low frequency modulation regime. In addition adjusting the probe-cavity frequency detuning (Δ_+) and probe-pump cavity loss ratio (β) it is possible to obtain even better control over the atomic dynamics. In the following example the low frequency modulation regime is used to slow a group of $N = 2000$ atoms with initial average momentum $\langle p_0 \rangle = 5000\hbar k$ and momentum spread $\sigma_0 = 500\hbar k$. In order to avoid many oscillations of the field and the momentum $\beta \approx 2 \times 10^{-4}$ is chosen. This allows only single amplification of the probe intensity to be produced, as shown in fig. 6.21.

Fig. 6.22 shows that, fast and hot atoms split into two groups. First, a smaller fraction of the total ensemble does not exchange energy with the field and remains at approximately the initial momentum. The other, significantly larger group, after reaching the minimum attainable momentum, i.e. $p_{min} \approx -6000\hbar k$, increases its momentum and stops at $\langle p \rangle = 0$ as shown in fig. 6.23.

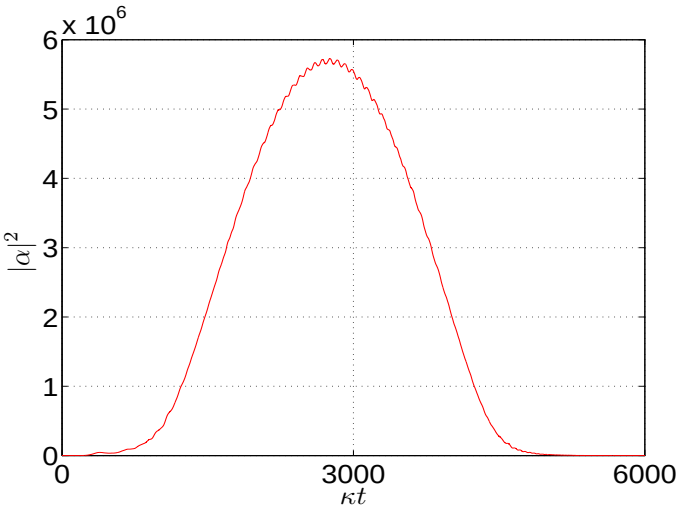

Figure 6.21: Time evolution of the probe intensity for a beam of initial finite temperature. The parameters used are: $N = 2 \times 10^3$, $\langle p_0 \rangle = 5000\hbar k$, $\sigma_0 = 500\hbar k$, $m = 60 \times 10^3 \hbar k^2/\kappa$, $\eta = 550\kappa$, $U_0 = 0.00005\kappa$

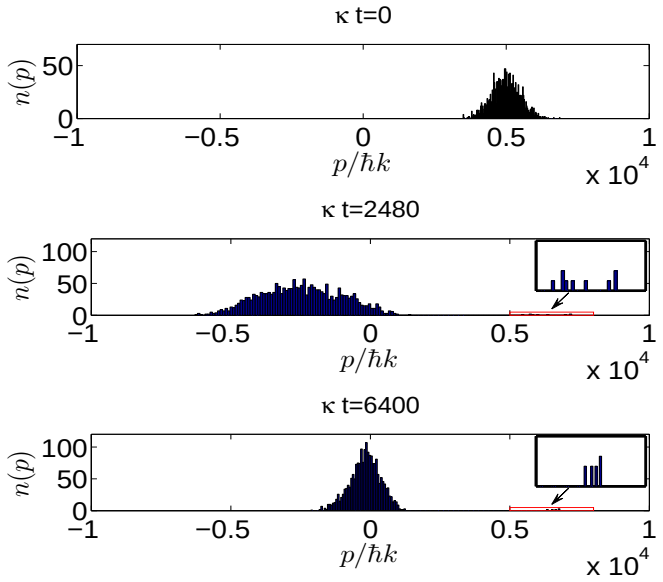

Figure 6.22: Histograms showing evolution of the momentum distribution, ($\Omega_m \ll g_r$), for a beam of finite temperature initially, at κt=0, 2400, 6400 (note the atoms separate into two distinctive groups). The parameters used are the same as in fig. 6.21

Even though, at some particular time of the interaction (e.g. $\kappa t \sim 2400$, in fig. 6.22), the momentum spread of the larger group increases (as in the case of the beam of

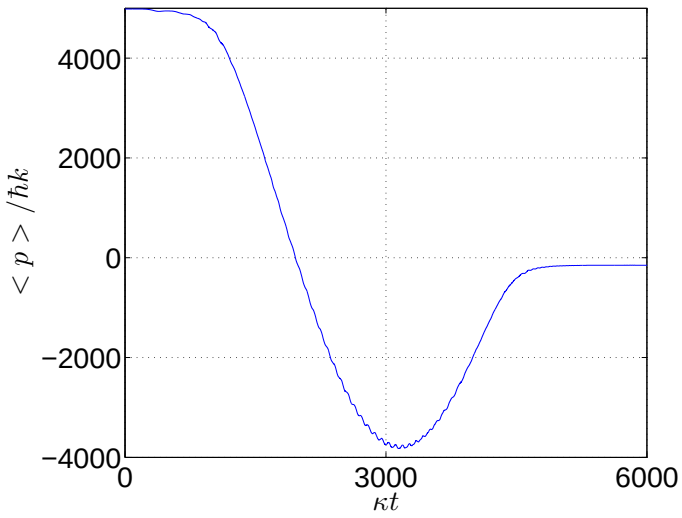

Figure 6.23: Time evolution of the average momentum, ($\Omega_m \ll g_r$) for a beam of finite temperature initially. The parameters used are the same as in fig. 6.21

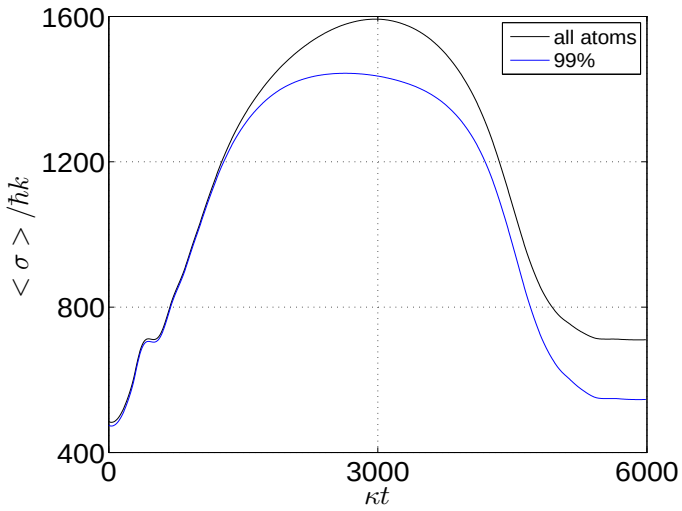

Figure 6.24: Time evolution of the momentum spread of the two separate groups of atoms (cf fig. 6.22). The parameters used are the same as in fig. 6.21

cold atoms) and the final momentum distribution of the atoms ($\kappa t \sim 6400$) is approximately equal to its initial value before any interaction took place. Hence slowing a beam of 'hot' atoms without introducing additional heating has been demonstrated [70].

Chapter 7

Conclusions

7.1 Summary

Results from studies of atoms confined in a Fabry-Perot cavity indicate two different behaviours of the atom-field interaction depending on the direction of the pump field with respect to the cavity axis. For the case of a pump field being sent directly through one of the cavity mirrors (here called the cavity-pump case) one can observe almost instantaneous growth of the cavity field and strong interaction with the confined atoms. Slowing and cooling of the sample can be clearly seen, however, closer inspection confirms a linear increase of the cooling time with atom number, which as pointed out in previous works [39] makes such systems rather impractical for very large ensembles. Significantly different behaviour can be observed for the case when the pump field is directed perpendicular to the cavity axis and hence the atoms are illuminated directly by the light field (here called the atom-pump case). Contrary to the cavity-pump configuration the atom-pump configuration needs the presence of particles to populate the cavity mode via scattering. For sufficiently strong fields, and large atomic ensembles, one can observe self-ordering of the particles which can lead to fast localisation and cooling of the atoms. As has been shown chapter 3 for given parameters the cooling rate can in fact increase with the number of atoms in the cavity.

As the number of atoms plays an important role in numerical simulations of the particle models the equivalent Vlasov model has also been presented. The results from simulation of the Vlasov models for both the cavity-pump and the atom-pump models show excellent agreement with their particle counterparts. However, the advantage of the Vlasov model over the particle model relies in the fact that the numerical effort can be greatly reduced for simulations involving large atomic ensembles.

Whereas chapter 2 and 3 considered classical models of atom-cavity interactions, chapters 4 and 5 described semi-classical models of both the cavity-pump and the atom-pump configurations. These semi-classical models show very good agreement with the classical models in the limit where atomic excitation is negligible. As expected from the analytical examination of the semi-classical equations the numerical simulations show an improving agreement between the semi-classical and classical models as the pump-atom detuning is increased. Furthermore semi-classical models of the cavity-pump and the atom-pump case reveal relatively fast cooling of atoms for blue detuned light compared to red detuned light.

Results from study of atoms confined in the ring cavity pumped by the phase modulated light show the presence of three different regimes in which both the field and the atoms reveal qualitatively different behaviour. This behaviour depends on the number of resonances that atoms can interact with and three cases can be distinguished: single resonance (high modulation frequency) and the multi resonances which can overlap due to growth of the probe intensity (intermediate modulation frequency) or when the resonances are sufficiently close to each other (low modulation frequency). As has been shown, the low frequency modulation regime gives an opportunity to control the dynamics of the atomic ensemble and can eventually lead to effective slowing of the atomic beam. Moreover the slowing of a beam of

hot atoms using the low frequency modulation regime does not introduce further heating to the atoms.

7.2 Future Work

All of the cavity cooling models presented in this work could be the subject of further work. One obvious topic for future studies could be the extension of the models described in chapters 2 - 5 from 1 to 2 or even 3 dimensions and using a variety of pumping geometries and cavity geometries. Although the computation time associated with such models is prohibitive at present, the rapid development of computing hardware and parallel programming techniques may make them feasible within a few years.

Another extension to the work described here is the modelling of a quantum gas e.q. Bose-Einstein condensate (BEC) or a Fermi gas. Although these systems are not of interest for cooling, they offer the possibility to study new regimes of light-matter interactions, and could be used as an analogue for several condensed matter systems involving quantum degenerate matter interacting with spatially periodic potentials.

The work described in chapter 6 involving ring cavities and phase-modulated pumping offers the possibility of new methods for slowing and cooling atoms. An obvious area for future studies would be to investigate different types of modulation e.g. amplitude modulation, combined amplitude/phase modulation, non-sinusoidal modulation as is performed in so-called "optical ratchets" [71, 72, 73] and deduce the optimum type of modulation for efficient atomic cooling and slowing.

Appendix A

Numerical Methods for Solving the Vlasov Model (sec. 2.4)

The Crank-Nicolson scheme is based on the Finite Difference Method for solving partial differential equations. It is an implicit method which means that to obtain the "next" value of a function in time a system of algebraic equation must be solved.

This method can be explained using an example of a simple partial differential equation of the form:

$$\frac{\partial u}{\partial t} = c\frac{\partial u}{\partial x} \tag{A.1}$$

Eq. (A.1) can be discretized using the Crank-Nicolson scheme such that:

$$\left(\frac{\partial u}{\partial x}\right)_i^{j+\frac{1}{2}} = \frac{1}{2}\left[\left(\frac{\partial u}{\partial x}\right)_i^{j+1} + \left(\frac{\partial u}{\partial x}\right)_i^{j}\right] = \frac{1}{2}\left[\left(\frac{u_{i+1}^{j+1} - u_{i-1}^{j+1}}{2\Delta x}\right) + \left(\frac{u_{i+1}^{j} - u_{i-1}^{j}}{2\Delta x}\right)\right] \tag{A.2}$$

$$\left(\frac{\partial u}{\partial t}\right)_i^{j+\frac{1}{2}} = \left(\frac{u_i^{j+1} - u_i^{j}}{\Delta t}\right) \tag{A.3}$$

where the subscript i corresponds to space and j corresponds to time and Δx and Δt are the space and the time step size respectively, as shown on the stencil presented in the fig. A.1

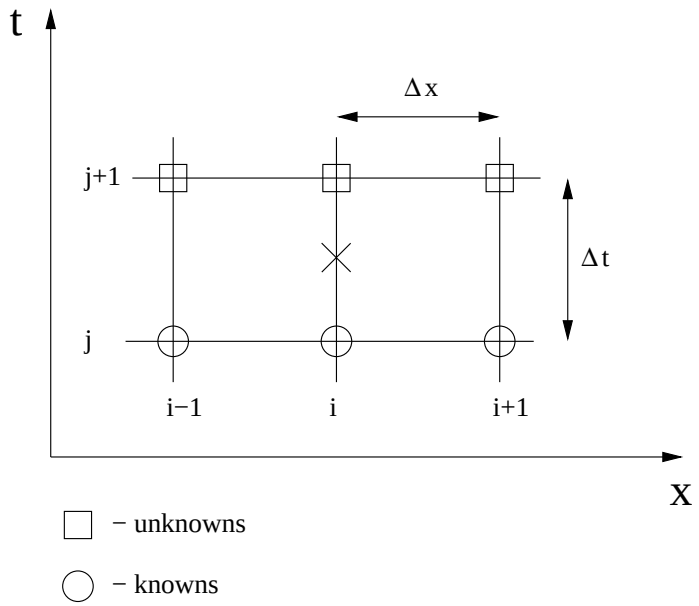

Figure A.1: The Crank-Nicolson stencil for a 1D problem

Hence eq. (A.1) can be written as:

$$\frac{1}{4\Delta x}\left[u_{i+1}^{j+1}-u_{i-1}^{j+1}+u_{i+1}^{j}-u_{i-1}^{j}\right]=\frac{1}{\Delta t}\left[u_{i}^{j+1}-u_{i}^{j}\right]. \tag{A.4}$$

This scheme can be similarly applied to the Vlasov model (eqs (2.50) - (2.51), section 2.4).

$$\frac{\partial \bar{f}_n}{\partial \bar{t}}=-in\bar{\omega}_r\bar{p}\bar{f}_n+\frac{i}{2}\bar{U}_0|\alpha|^2\left(\frac{\partial \bar{f}_{n-1}}{\partial \bar{p}}-\frac{\partial \bar{f}_{n+1}}{\partial \bar{p}}\right) \tag{A.5}$$

$$\frac{d\alpha}{d\bar{t}}=\left(-1+i\bar{\Delta}_c-\frac{N\bar{\gamma}_0}{2}-i\frac{N\bar{U}_0}{2}\right)\alpha-\frac{N(\bar{\gamma}_0+i\bar{U}_0)}{4}\int_{-\infty}^{\infty}\left(\bar{f}_{-1}+\bar{f}_1\right)\,d\bar{p}\,\alpha+\bar{\eta} \tag{A.6}$$

Using the Crank-Nicolson discretisation of eq. (A.5) one obtains:

$$(LHS):\ f(n)_i^{j+1}-\frac{i}{8}\bar{U}_0|\alpha|^2\frac{\Delta t}{\Delta p}\Bigg\{\left[f(n-1)_{i+1}^{j+1}-f(n-1)_{i-1}^{j+1}\right] -\left[f(n+1)_{i+1}^{j+1}-f(n+1)_{i-1}^{j+1}\right]\Bigg\} \tag{A.7}$$

and

$$(RHS):\ (1-in\omega_r p_i\Delta t)f(n)_i^{j}+\frac{i}{8}\bar{U}_0|\alpha|^2\frac{\Delta t}{\Delta p}\Bigg\{\left[f(n-1)_{i+1}^{j}-f(n-1)_{i-1}^{j}\right] -\left[f(n+1)_{i+1}^{j}-f(n+1)_{i-1}^{j}\right]\Bigg\} \tag{A.8}$$

where the "new" elements $(j+1)$ and "old" elements (j) have been separated on the LHS and the RHS respectively. Obviously in eqs. (A.7 and A.8) the subscript i corresponds to momentum space.

Similarly the field equation, eq. (A.6) can be written as

$$\alpha^{j+1} = \left\{ \left(-1 + i\bar{\Delta}_c - \frac{N\bar{\gamma}_0}{2} - i\frac{N\bar{U}_0}{2} \right) \alpha^j - \frac{N}{4} \left(\bar{\gamma}_0 + i\bar{\Delta}_0 \right) \times \int_{-\infty}^{\infty} \left[f(-1) + f(1) \right] \right\} \Delta t + \alpha^j. \tag{A.9}$$

Equations (A.7, A.8 and A.9) together make a closed set of evolution equations. In this form eqs. (A.7, A.8 and A.9) can be easily implemented in a numerical code and solved using one of many available methods for solving linear system of equations, e.g. LAPACK [74]

Appendix B

List of Publications

This appendix contains publications which have arisen from the work described in this thesis. These publications are:

- T. Griesser, H. Ritsch, M. Hemmerling and G.R.M. Robb, *" A Vlasov approach to bunching and selfordering of particles in optical resonators "*, Eur. Phys. J. D **58**, 349-368 (2010)
- M. Hemmerling and G.R.M. Robb, *" Slowing atoms using optical cavities pumped by phase-modulated light "*, Phys. Rev. A **82**, 053420 (2010)

Bibliography

[1] James Clerk Maxwell. *A treatise on electricity and magnetism [microform] / by James Clerk Maxwell.* Clarendon Press, Oxford :, 1873.

[2] R. Frisch. Experimenteller Nachweis des Einsteinschen Strahlungsrückstoßes. *Z. Phys.* ***86****, 42*, 1933.

[3] G. A. Askar'yan. Vozdiestvie gradienta polya intensivnogo electromagnitnogo lucha na electroni i atomi. *Zh. Eksp. Teor. Fiz. 42, 1567–1570[Sov. Phys. JETP 15, 1088]*, 1962.

[4] G. A. Letokhov. Narrowing of the Doppler width in a standing light wave. *Pisma Zh. Eksp. Teor. Fiz. 7, 348*, 1968.

[5] A. Ashkin. Acceleration and trapping of particles by radiation pressure. *Phys. Rev. Lett.*, 24(4):156–159, Jan 1970.

[6] T. Hansch and A. Schawlow. Cooling of gases by laser radiation. *Optics Communications*, 13(1):68–69, January 1975.

[7] P. Ehrenfest. Bemerkung über die angenäherte Gültigkeit der klassischen mechanik innerhalb der quantenmechanik. *Zeitschrift für Physik A Hadrons and Nuclei*, 45:455–457, 1927. 10.1007/BF01329203.

[8] Erich Joos. Ehrenfest theorems. In Daniel Greenberger, Klaus Hentschel, and Friedel Weinert, editors, *Compendium of Quantum Physics*, pages 180–182. Springer Berlin Heidelberg, 2009.

[9] Brian Harald Bransden and Charles Jean Joachain. *Physics of Atoms and Molecules; 2nd ed.* Prentice-Hall, Harlow, 2003.

[10] Harold J. Metcalf and Peter van der Straten. *Laser Cooling and Trapping.* Springer, November 2001. http://www.worldcat.org/isbn/0387987282.

[11] A. Ashkin. Applications of Laser Radiation Pressure. *Science*, 210(4474):1081–1088, 1980.

[12] J. D. Thompson, B. M. Zwickl, A. M. Jayich, Florian Marquardt, S. M. Girvin, and J. G. E. Harris. Strong dispersive coupling of a high-finesse cavity to a micromechanical membrane. *Nature*, 452(7183):72–75, March 2008.

[13] J.P. Gordon and A. Ashkin. Motion of atoms in a radiation trap. *Physical Review A **21**, No.5*, (1980).

[14] Steven Chu. Laser Manipulation of Atoms and Particles. *Science*, 253(5022):861–866, 1991.

[15] A. Ashkin and J. M. Dziedzic. Optical trapping and manipulation of viruses and bacteria. *Science*, 235(4795):1517–1520, March 1987.

[16] A Ashkin. Optical trapping and manipulation of neutral particles using lasers. 94(10):4853, 1997.

[17] W D Phillips, P D Lett, S L Rolston, C E Tanner, R N Watts, C I Westbrook, C Salomon, J Dalibard, A Clairon, and S Guellati. Optical molasses: The coldest atoms ever. *Physica Scripta*, 1991(T34):20, 1991.

[18] P.D. Lett, W.D. Phillips, S.L. Rolson, C.E. Tanner, R.N. Watts, and C.I.Westbrook. Optical molasses. *J. Opt. Soc. Am. B/Vol. **6** No. 11*, (1989).

[19] D. William Phillips. Nobel lecture: Laser cooling and trapping of neutral atoms. *Rev. Mod. Phys.*, 70(3):721–741, Jul 1998.

[20] C. Cohen-Tannoudji. *Fundamental Systems in Quantum Optics.* Proceedings of the Les Houches Summer School. Session LIII, edited by J. Dalibard, J.-M. Raimond, and J. Zinn-Justin (North-Holland, Amsterdam, 1992, pp. 1-164).

[21] J. Dalibard and C. Cohen-Tannoudji. Laser cooling and trapping of neutral atoms.

[22] C. S. Adams and E. Riis. Laser cooling and trapping of neutral atoms. *Progress in Quantum Electronics*, 21(1):1 – 79, 1997.

[23] C. Cohen-Tannoudji and J. Dalibard. Manipulating atoms with photons.

[24] Nir Friedman, Ariel Kaplan, and Nir Davidson. Dark optical traps for cold atoms. volume 48 of *Advances In Atomic, Molecular, and Optical Physics*, pages 99 – 151. Academic Press, 2002.

[25] Gabriel Spalding Kishan Dholakia, Michael MacDonald. Optical tweezers: the next generation. *Physics World*, **15**:31–35, October 2002.

[26] M. Gangl, P. Horak, and H. Ritsch. Cooling neutral particles in multimode cavities without spontaneous emission. *Journal of Modern Optics*, 47:2741–2753, November 2000.

[27] P. Maunz, T. Puppe, I. Schuster, N. Syassen, P. W. H. Pinkse, and G. Rempe. Cavity cooling of a single atom. *Nature*, (6978):50–52, March.

[28] Almut Beige, Peter L Knight, and Giuseppe Vitiello. Cooling many particles at once. *New Journal of Physics*, 7(1):96, 2005.

[29] Steven Chu. Nobel lecture: The manipulation of neutral particles. *Rev. Mod. Phys.*, 70(3):685–706, Jul 1998.

[30] J. Dalibard and C. Cohen-Tannoudji. Dressed-atom approach to atomic motion in laser light: the dipole force revisited. *J. Opt. Soc. Am. B*, 2(11):1707–1720, 1985.

[31] Claude Cohen-Tannoudji, Jacques Dupont-Roc, and Gilbert Grynberg. *Atom—Photon Interactions: Basic Processes and Applications*. Wiley-Interscience, March 1992.

[32] A. Aspect, J. Dalibard, A. Heidmann, C. Salomon, and C. Cohen-Tannoudji. Cooling atoms with stimulated emission. *Phys. Rev. Lett.*, 57(14):1688–1691, Oct 1986.

[33] D. J. Wineland, J. Dalibard, and C. Cohen-Tannoudji. Sisyphus cooling of a bound atom. *J. Opt. Soc. Am. B*, 9(1):32–42, 1992.

[34] Peter Horak, Gerald Hechenblaikner, Klaus M. Gheri, Herwig Stecher, and Helmut Ritsch. Cavity-induced atom cooling in the strong coupling regime. *Phys. Rev. Lett.*, 79(25):4974–4977, Dec 1997.

[35] Gerald Hechenblaikner, Markus Gangl, Peter Horak, and Helmut Ritsch. Cooling an atom in a weakly driven high-Q cavity. *Phys. Rev. A*, 58(4):3030–3042, Oct 1998.

[36] Vladan Vuletić and Steven Chu. Laser cooling of atoms, ions, or molecules by coherent scattering. *Phys. Rev. Lett.*, 84(17):3787–3790, Apr 2000.

[37] Peter Domokos and Helmut Ritsch. Mechanical effects of light in optical resonators. *J. Opt. Soc. Am. B*, 20(5):1098–1130, 2003.

[38] P. Pinkse and G. Rempe. Single atoms moving in a high-finesse cavity. *Reprint of Chapter 13 of Cavity-Enhanced Spectroscopies, Vol.40, pages: 255-295*, (2002).

[39] Peter Domokos and Helmut Ritsch. Collective cooling and self-organization of atoms in a cavity. *Phys. Rev. Lett.*, 89(25):253003, Dec 2002.

[40] Adam T. Black Hilton W. Chan and Vladan Vuletic. Observation of collective-emission-induced cooling of atoms in an optical cavity. *Physical Review Letters **90**, No.6*, (2003).

[41] Adam T. Black, James K. Thompson, and Vladan Vuletić. Collective light forces on atoms in resonators. *Journal of Physics B: Atomic, Molecular and Optical Physics*, 38(9):S605+, May 2005.

[42] Adam T Black, Hilton W.Chan, Vladan Vuletic. Self-organization of atomic samples in resonators and collective light forces. *World Scientific Publishing Co. Pte. Ltd*, 2003.

[43] Adam T Black. *Collective atom-light interactions applied to laser cooling and quantum communications*. PhD dissertation, Umi Number: 3186329, 2005.

[44] Daniel A. Steck. Cesium D line data. http://steck.us/alkalidata/cesiumnumbers.1.6.pdf.

[45] Markus Gangl and Helmut Ritsch. Collective dynamical cooling of neutral particles in a high-Q optical cavity. *Phys. Rev. A*, 61(1):011402, Dec 1999.

[46] Peter Horak and Helmut Ritsch. Scaling properties of cavity-enhanced atom cooling. *Phys. Rev. A **64**, 033422*, (2001).

[47] Peter Domokos, Peter Horak and Helmut Ritsch. Semiclassical theory of cavity-assisted atom cooling. *Journal of Physics B: Atomic, Molecular and Optical Physics **34**, 187-198*, (2001).

[48] Weiping Lu and P.F. Barker Yongkai Zhao. Cooling molecules in optical cavities. *Physical Review A **76**, 013417*, (2007).

[49] A. Vukics and P. Domokos. Simultaneus cooling and trapping of atoms by a single cavity-field mode. *Physical Review A* ***72****, 031401*, (2005).

[50] Rebecca L. Honeycutt. Stochastic runge-kutta algorithms. I. white noise. *Phys. Rev. A*, 45(2):600–603, Jan 1992.

[51] M. Januszewski and M. Kostur. Accelerating numerical solution of stochastic differential equations with CUDA. *Computer Physics Communications*, 181(1):183 – 188, 2010.

[52] A. A. Vlasov. The vibrational properties of an electron gas. *Physics-Uspekhi*, 10(6):721–733, 1968.

[53] T. Griesser, H. Ritsch, M. Hemmerling, and G.R.M. Robb. A vlasov approach to bunching and selfordering of particles in optical resonators. *The European Physical Journal D - Atomic, Molecular, Optical and Plasma Physics*, 58:349–368, 2010.

[54] William H. Press, Saul A. Teukolsky, William T. Vetterling, and Brian P. Flannery. *Numerical recipes in Fortran 90 (2nd ed.): the art of parallel scientific computing*. Cambridge University Press, New York, NY, USA, 1996.

[55] H. Ritsch J.K. Asbóth, P. Domokos and A. Vukics. Self-organization of atoms in a cavity field: Threshold, bistability, and scaling laws. *Physical Review A* ***72****, 053417*, (2005).

[56] Lin Zhang, G J Yang, and L X Xia. Self-organization effects and light amplification of collective atomic recoil motion in a harmonic trap. *Journal of Optics B: Quantum and Semiclassical Optics*, 7(11):355, 2005.

[57] Peter W. Milloni, Joseph H. Eberly. *Lasers*. John Wiley and Sons, (1988).

[58] R. Bonifacio and L. De Salvo. Collective atomic recoil laser (carl) optical gain without inversion by collective atomic recoil and self-bunching of two-level atoms. *Nuclear Instruments and Methods in Physics Research Section A: Accelerators, Spectrometers, Detectors and Associated Equipment*, 341(1-3):360 – 362, 1994.

[59] R. Bonifacio, G. R. M. Robb, and B. W. J. McNeil. Propagation, cavity, and doppler-broadening effects in the collective atomic recoil laser. *Phys. Rev. A*, 56(1):912–924, Jul 1997.

[60] G. R. M. Robb, R. T. L. Burgess, and W. J. Firth. Enhancement of collective atomic recoil lasing due to pump phase modulation. *Phys. Rev. A*, 78(4):041804, Oct 2008.

[61] M. Cashen, O. Rivoire, V. Romanenko, L. Yatsenko, and H. Metcalf. Strong optical forces in frequency-modulated light. *Phys. Rev. A*, 64(6):063411, Nov 2001.

[62] Marcus Gangl and Helmut Ritsch. Cold atoms in a high-Q ring cavity. *Physical Review A* ***61****, 043405*, (1980).

[63] C. Maes, J.K. Asbóth and H. Ritsch. Self ordering threshold and superradiant backscattering to slow a fast gas beam in a ring cavity with counter propagating pump. *Opt. Express*, 15:6019–6035, 2007.

[64] R. Roy, P. A. Schulz, and A. Walther. Acousto-optic modulator as an electronically selectable unidirectional device in a ring laser. *Opt. Lett.*, 12(9):672–674, 1987.

[65] T. Johnston and W. Proffitt. Design and performance of a broad-band optical diode to enforce one-direction traveling-wave operation of a ring laser. *Quantum Electronics, IEEE Journal of*, 16(4):483 – 488, apr 1980.

[66] G. R. M. Robb, B. W. J. McNeil, R. Bonifacio, and N. Piovella. Dispersive optical bistability in cold atomic vapours. *Optics Communications*, 194(1-3):151 – 165, 2001.

[67] Lucia De Salvo, Roberta Cannerozzi, Rodolfo Bonifacio, Eduardo J. D'Angelo, and Lorenzo M. Narducci. Collective-variables description of the atomic-recoil laser. *Phys. Rev. A*, 52(3):2342–2349, Sep 1995.

[68] M. Abramowitz and I. A. Stegun. *Handbook of Mathematical Functions with Formulas, Graphs, and Mathematical Tables, 9th edition.*

[69] R. Graham, M. Schlautmann, and D. L. Shepelyansky. Dynamical localization in josephson junctions. *Phys. Rev. Lett.*, 67(2):255–258, Jul 1991.

[70] M. Hemmerling and G. R. M. Robb. Slowing atoms using optical cavities pumped by phase-modulated light. *Phys. Rev. A*, 82(5):053420, Nov 2010.

[71] L. P. Faucheux, L. S. Bourdieu, P. D. Kaplan, and A. J. Libchaber. Optical thermal ratchet. *Phys. Rev. Lett.*, 74(9):1504–1507, Feb 1995.

[72] Emil Lundh and Mats Wallin. Ratchet effect for cold atoms in an optical lattice. *Phys. Rev. Lett.*, 94(11):110603, Mar 2005.

[73] Cécile Robilliard, D. Lucas, and G. Grynberg. Modelling a ratchet with cold atoms in an optical lattice. *Applied Physics A: Materials Science and Processing*, 75:213, 2002. 32.80.Pj, 32.60.+i, 87.10.+e, 05.40.+j, 05.60.+w.

[74] E. Anderson, Z. Bai, C. Bischof, S. Blackford, J. Demmel, J. Dongarra, J. Du Croz, A. Greenbaum, S. Hammarling, A. McKenney, and D. Sorensen. *LAPACK Users' Guide.* Society for Industrial and Applied Mathematics, Philadelphia, PA, third edition, 1999.

[75] H. W. P. Chan. *Cavity cooling of cesium atoms*. PhD thesis, Stanford University, 2003.

[76] Ovidiu Toader, Sajeev John, and Kurt Busch. Optical trapping, field enhancement and laser cooling inphotonic crystals. *Opt. Express*, 8(3):217–222, 2001.

[77] Claude N. Cohen-Tannoudji. Nobel lecture: Manipulating atoms with photons. *Rev. Mod. Phys.*, 70(3):707–719, Jul 1998.

[78] H. J. Metcalf and P. van der Straten. Laser cooling and trapping of atoms. *J. Opt. Soc. Am. B*, 20(5):887–908, 2003.

[79] Curtis C. Bradley and Randal G. Hulet. Laser cooling and atom trapping. *Atomic, Molecular, and Optical Physics*, 29B:129–144, 1966.

[80] Harold Metcalf and Peter van der Straten. Cooling and trapping of neutral atoms. *Physics Reports*, 244(4-5):203 – 286, 1994.

[81] Sophie Schlunk. *AC Electric Trapping of Neutral Atoms*. PhD thesis, Stanford University.

[82] N. P. Bigelow and M. Prentiss. Decreased damping of ultracold atoms in optical molasses: predictions and a possible solution. *Opt. Lett.*, 15(24):1479–1481, 1990.

[83] R Miller, T E Northup, K M Birnbaum, A Boca, A D Boozer, and H J Kimble. Trapped atoms in cavity qed: coupling quantized light and matter. *Journal of Physics B: Atomic, Molecular and Optical Physics*, 38(9):S551, 2005.

[84] D. van Thourhout and J. Roels. Optomechanical device actuation through the optical gradient force. *Nature Photonics*, 4:211–217, April 2010.

[85] Craig Savage. Introduction to light forces, atom cooling, and atom trapping. In *Selected papers from the workshop on Lectures in Atom Optics*, pages 745–764, East Melbourne, Victoria, Australia, Australia, 1996. Commonwealth Scientific and Industrial Research Organization.

[86] A. Ashkin. Atomic-beam deflection by resonance-radiation pressure. *Phys. Rev. Lett.*, 25(19):1321–1324, Nov 1970.

[87] D. J. Wineland and Wayne M. Itano. Laser cooling of atoms. *Phys. Rev. A*, 20(4):1521–1540, Oct 1979.

[88] Rudolf Grimm, Matthias Weidemüller, and Yurii B. Ovchinnikov. Optical dipole traps for neutral atoms. *Adv. At. Mol. Opt. Phys.*, 42:95–170, Feb 2000.

[89] Stig Stenholm. The semiclassical theory of laser cooling. *Rev. Mod. Phys.*, 58(3):699–739, Jul 1986.

[90] Vladan Vuletić, James K. Thompson, Adam T. Black, and Jonathan Simon. External-feedback laser cooling of molecular gases. *Phys. Rev. A*, 75(5):051405, May 2007.